

University of Groningen

Exciton Dynamics and Charge Carrier Generation in Organic Semiconductors

Raul, Benedito

DOI:
[10.33612/diss.242400569](https://doi.org/10.33612/diss.242400569)

IMPORTANT NOTE: You are advised to consult the publisher's version (publisher's PDF) if you wish to cite from it. Please check the document version below.

Document Version
Publisher's PDF, also known as Version of record

Publication date:
2022

[Link to publication in University of Groningen/UMCG research database](#)

Citation for published version (APA):
Raul, B. (2022). *Exciton Dynamics and Charge Carrier Generation in Organic Semiconductors*. University of Groningen. <https://doi.org/10.33612/diss.242400569>

Copyright

Other than for strictly personal use, it is not permitted to download or to forward/distribute the text or part of it without the consent of the author(s) and/or copyright holder(s), unless the work is under an open content license (like Creative Commons).

The publication may also be distributed here under the terms of Article 25fa of the Dutch Copyright Act, indicated by the "Taverne" license. More information can be found on the University of Groningen website: <https://www.rug.nl/library/open-access/self-archiving-pure/taverne-amendment>.

Take-down policy

If you believe that this document breaches copyright please contact us providing details, and we will remove access to the work immediately and investigate your claim.

Downloaded from the University of Groningen/UMCG research database (Pure): <http://www.rug.nl/research/portal>. For technical reasons the number of authors shown on this cover page is limited to 10 maximum.

Exciton Dynamics and Charge Carrier Generation in Organic Semiconductors

Dedicado a minha mãe

**Benedito Amado Luís Raúl
2022**

Exciton Dynamics and Charge Carrier Generation in Organic Semiconductors

Benedito Amado Luís Raúl PhD thesis
University of Groningen

Zernike Institute PhD Thesis series 2022-18
ISSN: 1570-1530

The research presented in this thesis was performed in the research group of Optical Condensed Matter Physics, Zernike Institute for Advanced Materials at the University of Groningen. The work was funded by the European Union's Horizon 2020 research and innovation programme under the Marie Skłodowska-Curie grant agreement No. 722651 (SEPOMO).

Cover art: Girolamo Sferrazza Papa
Layout design: Benedito Amado Luís Raúl
Printed by: Ridderprint, www.ridderprint.nl

© Benedito Amado Luís Raúl, Groningen 2022. All rights reserved.



**university of
 groningen**

**faculty of science
 and engineering**

**zernike institute for
 advanced materials**



university of
 groningen

Exciton Dynamics and Charge Carrier Generation in Organic Semiconductors

PhD thesis

to obtain the degree of PhD at the
University of Groningen
on the authority of the
Rector Magnificus Prof. C. Wijmenga
and in accordance with
the decision by the College of Deans.

This thesis will be defended in public on
Tuesday 1 November 2022 at 14.30 hours

by

Benedito Amado Luís Raúl

born on 4 March 1992
in Nampula, Mozambique

Supervisors

Prof. M.S. Pchenitchnikov

Prof. L.J.A. Koster

Co-supervisor

Dr. E. Barrena

Assessment Committee

Prof. R. Hildner

Prof. K. Vandewal

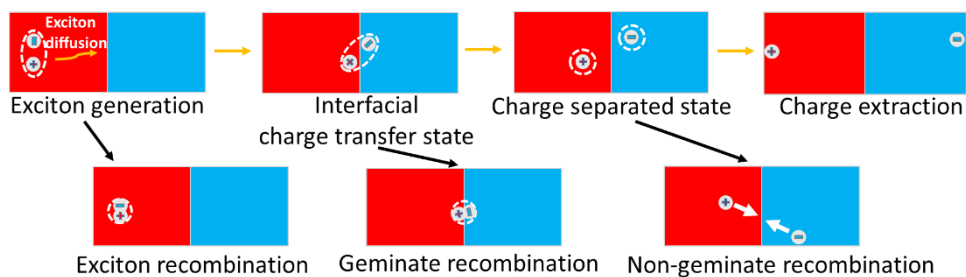
Prof. B. Ehrler

Table of Contents

Chapter 1. General Introduction	1
1.1 Organic Semiconductors	2
1.1.1 Excitons in Organic Semiconductors.....	3
1.2 Organic Solar Cells.....	4
1.3 Photon-to-Charge Conversion in Organic Semiconductors	6
1.3.1 Photon Absorption and Exciton Generation	6
1.3.2 Exciton Diffusion	9
1.3.3 Exciton Dissociation and Charge Pair Separation	12
1.4 Aims and Objectives of Thesis.....	15
1.5 Detection of Photophysical Processes	16
1.5.1 Steady-State Absorption	16
1.5.2 Time-resolved Photoluminescence	16
1.5.3 Pump-Probe Transient Absorption	18
1.6 Main Findings and Overview of the Thesis.....	19
1.7 Personal Contribution.....	20
1.8 References	21
Chapter 2. Excited State Dynamics and Exciton Diffusion in Triphenylamine-based Small Push–Pull Molecule.....	27
2.1 Introduction	28
2.2 Results and Discussion	29
2.2.1 Material Properties	29
2.2.2 Excited State Dynamics in Solution	30
2.2.3 TDDFT Calculations	32
2.2.4 Excited State Lifetime and Energetic Disorder in Film.....	34
2.2.5 Exciton Diffusion Length and Coefficient	36
2.2.6 Device Performance	38
2.3 Conclusions	39
2.4 Methods	40
2.4.1 Sample Preparation.....	40

2.4.2 Time-resolved Photoluminescence, Absorption and Quantum Yield	40
2.5 Supplementary Information.....	42
2.5.1 Photoluminescence Maps and Dynamical Stokes Shift (of solutions and matrix)	42
2.5.2 Molecular Orbital Calculations	43
2.5.3 Photoluminescence Maps of Neat Film.....	43
2.5.4 Average Separation between Quenchers	44
2.5.5 Monte Carlo Simulations.....	44
2.5.6 Effect of Intramolecular Acceptor Unit.....	46
2.6 References	53
Chapter 3. Exciton Dynamics in Solution-Processed Films of Novel Fullerene Derivatives.....	57
3.1 Introduction	58
3.2 Results and Discussion.....	59
3.2.1 Absorption and Photoluminescence	59
3.2.2 Exciton Dissociation.....	61
3.3 Conclusions	67
3.4 Methods	68
3.4.1 Sample Preparation.....	68
3.4.2 Time-resolved Photoluminescence and Absorption	68
3.5 Supplementary Information.....	69
3.5.1 Photoluminescence Spectra and Transients.....	69
3.5.2 Photoluminescence Volume Quenching.....	71
3.5.3 Monte Carlo Simulations.....	75
3.5.4 Estimation of Average Distance between Excitons.....	76
3.6 References	77
Chapter 4. Charge Carrier Generation in Star-Shaped Molecule for Single-Component Organic Solar Cells.....	79
4.1 Introduction	80
4.2 Results and Discussion.....	81

4.2.1 Absorption and Photoluminescence Spectra	81
4.2.2 Excited State Lifetimes.....	84
4.2.3 Charge Carrier Dynamics	87
4.2.4 Photoluminescence Volume Quenching.....	90
4.3 Conclusions	92
4.4 Methods	93
4.4.1 Sample Preparation.....	93
4.4.2 Time-resolved Photoluminescence.....	93
4.4.3 Transient Absorption	94
4.5 References	96
Chapter 5. Tailored Charge Carrier Generation in Star-Shaped Molecules for Enhanced Device Performance.....	99
5.1 Introduction	100
5.2 Results and Discussion.....	102
5.2.1 Absorption and Photoluminescence	102
5.2.2 Charge Carrier Generation.....	106
5.2.3 Exciton Diffusion	108
5.3 Conclusions	110
5.4 Methods	111
5.4.1 Sample Preparation.....	111
5.4.2 Time-resolved Photoluminescence and Absorption	111
5.5 Supplementary Information.....	112
5.5.1 Photoluminescence Mean Energy Shift.....	112
5.5.2 Photoluminescence Volume Quenching.....	113
5.5.3 Monte Carlo Simulations.....	115
5.6 References	117
Summary	121
Samenvatting.....	125
Acknowledgements.....	129
Curriculum Vitae.....	132



Chapter 1. General Introduction

Solution and vacuum processable organic solar cells (OSCs) have recently been in the spotlight as an attractive energy source owing to their continuously rising power conversion efficiencies. In this manner, it is fundamental to critically assess and revise the current understanding of the basic working principles of OSCs, in particular the early times photophysical processes that leads to photocurrent generation. This introductory Chapter provides an overview of the photophysical processes in organic semiconductors relevant to OSCs.

1.1 Organic Semiconductors

Organic materials are composed mainly of carbon atoms (electron configuration of $1S^2 2S^2 2P^2$, according to the Aufbau principle and Hund's rule¹). The atomic orbitals of carbon hybridize to participate in multiple bonds when combined with other atoms to form a molecule. For example, in the formation of methane molecule (CH_4), one of the $2S^2$ electrons in the carbon atom is promoted to the vacant $2P_Z$ orbital, and the $2S^1$ orbital combines with the three $2P$ orbitals ($2P_X, 2P_Y, 2P_Z$) to form SP^3 degenerate hybridized orbitals. Thus, in the new hybridized form, carbon has four unpaired electrons that are used to form the bonding and anti-bonding molecular orbitals (MO) with hydrogen atoms. The bonding/anti-bonding MO formed from hybridized orbitals are called sigma bonding (σ) and anti-bonding (σ^*) MO, respectively.

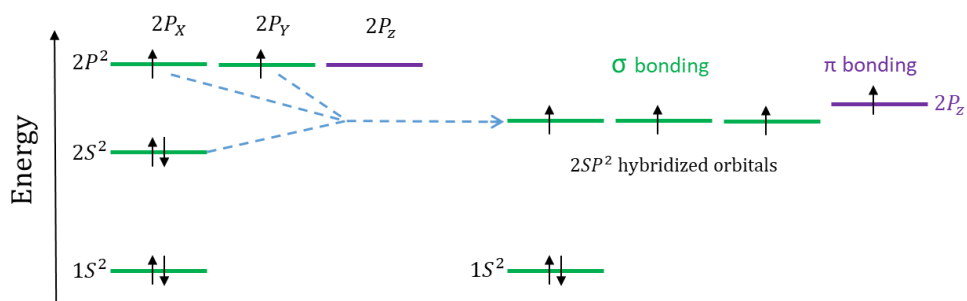


Figure 1.1. Schematic of energy levels for SP^2 hybridized carbon.

A different scenario would be the formation of ethylene (C_2H_4), in this case the $2S^2$ orbital of carbon atom combines with the two $2P$ orbitals ($2P_X, 2P_Y$) to form the SP^2 degenerate hybridized orbitals, leaving the $2P_Z$ orbital unhybridized (Figure 1.1). The three unpaired electrons from the hybridized orbitals are used to form the carbon–hydrogen (σ) and (σ^*) MO, and the carbon–carbon (σ) and (σ^*) MO (Figure 1.2a). The unhybridized $2P_Z$ orbitals form the second carbon–carbon MO, the so-called π bonding and π^* anti-bonding MO (Figure 1.2b). The overlap of the $2P_Z$ electron wave functions leads to delocalization of the charges (π –conjugation), which is the origin of conductivity of organic materials^{2,3}. Photon absorption can promote one of the π electrons to π^* in the so called π – π^* transition (the promotion of σ electrons is also possible but requires higher energy).

In this thesis, we mainly consider two important orbitals: the highest molecular orbital occupied by electrons of a molecule in the ground state (HOMO, highest occupied molecular orbital) and the lowest molecular orbital unoccupied by electrons in the ground state (LUMO, lowest unoccupied molecular orbital).

In ethylene, the HOMO corresponds to the bonding MO (π), and the LUMO to anti-bonding MO (π^*). In the literature, the energies calculated for HOMO and LUMO are typically based on one-electron orbital, neglecting any interaction between electrons, thus deviating from the energy required to experimentally remove (ionization potential) or add (electron affinity) an electron from/to a neutral molecule.

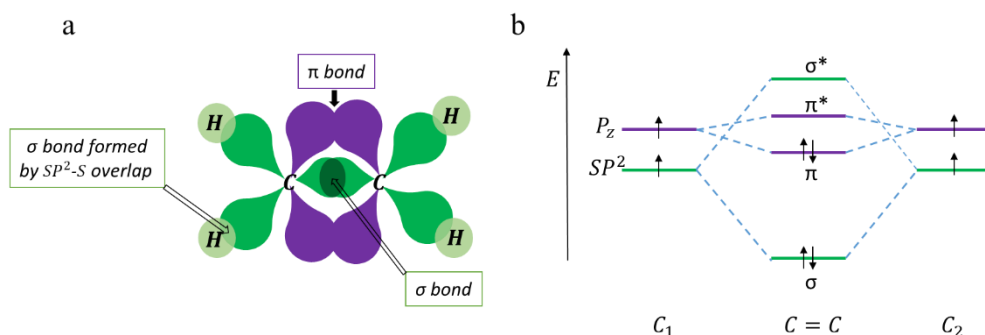


Figure 1.2. (a) Hybridized atomic orbitals and chemical bonding in ethylene C_2H_4 molecule. (b) Energy diagram of bonding and anti-bonding MO in carbon–carbon bonding with SP^2 hybridization.

1.1.1 Excitons in Organic Semiconductors

In inorganic semiconductors (which typically have high values of dielectric constant, ranging from 10–15)⁴, the collective response to an excitation leads to a weakly bound electron–hole pair called Wannier–Mott exciton⁵. The Wannier–Mott excitons have radii that are larger than the lattice spacing, and the exciton binding energy is typically less than ~ 25 meV, enabling excitons to dissociate into free charges at room temperature. Conversely, in organic semiconductors (which have intrinsically low dielectric constant values, typically less than 4)⁴, the collective response to an excitation leads to a strongly bound electron–hole pair called Frenkel exciton⁶.

The Frenkel exciton binding energy is typically significantly greater than the average thermal energy at room temperature of ~ 25 meV⁷, thus, exciton dissociation at room

temperature is less probable. For efficient exciton dissociation into charges, a heterojunction structure composed of electron donating and accepting materials (details in the next section) is typically used to overcome the Coulomb attraction between the electrons and holes. This is the commonly used strategy in the manufacturing of organic solar cells⁸⁻¹².

1.2 Organic Solar Cells

A solar cell is an optoelectronic device that converts light energy into electricity through the photovoltaic effect. The ever-increasing demand for cleaner sources of energy calls for the manufacturing of inexpensive and highly efficient solar cells¹³. Solution and vacuum-processable organic solar cells (OSCs) have recently been in the spotlight as an attractive source of energy owing to their continuously rising power conversion efficiency, low cost, thin device structure, and mechanical flexibility⁸⁻¹⁴.

Various OSCs device architectures have been investigated over the years. In the planar heterojunction structure (Figure 1.3a) introduced by Ching W. Tang in 1986¹⁵, two layers consisting of donor and acceptor materials were used to dissociate excitons. The major limiting factor in this design was the mismatch between light absorption depth of ~100 nm and the typical short exciton diffusion length in organic materials of ~10 nm. In this scenario, assuming complete absorption of incident light and 100% exciton generation, only 10% of the generated excitons reach the donor-acceptor interface for dissociation into charge carriers, fundamentally limiting the device performance.

To circumvent the limitations associated with a planar heterojunction structure, a possible strategy is fine tuning material processing to extend the exciton diffusion length, thus allowing manufacture of devices with thicker layers. Alternatively, a columnar structure^{16,17} with alternating thin columns of donor and acceptor materials can be fabricated (Figure 1.3b). However, a columnar structure requires complex fabrication processes, which is not ideal for commercial-scale application. An intermediate solution was introduced in the early 1990s¹⁸, by intimately mixing the donor and acceptor materials to form the so-called bulk heterojunction (BHJ).

The BHJ structure is produced by spin-coating the donor-acceptor blend or by co-evaporation of small molecules. In the BHJ configuration (Figure 1.3c), a nanoscale phase separation of donor and acceptor materials is formed, ensuring efficient exciton

harvesting over the whole extent of the solar cell without compromising the device thickness. However, due to the complex and often ill-controlled nano-morphology, well-defined pathways for charges toward the electrodes are difficult to produce, which decreases the efficiency of charge collection¹⁹. Furthermore, the nano-morphology is thermodynamically unstable; and the progressive macro-phase separation of donor and acceptor materials is among the most pertinent causes of instability of BHJs^{20,21}. In this manner, the fabrication of OSCs using a single material (with intramolecular donor and acceptor units) in the active layer (Figure 1.3d) mitigates the morphological instability of BHJs, provides additional cost reduction for OSCs, and further simplifies the fabrication process^{22–25}. Nevertheless, the positive effects of BHJ on the device performance outweigh the drawbacks and BHJ concept is currently the most commonly used configuration^{26,27}.

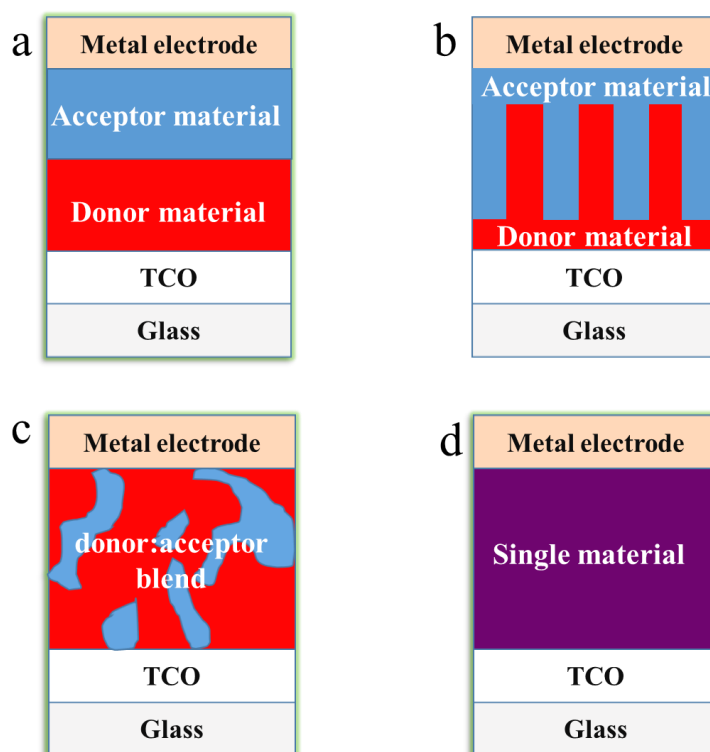


Figure 1.3. Representation of different OSCs architectures. (a) Bi-layer planar heterojunction, (b) columnar structure, (c) bulk heterojunction, and (d) single component

1.3 Photon-to-Charge Conversion in Organic Semiconductors

The photophysical process in organic semiconductors leading to photocurrent generation includes the following steps (Figure 1.4)¹⁹:

- 1- Photon absorption and exciton generation
- 2- Exciton diffusion
- 3- Exciton dissociation into charges
- 4- Charge transport toward electrodes
- 5- Charge extraction at electrodes

All of the steps are subject to losses (Figure 1.4); therefore, it is fundamental to critically assess each step, in order to improve the device performance. In this thesis, we focus on the first three steps, from exciton generation to dissociation into charges. Charge transport and extraction are beyond the scope of this thesis.

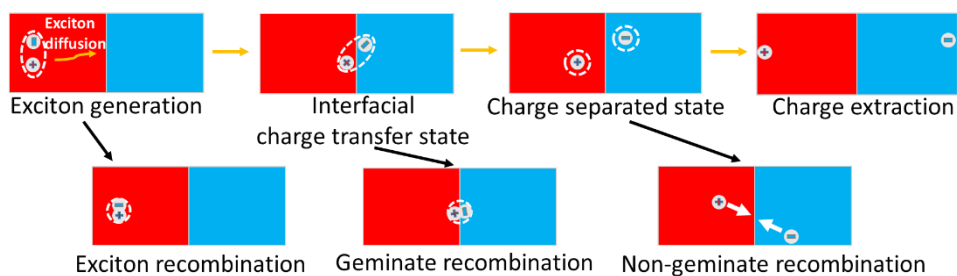


Figure 1.4. Photophysical processes in OSCs leading to photocurrent generation (orange arrows) and recombination losses (black arrows). The donor material is represented in red, and the acceptor material is represented in blue.

1.3.1 Photon Absorption and Exciton Generation

The lowest possible state of a molecule is the ground state. The photon absorption can lead a molecule from the ground state to an excited state. This change in state is possible due to the promotion of one electron from the HOMO to LUMO of a molecule. The promotion of an electron to LUMO + 1 is also possible but requires higher energy. In this thesis, we mainly consider the transitions from HOMO to LUMO. When the spins of electrons in the LUMO and that of remaining electron in the HOMO are antiparallel and add up to a net spin of zero (spin multiplicity of one),

we refer the spins of electrons as singlet state². Conversely, when the spins are parallel (or antiparallel) and the net spin add up to one (spin multiplicity of three), we refer the spins of electrons as triplet state². The representation of ground, singlet, and triplet states for isolated molecules in terms of MO and in state diagram are presented in Figure 1.5.

In Figure 1.5b, photon absorption causes the molecule to change from the ground state (S_0) to the first singlet excited state (S_1). Upon photon absorption, the molecule rapidly relaxes to the lowest vibrational level of S_1 (internal conversion) through heat dissipation to the surrounding environment. From S_1 , emission of photons (fluorescence) can be observed or a subsequent intersystem crossing to the triplet state (T_1) can also yield photon emission (phosphorescence). Both fluorescence and phosphorescence (also referred to as photoluminescence) compete with non-radiative processes such as thermal relaxation, intersystem crossing, conformational changes (see chapter 2 for details), electron or hole transfer in the presence of appropriate quenchers (see chapters 2, 3, 4 and 5 for details), exciton–exciton annihilation, etc.

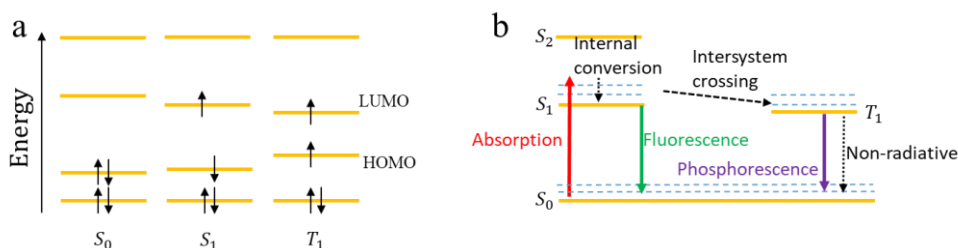


Figure 1.5. (a) Orbital diagram representation of ground (S_0), singlet (S_1) and triplet (T_1) states. Arrows indicate electron spins. (b) State diagram (Jablonski diagram) showing main transitions in organic semiconductors.

The excited state population decays according to the radiative (k_r) and nonradiative (k_{nr}) decay rates as

$$\frac{dn(t)}{dt} = -(k_r + k_{nr})n(t) \quad (1.1)$$

where $n(t)$ is the number of excited molecules at time t upon photoexcitation. From Equation (1.1), it follows that the integral $\int \frac{dn(t)}{n(t)} = -\int (k_r + k_{nr})dt$, yields a mono-exponential function:

$$n(t) = \alpha \exp(-t/\tau_f) \quad (1.2)$$

$$\tau_f = \frac{1}{k_r + k_{nr}} \quad (1.3)$$

where α is the pre-exponential factor, and τ_f is the excited state lifetime (photoluminescence lifetime).

The intrinsic, natural, or radiative lifetime of the fluorophore corresponds to the lifetime in the absence of non-radiative decay processes and is expressed as $\tau_r = \frac{1}{k_r}$.

The fluorescence quantum yield Q_f , defined as the ratio of the number of emitted photons to the number of absorbed photons, can be determined as

$$Q_f = \frac{k_r}{k_r + k_{nr}} = k_r \tau_f \quad (1.4)$$

Using the fluorescence quantum yield (Equation 1.4) and the measured excited state lifetime (Equation 1.3), the radiative lifetime can also be calculated as $\tau_r = \frac{\tau_f}{Q_f}$. The non-radiative decay rate can be calculated as $k_{nr} = \frac{(1-Q_f)}{\tau_f}$.

If two or more subpopulations exist that decay by different processes, Equation (1.2) can be written as

$$n(t) = \sum_i \alpha_i \exp(-t/\tau_i) \quad (1.5)$$

In this case, the excited-state lifetime is defined by the average time the molecule spends in the excited state, and is determined using the statistical method of survival analysis as²⁸

$$\langle \tau_f \rangle = \frac{\int_0^\infty t n(t) dt}{\int_0^\infty n(t) dt} = \frac{\int_0^\infty t \sum_i \alpha_i \exp(-t/\tau_i) dt}{\int_0^\infty \sum_i \alpha_i \exp(-t/\tau_i) dt} = \frac{\sum_i \alpha_i \tau_i^2}{\sum_i \alpha_i \tau_i} \quad (1.6)$$

The state diagrams in Figure 1.5b describing isolated molecules, can also be used to describe excitonic transitions². Thus, excitons with total spin of zero or one are called singlet or triplet excitons, respectively. In the following sections, we focus on singlet exciton dynamics, which is within the scope of this thesis.

1.3.2 Exciton Diffusion

Singlet exciton migration

Excitons migrate between conjugated segments of organic semiconductors via non-radiative energy transfer processes (intermolecular interactions) from an excited molecule to a ground-state nearby molecule. The exciton migration process in organic semiconductors occurs via dipole-dipole interactions or through exchange of electrons (Dexter energy transfer)²⁹⁻³¹.

Singlet exciton diffusion modelling

A π -conjugated system with unperturbed P_Z orbitals overlap would ideally ensure long range exciton migration. However, this is not the case in organic semiconductor films (e.g., amorphous films), where due to defects and random orientation of molecules, the conjugation breaks along a molecule. As a result, the HOMO and LUMO have a distribution of energies³²⁻³⁴(Figure 1.6) described by a normal (Gaussian) distribution function³⁵:

$$g(\varepsilon) = \frac{1}{\sigma\sqrt{2\pi}} e^{-\frac{(\varepsilon-\varepsilon_0)^2}{2\sigma^2}} \quad (1.7)$$

where the standard deviation σ is the energetic disorder, ε is the energy of hopping sites, ε_0 is the mean energy.

In the simplest terms, exciton diffusion in a three-dimensional medium is considered as an ensemble of nearest neighbor hopping events that can be described by Equation (1.8)^{29,36}:

$$\frac{\partial n(r, t)}{\partial t} = G(r, t) + D\nabla^2 n(r, t) - \frac{\partial n(r, t)}{\tau} \quad (1.8)$$

where $n(r, t)$ is the exciton density, $G(r, t)$ is the exciton generation rate, r is the exciton position, D is the diffusion constant and is assumed to be isotropic, ∇^2 is the Laplace operator, τ is the exciton lifetime. In Equation (1.8), the first term $G(r, t)$ represents exciton generation upon light absorption, the second term represents exciton migration by diffusion, and the third term represents exciton recombination.

The average displacement of a particle from its initial position, i.e., the exciton diffusion length is expressed as:

$$L_D = \sqrt{2ZD\tau} \quad (1.9)$$

where Z is the spatial dimensionality which is equal to 1, 2 or 3 in case of one-, two- or three-dimensional diffusion process, respectively.

Exciton diffusion in disordered medium is primarily characterized by downhill migration toward lower energetic levels, resulting in a dynamical red shift of photoluminescence³⁷. The total photoluminescence mean energy shift stabilizes at $\Delta E_{PL} = E_{PL}(t = 0) - E_{PL}(t = \infty) \cong \frac{\sigma^2}{kT}$, below the center of density of states (Figure 1.6) (σ is the energetic disorder, $kT \sim 25$ meV is the room temperature thermal energy)³⁸. Here, the quasi-equilibrium is reached and the thermally activated hopping mainly contributes to the diffusion process³⁷. Thus, accounting for downhill migration, a generalized differential form of the Einstein-Smoluchowski relation is used to determine the time dependent exciton diffusion coefficient as

$$D(t) = \frac{\partial \langle l^2(t) \rangle}{6\partial t} \quad (1.10)$$

where $\langle l^2(t) \rangle$ is the average square of excitons displacement (over the whole exciton ensemble), and t is the diffusion time. In this manner, the exciton diffusion coefficient is primarily time dependent during downhill migration and becomes constant when the quasi-equilibrium is reached.

In Chapters 2, 3 and 5, we use time-resolved photoluminescence volume quenching technique combined with Monte Carlo simulations³⁹ to determine the exciton diffusion length. The energetic disorder is readily obtained experimentally from the photoluminescence mean energy shift. The exciton diffusion is simulated within a Gaussian density of states (Figure 1.6), where the exciton hopping is a thermally activated process and the hopping probability (p_{if}) at room temperature ($kT \sim 25$ meV) is determined from the Boltzmann factor depending on the initial (E_i) and final (E_f) energies³⁹:

$$p_{if} = \begin{cases} 1, & E_i \geq E_f \\ e^{-\frac{E_f - E_i}{kT}}, & E_i < E_f \end{cases} \quad (1.11)$$

From here, by using the exciton hopping time as a fitting parameter, the time-dependent exciton diffusion coefficient and the exciton diffusion length are determined. A detailed description of the Monte Carlo simulations is provided in Chapter 2.

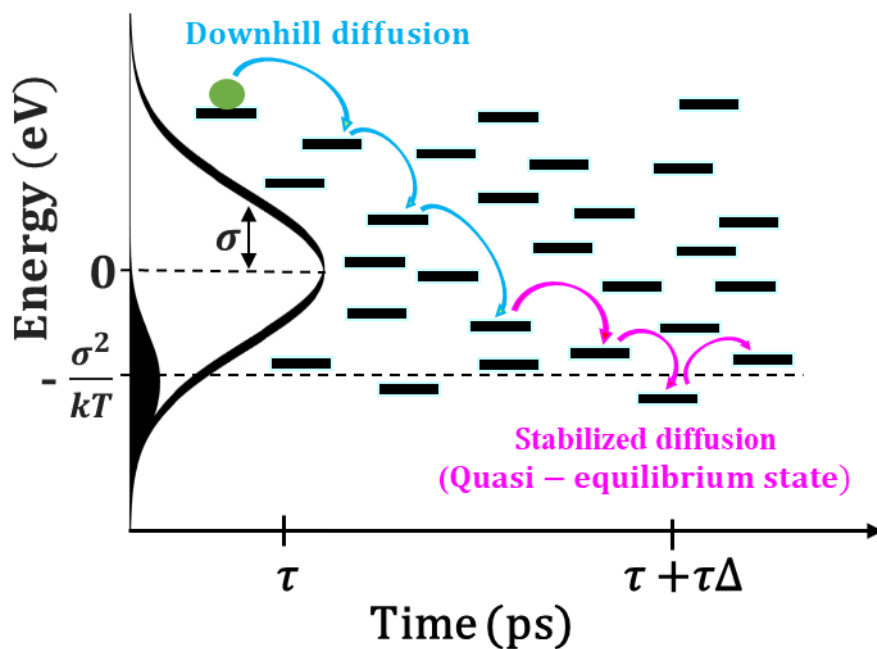


Figure 1.6. Illustration of exciton diffusion in disordered medium. At early (τ) exciton migrate downhill and reach the quasi-equilibrium state at a later time ($\tau + \Delta\tau$). The energy at quasi-equilibrium is equal to $-\frac{\sigma^2}{kT}$, from which the energetic disorder σ is readily obtained.

1.3.3 Exciton Dissociation and Charge Pair Separation

Small-molecule homojunctions for exciton dissociation

To efficiently dissociate the exciton into charge carriers, electron-donating and electron-accepting materials with suitable energy levels are typically used. This creates an energy level offset which acts as the driving force to overcome the coulomb attraction between the electron–hole pairs and finally dissociate the exciton into charge carriers. Figure 1.7 shows a typical example of favorable energetic alignment for exciton dissociation.

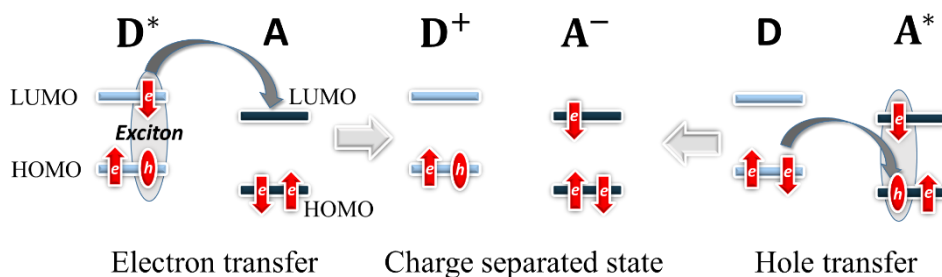


Figure 1.7. Electron or hole transfer process involving an excited donor (D^*) or acceptor (A^*) with suitable energy levels. Plus, and minus signs indicate positive and negative charges, respectively.

The LUMO energy level of the acceptor is lower than the LUMO of the donor molecule, which allows electron transfer from the donor to the acceptor. Similarly, to allow hole transfer from the acceptor to the donor, the HOMO energy level of the acceptor should be lower than the HOMO of the donor. The hole transfer process can be viewed as an electron transfer from the HOMO of the donor to the HOMO of the acceptor upon photoexcitation of the acceptor. In this manner, regardless of the donor or acceptor photoexcitation, the system always ends up at the same charge-separated state with the donor molecule positively charged and the acceptor molecule negatively charged.

The acceptor materials for OSCs are typically categorized into fullerenes and non-fullerenes acceptors^{40–42}. The photophysics of fullerene derivatives are discussed in Chapter 3.

There are several classes of donor materials^{23,43–51}, and among them, donor materials with intramolecular donor and acceptor units are the most promising for efficient exciton dissociation^{51,52}. The reason for this is their structure that combines the intramolecular donor-acceptor units, which upon photoexcitation promotes the delocalization of electron density to be mainly along the intramolecular acceptor unit of the molecule⁵³. As a result, the exciton dissociation process is initiated, or in some cases, a complete exciton dissociation into charges is possible without the need of an external acceptor⁵³. In this regard, donor materials with intramolecular donor-acceptor units represent a very attractive class of materials not only for BHJ architecture (Chapters 2 and 3), but also for single-component OSCs (Chapter 4 and 5)^{22–24,51,52}. Figure 1.8 depicts the structure of two donor materials with intramolecular donor-acceptor units, namely, a linear push-pull molecule (Figure 1.8a) and a star-shaped molecule (Figure 1.8b).

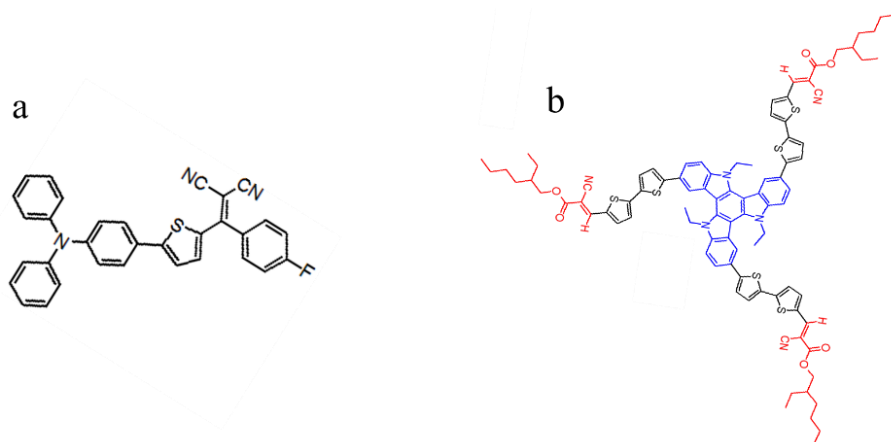


Figure 1.8. Two donors used in this thesis. **(a)** Linear push-pull molecule TPA-TDCV-Ph-F (discussed in Chapter 2). **(b)** Star-shaped molecule BTI(2T – CNA – EHex)₃ (discussed in Chapter 4).

Charge transfer and charge separated state

Upon its generation, exciton migrates to the donor–acceptor interface in order to dissociate into charge carriers. Following electron transfer at the donor–acceptor interface, the exciton evolves into a charge pair with the hole partially residing in the donor molecule and the electron in the acceptor. This intermediate state involving a charge pair at the donor–acceptor interface is known as interfacial charge transfer (CT) state (Figure 1.4). The existence of interfacial CT state has been evidenced from both absorption^{54–56} and luminescence^{57–59} measurements. In some donor–acceptor materials, the charge pair at interfacial CT state has been demonstrated to be Coulombically bound^{60–62}, hence, it is highly susceptible to recombine in the process known as geminate recombination^{63–68} (Figure 1.4).

As the interfacial CT state binding energy is significantly larger than the thermal energy at room temperature (~ 25 meV), it is reasonable to ask about the driving force for the charge pair (at interfacial CT state) to fully dissociate into charges that might contribute to the photocurrent. This is a fundamental question in organic photovoltaics field that is still open for debate^{7,69,70}. There are different mechanisms proposed to answer to this question such as, dissociation via the “hot” interfacial CT state (when the excess energy from the charge pair generation is used to dissociate the charge pair (hot charge pair) before it fully relaxes^{71–74}), dissociation via the relaxed “cold” interfacial CT state^{75,76}, and dissociation induced by charge delocalization^{77,78}. For dissociation via relaxed “cold” interfacial CT state, the driving forces are typically proposed as the electric field and the disorder.

The charge pairs at the interfacial CT state are typically referred to as interfacial CT excitons. In materials with intramolecular donor-acceptor units, both intramolecular CT state and intermolecular CT states are typically formed. Intramolecular CT state can be observed in isolated molecules (e.g., in solutions), while intermolecular CT state is typically observed in neat films. The role of intermolecular CT excitons for charge carrier generation is investigated in Chapter 4 and 5, and the findings are further discussed in terms of applications for single-component OSCs.

When the distance between the electron and hole becomes significant, such that the electron-hole pair binding energy is similar to or smaller than the thermal energy at room temperature (≤ 25 meV), the electron–hole pairs are no longer considered Coulombically bound, and are considered to be at the charge separated (CS) state (Figure 1.4). The charge pairs that fully dissociate reaching the CS state are referred to as free charge carriers. Evidently, to achieve highly efficient OSCs the free-charge

carriers generation must be dominant and the interfacial CT excitons recombination (geminate recombination) should be suppressed.

Following charge-pair separation, the free-charge carriers are transported to the respective electrodes. During the transport, the free-charge carriers may recombine in process called non-geminate recombination^{63–67,79,80} (Figure 1.4). In BHJ OSCs, if the grain sizes of donor and acceptor materials are small, the probability of non-geminate recombination increases. Conversely, if the grain sizes are large (on the order of exciton diffusion length), the excitons might recombine before reaching the donor-acceptor interface. Thus, knowledge of exciton diffusion length is fundamental for morphological optimization of the active layer. The interplay between morphology and exciton diffusion in BHJ is investigated in detail in Chapter 3.

1.4 Aims and Objectives of Thesis

This thesis aims to shed light on exciton dynamics and charge carrier generation in organic photovoltaics. A variety of materials systems (including push-pull small molecules, star-shaped molecules, and fullerenes) were chosen to obtain insights on the limiting factors of exciton diffusion and charge carrier generation in BHJ and single-component OSCs. In accordance with the aims of the thesis, the chapters have the following objectives:

1. Chapter 2: provide detailed understanding of the underlying mechanism governing excited-state dynamics in triphenylamine-based push-pull molecules.
2. Chapter 3: examine the roles of the length and polarity of fullerene derivatives side chains in crystallization and their impact on charge carrier generation.
3. Chapter 4: elucidate the role of intermolecular interactions in the excited-state lifetime and charge-carrier generation in star-shaped molecules.
4. Chapter 5: demonstrate an approach for tuning charge-carrier generation in neat films of star-shaped molecules.

1.5 Detection of Photophysical Processes

There are several methods to probe the photophysical process from photon-to-charge conversion in organic semiconductors. This section provides a brief overview of the experimental methods that were selected according to the aims and objectives of the thesis; more detailed descriptions can be found in Materials and Methods sections of the chapters.

1.5.1 Steady-State Absorption

A simple way to study the transition of molecules from the ground to the excited state is to use steady-state absorption spectrometer. As the absorption per se is not directly measurable, it can be quantified by measuring the transmittance of the sample. The transmittance $T(\lambda)$ of the sample (i.e., the percentage of light that passes through the sample) at several wavelengths is expressed as the ratio of output $P(\lambda)_{\text{out}}$ to the incident powers $P(\lambda)_{\text{in}}$,

$$T(\lambda) = \frac{P(\lambda)_{\text{out}}}{P(\lambda)_{\text{in}}} \quad (1.12)$$

The absorption $A(\lambda)$ of the sample (without considering the reflectance) is readily obtained as $A(\lambda) = 1 - T(\lambda)$. For convenience, the optical density (also called absorbance) calculated as

$$OD(\lambda) = \log_{10} \frac{1}{T(\lambda)} \quad (1.13)$$

is generally used to plot the absorption spectra.

1.5.2 Time-resolved Photoluminescence

In organic semiconductors, the radiative recombination of photo-generated singlet excitons typically occurs within nanosecond time-scale. Thus, the investigation of singlet exciton dynamics requires techniques with picosecond temporal resolution. In this thesis, such resolution is achieved using ultrafast time-resolved photoluminescence setup with a streak camera (Figure 1.9a).

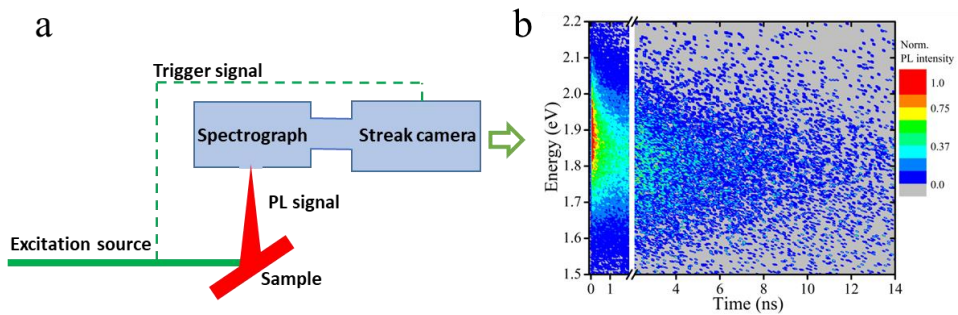


Figure 1.9. (a) Schematic of time-resolved photoluminescence setup with streak camera. (b) Photoluminescence map of TPA-T-DCV-Ph-F neat film. The break separates experimental data obtained with time ranges of 2 ns and 20 ns.

In such setups, the excitation source is typically an ultrafast laser system with femtosecond pulse duration, allowing the measurements of photoluminescence decays with picosecond time resolution. The emission is detected using a spectrograph combined with a streak camera. The spectrograph provides the spectral dispersion of the signal in its constituent wavelengths, and the signal is directed into the streak camera to be temporally resolved.

The incident light in the streak camera is firstly converted into electrons through the photoelectric effect. Then, the electrons are directed to a phosphor screen where the image is formed. During the electron movement to the phosphor screen, an increasing vertical electric field (generated by applying a sweep voltage to a pair of sweep electrodes) is applied to deflect the electrons such that the first photons arriving into the camera experience a small deflection, and photons arriving later experience a larger deflection. In this manner, a two-dimensional image is formed on the phosphor screen with the wavelength and time axis.

The time resolution of a selected time range measurement is set by the slope of the sweep voltage, as it controls the electron spacing on the phosphor screen. Different time ranges can be measured with an approximate time resolution of 10 ps. A charge-coupled device is used to detect the signal intensity at each point on the phosphor screen. The resulting image is called the photoluminescence map (Figure 1.9b), with the vertical axis corresponding to the wavelength (or energy), the horizontal axis corresponding to time, and the color schemes corresponding to the intensity. From the photoluminescence map in Figure 1.9b, the photoluminescence spectrum at specific times or the photoluminescence decay at specific wavelengths (or energies) can be extracted by vertically or horizontally integrating the signal.

1.5.3 Pump-Probe Transient Absorption

Time-resolved photoluminescence is a powerful method for examining emissive species. However, the investigation of non-emissive species requires a different spectroscopy technique. Pump-probe transient absorption is an established method commonly used to investigate the excited-state dynamics of non-emissive species with femtosecond time resolution^{81–90}. In the pump-probe technique, a laser pulse excites the sample (pump pulse), and a subsequent time-delayed pulse (probe pulse) probes the changes induced by the pump pulse (Figure 1.10).

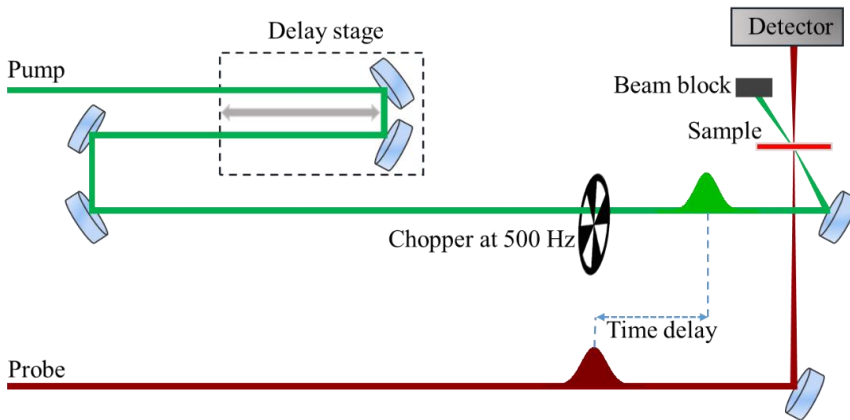


Figure 1.10. Schematic of transient absorption pump-probe setup.

In the actual experiment, the induced change in transmittance $-\Delta T$ is monitored with a lock-in amplifier working at the modulation frequency of the pump (pump on or off). The change in transmittance $-\Delta T$ is normalized to the unperturbed transmittance of the sample (T) to account for intensity variations. The pump-probe transient absorption results presented in this thesis were measured according to:

$$-\frac{\Delta T}{T} = -\frac{\frac{P_{out}^{ON} - P_{out}^{OFF}}{P_{in}}}{\frac{P_{out}^{OFF}}{P_{in}}} = -\frac{P_{out}^{ON} - P_{out}^{OFF}}{P_{out}^{OFF}} \quad (1.14)$$

where P_{out}^{ON} is the output power of the probe beam with the pump beam on (unblocked by the chopper), P_{out}^{OFF} is the output power of the probe beam with the pump beam off (blocked by the chopper), and P_{in} is the incident probe power.

1.6 Main Findings and Overview of the Thesis

The main findings of this thesis are as follow:

1. The short excited-state lifetime in solutions of triphenylamine-based push-pull molecules does not necessarily hinder long exciton diffusion length in films, thereby granting the use of similar push-pull molecules in vacuum- and solution-processable devices.
2. Small changes in the length or polarity of fullerene derivatives side chains have a great effect on charge generation due to the crystallinity of the films.
3. Variations in the intermolecular separation of star-shaped molecules indicate that the bi-exponential photoluminescence decay in neat film is caused by formation of intermolecular charge transfer excitons that undergo charge carrier generation.
4. Elongation of the oligothiophene π -bridge in star-shaped molecules leads to decrease in excited state lifetime and exciton diffusion length due to efficient exciton-to-charge carrier conversion.

A brief summary of each chapter is presented as follows:

In Chapter 2, ultrafast photo-induced processes in solutions and the correlation to the solid-state of triphenylamine-based push-pull materials are investigated. It is demonstrated that conformational changes in solutions can lead to a conical intersection, and suppression of the conformational changes in the solid-state leads to reduced non-radiative relaxation. Exciton diffusion length in solution-processed films is found to be ~ 16 nm, thereby granting the use of the triphenylamine-based push-pull molecules in solid-state devices.

In Chapter 3, the effects of the length and polarity of fullerene derivatives side chains are studied with particular focus on the role of fullerenes as light absorbers. It is found that crystallization plays a crucial role in exciton dissociation in blend films containing fullerenes and exciton quenchers. Exciton dissociation into charge carriers is observed in some blend films, whereas in other blend films excitons do not dissociate. The latter is attributed to the crystallization of fullerenes that drives their self-assembly rather than allowing for fine-intermixing between the quenchers and fullerene derivatives in the blends. These results reiterate that crystallization dynamics should meticulously considered during the manufacturing of organic semiconductors devices.

Chapter 4 addresses the role of intermolecular interactions in the excited-state lifetime and charge carrier generation in neat films of star-shaped molecules. By varying intermolecular separation, it is demonstrated that the bi-exponential photoluminescence decay in the neat films is due to formation of intermolecular charge-transfer excitons that undergo charge-carrier generation. These findings highlight the broad potential of star-shaped molecules in the development of single material devices.

In Chapter 5, the effect of variation of intramolecular donor-acceptor spacing in star-shaped molecules is investigated. It is demonstrated that the increase in intramolecular donor-acceptor spacing leads to decrease in excited state lifetime and exciton diffusion length due to efficient charge carrier generation in the neat films. The approach for tuning charge carrier generation presented in this chapter is beneficial for future development of novel materials for single-component OSCs.

1.7 Personal Contribution

This thesis greatly benefited from close collaboration between research groups from different institutions. The author was directly involved in task formulation, designing and performing experiments, discussing results, implementing Monte-Carlo modeling, and writing the scientific papers. The detailed contributions of the co-authors are specified at the end of each Chapter.

1.8 References

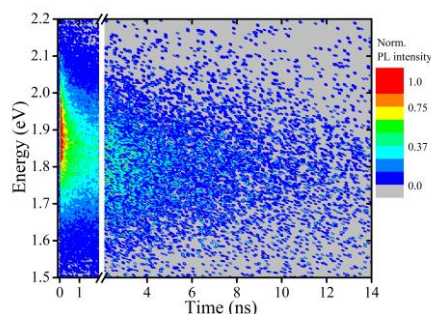
1. Kutzelnigg, W. & Morgan, J. D. Hund's rules. *Zeitschrift fur Phys. D Atoms, Mol. Clust.* **36**, 197–214 (1996).
2. Köhler, A. & Bässler, H. Triplet states in organic semiconductors. *Mater. Sci. Eng. R Reports* **66**, 71–109 (2009).
3. Audenaert, M., Gusman, G. & Deltour, R. Electrical conductivity of I2-doped polyacetylene. *Phys. Rev. B* **24**, 7380–7382 (1981).
4. Brebels, J., Manca, J. V., Lutsen, L., Vanderzande, D. & Maes, W. High dielectric constant conjugated materials for organic photovoltaics. *J. Mater. Chem. A* **5**, 24037–24050 (2017).
5. La Rocca, G. . Wannier–Mott Excitons in Semiconductors. in 97–128 (2003). doi:10.1016/S1079-4050(03)31002-6
6. Frenkel, J. On the transformation of light into heat in solids. i. *Phys. Rev.* **37**, 17–44 (1931).
7. Few, S., Frost, J. M. & Nelson, J. Models of charge pair generation in organic solar cells. *Phys. Chem. Chem. Phys.* **17**, 2311–2325 (2015).
8. Hong, L. *et al.* 18.5% Efficiency Organic Solar Cells with a Hybrid Planar/Bulk Heterojunction. *Adv. Mater.* **33**, (2021).
9. Lin, Y. *et al.* 17.1% Efficient Single-Junction Organic Solar Cells Enabled by n-Type Doping of the Bulk-Heterojunction. *Adv. Sci.* **7**, 1–9 (2020).
10. Burlingame, Q. *et al.* Intrinsically stable organic solar cells under high-intensity illumination. *Nature* **573**, 394–397 (2019).
11. Jiang, Z. *et al.* Highly efficient organic photovoltaics with enhanced stability through the formation of doping-induced stable interfaces. *Proc. Natl. Acad. Sci. U. S. A.* **117**, 6391–6397 (2020).
12. Li, Y. *et al.* Non-fullerene acceptor organic photovoltaics with intrinsic operational lifetimes over 30 years. *Nat. Commun.* **12**, 1–9 (2021).
13. Scharber, M. C. & Sariciftci, N. S. Efficiency of bulk-heterojunction organic solar cells. *Prog. Polym. Sci.* **38**, 1929–1940 (2013).
14. Fukuda, K., Yu, K. & Someya, T. The Future of Flexible Organic Solar Cells. *Adv. Energy Mater.* **10**, 1–10 (2020).
15. Tang, C. W. Two-layer organic photovoltaic cell. *Appl. Phys. Lett.* **48**, 183–185 (1986).
16. Matsuo, Y. *et al.* Columnar structure in bulk heterojunction in solution-processable three-layered p-i-n organic photovoltaic devices using tetrabenzoporphyrin precursor and silylmethyl[60]fullerene. *J. Am. Chem. Soc.* **131**, 16048–16050 (2009).
17. Seo, J. W. *et al.* Columnar-Structured Low-Concentration Donor Molecules in Bulk Heterojunction Organic Solar Cells. *ACS Omega* **3**, 929–936 (2017).
18. Yu, G., Gao, J., Hummelen, J. C., Wudl, F. & Heeger, A. J. Polymer photovoltaic cells: Enhanced efficiencies via a network of internal donor-acceptor heterojunctions. *Science (80-.)*. **270**, 1789 (1995).
19. Deibel, C. & Dyakonov, V. Polymer-fullerene bulk heterojunction solar cells. *Reports Prog. Phys.* **73**, (2010).
20. Cheng, P. & Zhan, X. Stability of organic solar cells: Challenges and strategies. *Chem. Soc. Rev.* **45**, 2544–2582 (2016).
21. Li, N. *et al.* Abnormal strong burn-in degradation of highly efficient polymer solar cells caused by spinodal donor-acceptor demixing. *Nat. Commun.* **8**, 1–9 (2017).

22. Jiang, X. *et al.* Miscibility-Controlled Phase Separation in Double-Cable Conjugated Polymers for Single-Component Organic Solar Cells with Efficiencies over 8 %. *Angew. Chemie - Int. Ed.* **59**, 21683–21692 (2020).
23. Li, S. *et al.* Narrow-Bandgap Single-Component Polymer Solar Cells with Approaching 9% Efficiency. *Adv. Mater.* **33**, (2021).
24. Wu, Y. *et al.* A conjugated donor-acceptor block copolymer enables over 11% efficiency for single-component polymer solar cells. *Joule* **5**, 1800–1815 (2021).
25. Roncali, J. & Grosu, I. The Dawn of Single Material Organic Solar Cells. *Adv. Sci.* **6**, (2019).
26. Dulal, R., Scougale, W. R., Chen, W., Balasubramanian, G. & Chien, T. Y. Direct Observations of Uniform Bulk Heterojunctions and the Energy Level Alignments in Nonfullerene Organic Photovoltaic Active Layers. *ACS Appl. Mater. Interfaces* **13**, 56430–56437 (2021).
27. Liang, Q., Xie, Y. & Wu, H. Elucidating the role of the heterojunction interface in the exciton harvest and charge collection of organic solar cells through a planar heterojunction structure. *J. Mater. Chem. C* **10**, 598–606 (2022).
28. Zatoryb, G. & Klak, M. M. On the choice of proper average lifetime formula for an ensemble of emitters showing non-single exponential photoluminescence decay. *J. Phys. Condens. Matter* **32**, (2020).
29. Mikhnenko, O. V., Blom, P. W. M. & Nguyen, T. Q. Exciton diffusion in organic semiconductors. *Energy Environ. Sci.* **8**, 1867–1888 (2015).
30. Dexter, D. L. A theory of sensitized luminescence in solids. *J. Chem. Phys.* **21**, 836–850 (1953).
31. Menke, S. M. & Holmes, R. J. Exciton diffusion in organic photovoltaic cells. *Energy Environ. Sci.* **7**, 499–512 (2014).
32. Suzuki, F., Kubo, S., Fukushima, T. & Kaji, H. Effects of Structural and Energetic Disorders on Charge Transports in Crystal and Amorphous Organic Layers. *Sci. Rep.* **8**, 1–9 (2018).
33. Zhou, K. *et al.* Interfacial energetic disorder induced by the molecular packing structure at conjugated polymer-based donor/acceptor heterojunctions. *J. Mater. Chem. C* **9**, 13761–13769 (2021).
34. Hood, S., Zarrabi, N., Meredith, P., Kassal, I. & Armin, A. Measuring Energetic Disorder in Organic Semiconductors Using the Photogenerated Charge-Separation Efficiency. *J. Phys. Chem. Lett.* **10**, 3863–3870 (2019).
35. Fisher, H. *The Prehistory: De Moivre's Theorem. A History of the Central Limit Theorem* (2010).
36. Powell, R. C. & Soos, Z. G. Singlet exciton energy transfer in organic solids. *J. Lumin.* **11**, 1–45 (1975).
37. Bäessler, H. Charge Transport in Disordered Organic Photoconductors a Monte Carlo Simulation Study. *Phys. Status Solidi* **175**, 15–56 (1993).
38. Movaghar, B., Gr̄newald, M., Ries, B., Bassler, H. & W̄rtz, D. Diffusion and relaxation of energy in disordered organic and inorganic materials. *Phys. Rev. B* **33**, 5545–5554 (1986).
39. Scheidler, M., Lemmer, U., Marburg, D.- & Thomas, P. Monte Carlo study of picosecond exciton relaxation and dissociation in poly ,, phenylenevinylene *Phys. Rev. B* **54**, 5536–5544 (1996).

40. Speller, E. M. *et al.* From fullerene acceptors to non-fullerene acceptors: Prospects and challenges in the stability of organic solar cells. *J. Mater. Chem. A* **7**, 23361–23377 (2019).
41. Wu, Z. *et al.* Fullerene–non-fullerene hybrid acceptors for enhanced light absorption and electrical properties in organic solar cells. *Mater. Today Energy* **20**, (2021).
42. Armin, A. *et al.* A History and Perspective of Non-Fullerene Electron Acceptors for Organic Solar Cells. *Adv. Energy Mater.* **11**, 1–42 (2021).
43. Roncali, J., Leriche, P. & Blanchard, P. Molecular materials for organic photovoltaics: Small is beautiful. *Adv. Mater.* **26**, 3821–3838 (2014).
44. Nicolas, Y. *et al.* Planarized Star-Shaped Oligothiophenes with Enhanced π -Electron Delocalization. *Org. Lett.* **6**, 273–276 (2004).
45. Mishra, A. & Bäuerle, P. Small molecule organic semiconductors on the move: Promises for future solar energy technology. *Angew. Chemie - Int. Ed.* **51**, 2020–2067 (2012).
46. Leliège, A., Blanchard, P., Rousseau, T. & Roncali, J. Triphenylamine/tetracyanobutadiene-based D-A-D π -conjugated systems as molecular donors for organic solar cells. *Org. Lett.* **13**, 3098–3101 (2011).
47. Zhang, J., Xu, W., Sheng, P., Zhao, G. & Zhu, D. Organic Donor-Acceptor Complexes as Novel Organic Semiconductors. *Acc. Chem. Res.* **50**, 1654–1662 (2017).
48. Raul, B. A. L. *et al.* Excited state dynamics and exciton diffusion in triphenylamine/dicyanovinyl push–pull small molecule for organic optoelectronics. *Sci. Rep.* **10**, 1–10 (2020).
49. Simón Marqués, P. *et al.* Triphenylamine/Tetracyanobutadiene-Based π -Conjugated Push–Pull Molecules End-Capped with Arene Platforms: Synthesis, Photophysics, and Photovoltaic Response. *Chem. - A Eur. J.* **26**, 16422–16433 (2020).
50. Lin, Y., Li, Y. & Zhan, X. Small molecule semiconductors for high-efficiency organic photovoltaics. *Chem. Soc. Rev.* **41**, 4245–4272 (2012).
51. Luponosov, Y. N. *et al.* Effect of oligothiophene π -bridge length in D- π -A star-shaped small molecules on properties and photovoltaic performance in single-component and bulk heterojunction organic solar cells and photodetectors. *Mater. Today Energy* **22**, 100863 (2021).
52. Roncali, J. Single-Material Organic Solar Cells Based on Small Molecule Homojunctions: An Outdated Concept or a New Challenge for the Chemistry and Physics of Organic Photovoltaics? *Adv. Energy Mater.* **11**, 1–9 (2021).
53. Kozlov, O. V. *et al.* Ultrafast Exciton-to-Polaron Conversion in Densely Packed Small Organic Semiconducting Molecules. *Adv. Opt. Mater.* **5**, 1–7 (2017).
54. Goris, L. *et al.* Absorption phenomena in organic thin films for solar cell applications investigated by photothermal deflection spectroscopy. *J. Mater. Sci.* **40**, 1413–1418 (2005).
55. Benson-Smith, J. J. *et al.* Formation of a ground-state charge-transfer complex in polyfluorene/[6,6]-phenyl-C61 butyric acid methyl ester (PCBM) blend films and its role in the function of polymer/PCBM solar cells. *Adv. Funct. Mater.* **17**, 451–457 (2007).
56. Goris, L. *et al.* Observation of the subgap optical absorption in polymer-fullerene blend solar cells. *Appl. Phys. Lett.* **88**, 1–3 (2006).
57. Hasharoni, K. *et al.* Near IR photoluminescence in mixed films of conjugated polymers and fullerenes. *J. Chem. Phys.* **107**, 2308–2312 (1997).

58. Veldman, D. *et al.* Compositional and electric field dependence of the dissociation of charge transfer excitons in alternating polyfluorene copolymer/fullerene blends. *J. Am. Chem. Soc.* **130**, 7721–7735 (2008).
59. Olle, I., Fengling, Z. & Andersson, M. R. Alternating polyfluorenes collect solar light in polymer photovoltaics. *Acc. Chem. Res.* **42**, 1731–1739 (2009).
60. Zhu, X. Y., Yang, Q. & Muntwiler, M. Charge-transfer excitons at organic semiconductor surfaces and interfaces. *Acc. Chem. Res.* **42**, 1779–1787 (2009).
61. Drori, T. *et al.* Below-gap excitation of π -conjugated polymer-fullerene blends: Implications for bulk organic heterojunction solar cells. *Phys. Rev. Lett.* **101**, 1–4 (2008).
62. Hallermann, M., Haneder, S. & Da Como, E. Charge-transfer states in conjugated polymer/fullerene blends: Below-gap weakly bound excitons for polymer photovoltaics. *Appl. Phys. Lett.* **93**, (2008).
63. Proctor, C. M., Kuik, M. & Nguyen, T.-Q. Charge carrier recombination in organic solar cells. *Prog. Polym. Sci.* **38**, 1941–1960 (2013).
64. Kyaw, A. K. K. *et al.* Intensity Dependence of Current–Voltage Characteristics and Recombination in High-Efficiency Solution-Processed Small-Molecule Solar Cells. *ACS Nano* **7**, 4569–4577 (2013).
65. Rao, A. *et al.* The role of spin in the kinetic control of recombination in organic photovoltaics. *Nature* **500**, 435–439 (2013).
66. Foertig, A. *et al.* Nongeminate and Geminate Recombination in PTB7:PCBM Solar Cells. *Adv. Funct. Mater.* **24**, 1306–1311 (2014).
67. Privitera, A. *et al.* Geminate and Nongeminate Pathways for Triplet Exciton Formation in Organic Solar Cells. *Adv. Energy Mater.* **12**, 2103944 (2022).
68. Sandoval-Torrientes, R. *et al.* Minimizing geminate recombination losses in small-molecule-based organic solar cells. *J. Mater. Chem. C* **7**, 6641–6648 (2019).
69. Bässler, H. & Kohler, A. ‘hot or cold’: How do charge transfer states at the donor-acceptor interface of an organic solar cell dissociate? *Phys. Chem. Chem. Phys.* **17**, 28451–28462 (2015).
70. Gao, F. & Inganäs, O. Charge generation in polymer-fullerene bulk-heterojunction solar cells. *Phys. Chem. Chem. Phys.* **16**, 20291–20304 (2014).
71. Ohkita, H. *et al.* Charge carrier formation in polythiophene/fullerene blend films studied by transient absorption spectroscopy. *J. Am. Chem. Soc.* **130**, 3030–3042 (2008).
72. Virgili, T., Marinotto, D., Manzoni, C., Cerullo, G. & Lanzani, G. Ultrafast intrachain photoexcitation of polymeric semiconductors. *Phys. Rev. Lett.* **94**, 1–4 (2005).
73. Schulze, M., Hänsel, M. & Tegeder, P. Hot excitons increase the donor/acceptor charge transfer yield. *J. Phys. Chem. C* **118**, 28527–28534 (2014).
74. Shimazaki, T. & Nakajima, T. Theoretical study of exciton dissociation through hot states at donor-acceptor interface in organic photocell. *Phys. Chem. Chem. Phys.* **17**, 12538–12544 (2015).
75. Vandewal, K. *et al.* Efficient charge generation by relaxed charge-transfer states at organic interfaces. *Nat. Mater.* **13**, 63–68 (2014).
76. Offermans, T., Meskers, S. C. J. & Janssen, R. A. J. Time delayed collection field experiments on polymer: Fullerene bulk-heterojunction solar cells. *J. Appl. Phys.* **100**, (2006).

77. Bakulin, A. A. *et al.* The Role of Driving Energy and Delocalized States for Charge Separation in Organic Semiconductors. *Science* (80-.). **335**, 1340–1344 (2012).
78. Deibel, C., Strobel, T. & Dyakonov, V. Origin of the efficient polaron-pair dissociation in polymer-fullerene blends. *Phys. Rev. Lett.* **103**, 1–4 (2009).
79. Bartesaghi, D. *et al.* Competition between recombination and extraction of free charges determines the fill factor of organic solar cells. *Nat. Commun.* **6**, 7083 (2015).
80. Firdaus, Y. *et al.* Key Parameters Requirements for Non-Fullerene-Based Organic Solar Cells with Power Conversion Efficiency >20%. *Adv. Sci.* **6**, 1802028 (2019).
81. Kozlov, O. V. *et al.* Ultrafast Exciton-to-Polaron Conversion in Densely Packed Small Organic Semiconducting Molecules. *Adv. Opt. Mater.* **5**, 1700024 (2017).
82. Kozlov, O. V. *et al.* Triphenylamine-Based Push–Pull Molecule for Photovoltaic Applications: From Synthesis to Ultrafast Device Photophysics. *J. Phys. Chem. C* **121**, 6424–6435 (2017).
83. Serbenta, A., Kozlov, O. V., Portale, G., van Loosdrecht, P. H. M. & Pshenichnikov, M. S. Bulk heterojunction morphology of polymer:fullerene blends revealed by ultrafast spectroscopy. *Sci. Rep.* **6**, 36236 (2016).
84. Kozlov, O. V. *et al.* Ultrafast Charge Generation Pathways in Photovoltaic Blends Based on Novel Star-Shaped Conjugated Molecules. *Adv. Energy Mater.* **5**, 1401657 (2015).
85. Pavelyev, V. G. *et al.* Charge Transfer Dynamics in Donor–Acceptor Complexes between a Conjugated Polymer and Fluorene Acceptors. *J. Phys. Chem. C* **118**, 30291–30301 (2014).
86. He, Y. *et al.* Unraveling the Charge-Carrier Dynamics from the Femtosecond to the Microsecond Time Scale in Double-Cable Polymer-Based Single-Component Organic Solar Cells. *Adv. Energy Mater.* **12**, 2103406 (2022).
87. Cabanillas-Gonzalez, J., Grancini, G. & Lanzani, G. Pump-Probe Spectroscopy in Organic Semiconductors: Monitoring Fundamental Processes of Relevance in Optoelectronics. *Adv. Mater.* **23**, 5468–5485 (2011).
88. Davydova, D., de la Cadena, A., Akimov, D. & Dietzek, B. Transient absorption microscopy: advances in chemical imaging of photoinduced dynamics. *Laser Photon. Rev.* **10**, 62–81 (2016).
89. Liu, Y., Zuo, L., Shi, X., Jen, A. K.-Y. & Ginger, D. S. Unexpectedly Slow Yet Efficient Picosecond to Nanosecond Photoinduced Hole-Transfer Occurs in a Polymer/Nonfullerene Acceptor Organic Photovoltaic Blend. *ACS Energy Lett.* **3**, 2396–2403 (2018).
90. Kahmann, S., Gomulya, W., Loi, M. A. & Mura, A. Donor–acceptor photoexcitation dynamics in organic blends investigated with a high sensitivity pump–probe system. *J. Mater. Chem. C* **6**, 10822–10828 (2018).



Chapter 2. Excited State Dynamics and Exciton Diffusion in Triphenylamine-based Small Push–Pull Molecule

Triphenylamine-based small push-pull molecules have recently attracted substantial research attention due to their unique optoelectronic properties. Here, we investigate the excited state dynamics and exciton diffusion in a TPA-T-DCV-Ph-F small molecule, which has a simple chemical structure with asymmetrical architecture, and end-capped with an electron-withdrawing *p*-fluorodicyanovinyl group. The excited-state lifetime in diluted solutions (0.04 ns in toluene and 0.4 ns in chloroform) are found to be significantly shorter than the solid state (3 ns in PMMA matrix). Time-dependent density functional theory indicates that this behavior originates from non-radiative relaxation of the excited state through a conical intersection between the ground and singlet excited state potential energy surfaces. Exciton diffusion length of ~16 nm in solution processed films was retrieved by employing time-resolved photoluminescence volume quenching measurements with Monte Carlo simulations. As means of investigating the device performance of TPA-T-DCV-Ph-F, we manufactured solution- and vacuum-processed bulk heterojunction solar cells that yielded efficiencies of ~1.5% and ~3.7%, respectively. Our findings demonstrate that the short lifetimes in solutions does not hinder *per se* long exciton diffusion length in films, thereby granting the use of TPA-T-DCV-Ph-F and similar push-pull molecules in vacuum- and solution-processable devices.

This chapter is based on the following publications:

[Benedito A. L. Raul](#), Yuriy N. Luponosov, Wenyan Yang, Nikolay M. Surin, Olivier Douhéret, Jie Min, Thomas L. C. Jansen, Sergei A. Ponomarenko, and Maxim S. Pshenichnikov, *Scientific Reports* 10, 21198 (2020)

Pablo Simón Marqués, José María Andrés Castán, [Benedito A. L. Raul](#), Giacomo Londi, Ivan Ramirez, Maxim S. Pshenichnikov, David Beljonne, Karsten Walzer, Martin Blais, Magali Allain, Clément Cabanetos, and Philippe Blanchard, *Chemistry–A European Journal* 26, 16422-16433 (2020)

2.1 Introduction

Small donor-acceptor conjugated push-pull molecules (D- π -A) represent an outstanding class of materials due to their inherent low-energy intramolecular charge-transfer band in the visible to near-infrared region, sometimes with, aggregation induced emission or thermally-activated delayed fluorescence properties. As a result, they have been used in various electronic and optoelectronic applications in nonlinear optics^{1,2}, organic light-emitting diodes³, bio-imaging⁴, dye-sensitized solar cells^{5,6} and organic solar cells (OSCs)^{7,8}. In particular, related dipolar systems based on triphenylamine (TPA) as electron-donating building block providing good hole-transporting properties⁹, have been extensively investigated for preparation of efficient donor materials for organics photovoltaics^{10,11}.

TPA-based compounds offer many attractive advantages over their polymer counterparts, such as vacuum- and solution-processability, easy synthesis and purification, allowing for flexibility in molecular design, and better batch-to-batch reproducibility^{12–14}. Kozlov *et al.* demonstrated that such materials provide the possibility of long exciton diffusion length¹⁵, and their push-pull character facilitates efficient intra- and intermolecular charge separation¹⁶, which can potentially lead to high values of open-circuit voltage¹⁵ as charge carrier generation might be achieved without the need of an external acceptor material. These properties make TPA-based materials promising candidates for commercial-scale applications.

Despite extensive research on TPA-based small molecules, there are few experimental and theoretical studies that investigate their excited state photophysical behavior^{12,16–21}. Specifically, studies geared towards understanding the ultrafast photo-induced processes in solution and the corresponding correlation to the solid-state have not been thoroughly addressed. Thus, a detailed knowledge about the underlying mechanism governing the excited state dynamics in such materials is of utmost research importance to further improve the molecular design and push the frontier of device performance to the next level^{22–24}.

In this Chapter, we report on the excited-state relaxation pathways and exciton diffusion dynamics in a TPA-based small molecule (TPA-T-DCV-Ph-F). We demonstrate that the excited-state lifetime in solution is ~ 0.04 ns in toluene and ~ 0.4 ns in chloroform, which is substantially shorter than ~ 3 ns in the PMMA matrix. This unusual behavior is attributed to excited-state non-radiative depopulation via conical intersection between the ground- and excited-state potential energy surfaces. Through time-resolved photoluminescence (PL) volume-quenching experiments and

Monte Carlo simulations, the exciton diffusion length in solution processed films of TPA-T-DCV-Ph-F is obtained as ~16 nm and found to be limited by the energetic disorder. To study the potential of TPA-T-DCV-Ph-F as a donor material in OSCs, vacuum- and solution-processed solar cells were manufactured with 3.7% and 1.5% power conversion efficiencies (PCE), respectively. The obtained results suggest that the TPA-T-DCV-Ph-F molecule has promising properties for organic optoelectronics provided that the energetic disorder is reduced.

2.2 Results and Discussion

2.2.1 Material Properties

Fluorination of chemical blocks in conjugated systems is regarded as a promising tool for controlling intramolecular and intermolecular interactions^{25–29}. The phase behavior, glass transition temperature and crystallinity of conjugated molecules can be precisely tuned by adjusting the number and positions of fluorine atoms. Furthermore, incorporating fluorine atoms into the chemical structure can effectively modulate the optical and optoelectronic properties, and therefore affect the device performance.

The synthetic route to TPA-T-DCV-Ph-F (Figure 2.1) consists of two steps and is similar to its non-fluorinated analog TPA-T-DCV-Ph¹⁵. The synthesis details can be found in reference [30].

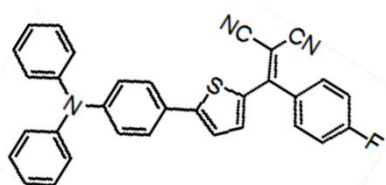


Figure 2.1. Chemical structure of TPA-T-DCV-Ph-F.

TPA-T-DCV-Ph-F has good solubility in chloroform and in commonly used organic solvents, such as toluene, tetrahydrofuran and chlorobenzene³⁰; making the compound highly attractive for solution-processed organic optoelectronics.

TPA-T-DCV-Ph-F exhibits excellent thermal stability in both air and nitrogen with high decomposition temperatures of 389 °C and 397 °C, respectively³⁰, which is similar to that of its analog TPA-T-DCV-Ph¹⁵.

2.2.2 Excited State Dynamics in Solution

The absorption and PL spectra of TPA-T-DCV-Ph-F in diluted solutions (toluene and chloroform) and in poly (methyl methacrylate) (PMMA) matrix are depicted in Figure 2.2a. The dispersed TPA-T-DCV-Ph-F molecules in the PMMA matrix are used as a proxy to mimic solutions with restriction of any potential photo-induced molecular motions, while still preventing intermolecular interactions^{16,21}. The absorption spectra consist of two typical bands (at ~300 nm and ~500 nm) for push-pull molecules^{17,31}. These bands have been previously indicated to have a mixed character due to the π - π^* transition in the conjugated triphenyl-thiophene fragment and intramolecular charge transfer between the electron-donating and electron-withdrawing groups^{17,31}.

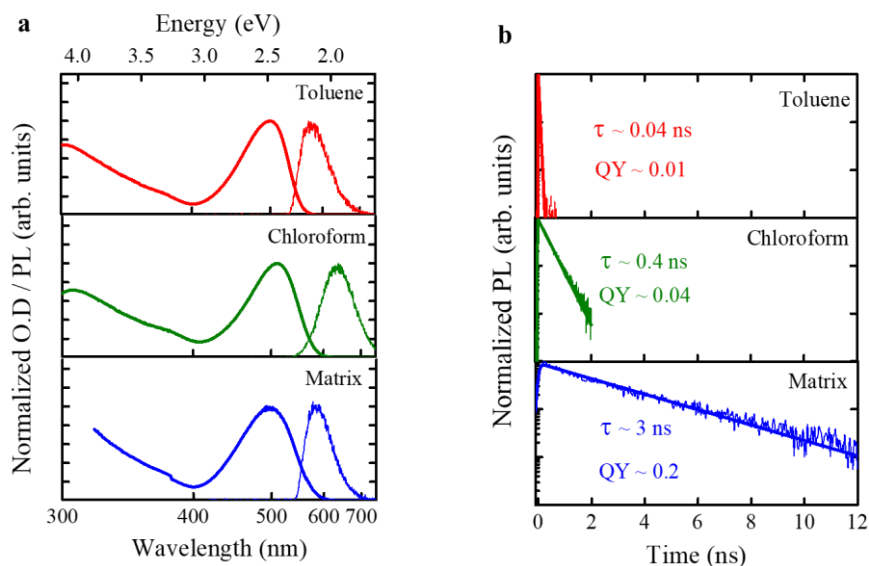


Figure 2.2. (a) Absorption (thick solid lines) and PL spectra (thin solid lines) of TPA-T-DCV-Ph-F in toluene solution, chloroform solution (green), and in PMMA matrix (blue). (b) Experimental TPA-T-DCV-Ph-F PL transients (thin solid lines) in toluene solution (red), chloroform solution (green) and in PMMA matrix (blue), obtained by integrating the PL maps (Section 2.5.1) in the 620-700 nm spectral range. The thick solid lines represent the results of mono-exponential fitting. The decay times and respective PL quantum yields (QY) are indicated next to the transients.

The PL spectra were obtained upon excitation near the absorption maximum (~520 nm) for optimal light absorption; the Stokes shift values are ~0.34 eV in toluene and ~0.48 eV in chloroform. The larger Stokes shift in chloroform as compared to toluene is attributed to the higher polarity of the former that leads to increased energy relaxation to longer wavelengths^{32,33}. The absorption and PL spectra maxima peak positions of the molecules dispersed in the PMMA matrix are slightly shifted compared to the diluted solutions, which is also attributed to the difference in medium polarizability^{16,21}.

Figure 2.2b shows the PL transients of TPA-T-DCV-Ph-F in solutions and in PMMA matrix with the respective independently measured PL quantum yield (QY) values. The PL transients are fitted with a mono-exponential function convoluted with a Gaussian apparatus function. Exponential fitting of the PL transients in solution yielded lifetime values of ~0.04 ns in toluene and ~0.4 ns in chloroform, consistent with increased PL QY from 0.01 to 0.04 in toluene and chloroform, respectively. Short lifetimes and low PL QYs suggest prevalence of non-radiative relaxation channels.

TPA-T-DCV-Ph-F undergoes a strong change in dipole moment upon photoexcitation, with the electron density mostly delocalized on the acceptor unit DCV-Ph-F and in part on the thiophene linker (Section 2.5.2). This causes substantial reorientation of the polar solvent (such as chloroform with a dipole moment of 1.1 D³⁴) around TPA-T-DCV-Ph-F molecules¹²; in the less polar toluene (dipole moment of 0.3 D³⁴), the effect is much weaker. Thus, the excited-state lifetimes and the PL QYs appear to be correlated with solvent polarity. These results are in agreement with earlier studies performed on other dissolved molecules in solvents with descending polarities, in which it was also found that the PL lifetime becomes shorter in less polar solvents^{33,35}. It was suggested^{33,35} that the higher dipole moment of the solvent tends to stabilize the conformational changes at the excited state due to stronger solvent-fluorophore dipole-dipole interaction, causing by this manner the reduction in non-radiative decay and the subsequent increase in lifetime.

To demonstrate the applicability of this scenario, we dispersed TPA-T-DCV-Ph-F molecules in a PMMA matrix to restrain possible molecular conformations^{16,21}. This resulted in a much longer excited state lifetime of ~3 ns with the corresponding increase in PL QY (Figure 2.2b). Similar behavior (known as solid state luminescence enhancement) has been previously reported^{36,37} and assigned to a conical intersection (CI) between excited and ground states of the molecule in the liquid phase (see Section 2.5.6 for more on materials with CI). To support such

scenario for the TPA-T-DCV-Ph-F molecule, our collaborator (Thomas L. C. Jansen) performed time-dependent density functional theory (TDDFT).

2.2.3 TDDFT Calculations

The TDDFT calculation details can be found in reference [30]. Two unbound degrees of freedom were identified in the excited-state potential. One involves rotation of the thiophene (Figure 2.3a), the other involves motion of the nitrogen atoms in the DCV moiety and rearrangements around the TPA donating group at the other end of the molecule (Figure 2.3b). The unbound degrees of freedom on the Franck-Condon point of the excited-state surface demonstrate that in the excited-state, this geometry is not a local minimum, and the molecule can be expected to move when excited³⁸. Further analysis is needed to identify the excited-state potential minimum.

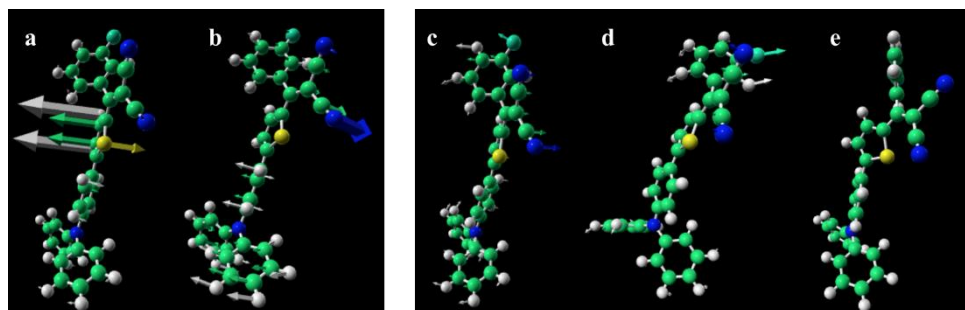


Figure 2.3. Structures and motion of TPA-T-DCV-Ph-F in the excited states. Two unbound degrees of freedom identified in the excited state at the Frank-Condon point with imaginary frequency of $27i$ (a) and $88i$ cm^{-1} (b). The arrows indicate atomic movements towards the CI. (c) The structure of the lowest energy configuration. (d) The structure identified near the conical intersection. (e) The local minimum configuration on the ground state potential energy surface identified from the energy minimization on the ground state potential energy surface starting from the conical intersection point. The arrows in (c) indicate the atomic movement towards the conical intersection structure shown in (d), while the arrows in (d) indicate the atomic movement towards the local minimum in (e). In all panels, the light green atoms are carbon, white is hydrogen, blue is nitrogen, yellow is sulfur and cyan is fluorine.

Geometry optimization on the excited-state potential energy surface starting in the ground-state minimum configuration (Figure 2.3c) deforms the molecule and leads to a geometry where the TDDFT calculations do not converge (Figure 2.3d). This is because in this geometry the ground state and lowest excited state are near-degenerate, causing the TDDFT procedure to fail. Thus, we propose that this geometry is close to a CI. From the CI geometry, further geometry optimization on the ground-state potential surface leads to a new ground-state geometry (Figure 2.3e) with a slightly higher energy than the original geometry. This demonstrates that the molecule has at least one CI and at two stable configurations on the ground-state potential energy surface. The atomic movements (indicated by arrows) have a large resemblance to the $27i$ cm^{-1} mode (Figure 2.3b), suggesting that this mode indeed plays a crucial role in photo-isomerization.

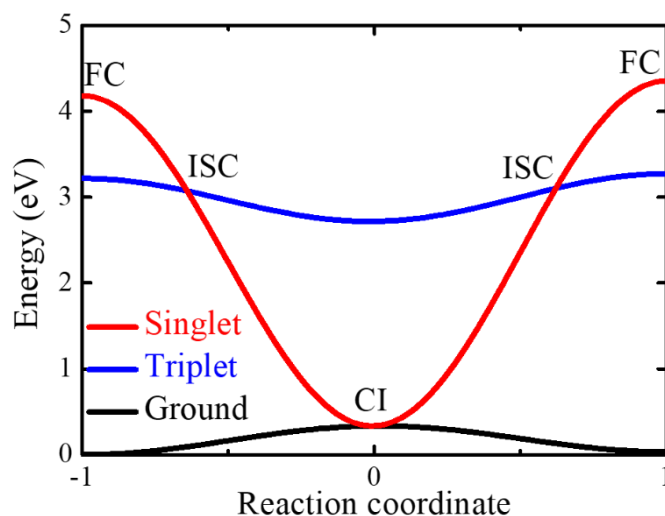


Figure 2.4. Illustration of energies along potential energy surfaces. The red, blue, and black lines represent the energies of the singlet excited-state, the triplet excited-state, and the ground state, respectively. FC represents the Franck-Condon points, CI is the conical intersection position, and ISC represents the singlet-triplet states intersystem crossing positions. The effective reaction coordinate indicates consecutive excited-state configurations.

The potential energy surfaces of the lowest electronic states and the ground state as obtained by interpolation between energies obtained for the initial CI, and final geometries are illustrated in Figure 2.4. The energy crossing point is observed between the singlet excited state and the ground state, indicating a non-radiative de-

excitation transition at the estimated CI position. The exact energy of the crossing point may be higher as the CI geometry was assigned in the excited-state geometry optimization when the TDDFT calculation stopped converging. Although excited-state relaxations involving CI often happen on sub-picosecond timescales³⁹, for the TPA-T-DCV-Ph-F molecule dissolved in toluene, the timescale is ~40 ps. In a rigid environment, where the relatively large molecular deformation required to reach the CI is efficiently suppressed, the relaxation process should be significantly slower, as observed in the experiments above and in Section 2.5.6.

Figure 2.4 also shows the energy crossing points between the singlet excited-state and the lowest triplet excited-state, thereby potentially allowing intersystem crossing (ISC). We did not explicitly calculate the rates for ISC and CI; however, ISC requires quantum-mechanical perturbations to flip the spin such as spin-orbit coupling induced by heavy metals, or to a lesser degree by out-of-plane vibrations. The TPA-T-DCV-Ph-F molecule does not contain heavy atoms, and we presume that the contributions from out-of-plane vibrations for ISC to be minimal. Thus, the rate for ISC is expected to be low (typically sub-0.1 ns⁻¹)⁴⁰, such that the transition through the CI is likely much faster.

2.2.4 Excited State Lifetime and Energetic Disorder in Film

After establishing that the excited-state lifetime of the isolated TPA-T-DCV-Ph-F molecule varies from 40 ps in toluene solution to 3 ns in a PMMA matrix, we shift to TPA-T-DCV-Ph-F films where conformational movements of the molecule are restricted but intermolecular interactions become important. Figure 2.5a shows the PL transient of TPA-T-DCV-Ph-F solution processed neat film. The bi-modal behavior of the PL transient indicates that several photophysical processes contribute to the excited state dynamics. The fast decay is attributed to intermolecular energy transfer⁴¹, with possible contributions from non-radiative decay induced by excitonic traps^{42–44}.

The PL transient was fitted with a bi-exponential function convoluted with a Gaussian apparatus function of ~10 ps. The average excited state lifetime was determined as $\tau_{av} = \frac{\sum_i a_i t_i^2}{\sum_i a_i t_i}$, where a_i represents the pre-exponential factor and t_i is the time constant. The weighted-average exciton lifetime was determined to be ~3.7 ns and the measured PL QY was ~0.17. These values are similar to those obtained in

the PMMA matrix, further substantiating our previous findings that photo-induced molecular conformations are mostly restricted in the solid state.

Exciton diffusion in a disordered medium is primarily characterized by downhill migration toward lower energetic sites, which results in a dynamical red-shift of PL⁴⁵. The total shift of PL mean energy stabilizes at $\Delta E_{PL} = E_{PL}(t = 0) - E_{PL}(t = \infty) \cong \frac{\sigma^2}{kT}$, where σ is the standard deviation of the Gaussian density of states (energetic disorder). Here the quasi-equilibrium is reached and thermally activated hopping mainly contributes to the diffusion process⁴⁵. Figure 2.5b depicts the experimentally tracked dynamical PL mean energy for each time step. The total PL mean energy shift is $\Delta E_{PL} \sim 155$ meV, so that $\sigma \sim 65$ meV (at room temperature, $kT \sim 25$ meV).

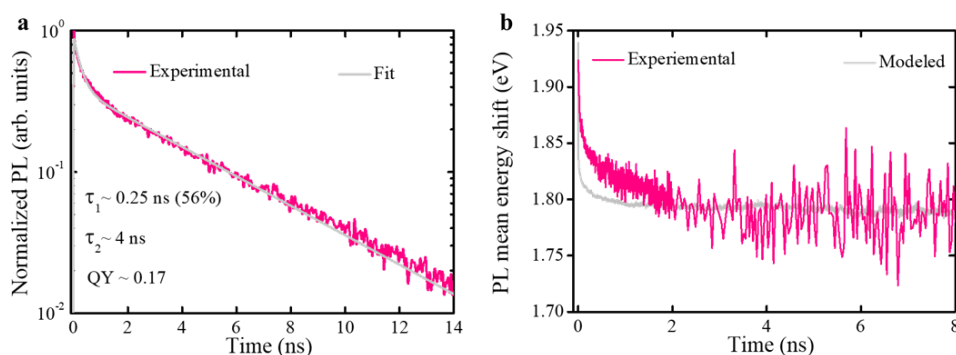


Figure 2.5. (a) PL transient of neat film, obtained by stitching the fast (< 2 ns) and slow (< 14 ns) transients after respective integrations of PL maps in the 550-840 nm range (Section 2.5.3). The solid pink line represents the experimental data, the solid gray line represents the result of bi-exponential fitting. The fitting parameter and PL QY are indicated next to the transient. (b) Experimental (solid pink line) and Monte Carlo modeled (solid gray line) dynamical shift of PL mean energy. The experimental data was obtained by stitching fast (< 2 ns) and slow dynamics (< 14 ns). As the density of states in the simulations is centered at 0 eV, we blue-shifted the Monte Carlo simulation value by 1.95 eV to match the experimental conditions. For clarity, the data is shown up to 8 ns as there are no changes afterward.

2.2.5 Exciton Diffusion Length and Coefficient

As means of acquiring quantitative information about the temporal and spatial evolution of the excited state population in solution processed films of TPA-T-DCV-Ph-F, we performed time-resolved PL volume-quenching experiments and Monte Carlo simulations, out of which the exciton diffusion length and exciton diffusion coefficient were determined^{46,47}.

The commonly used acceptor in OSCs [6,6]-Phenyl- C_{61} -butyric acid methyl ester (PC₆₀BM) was used as a quenching molecule. The neat film and films mixed with different content of PC₆₀BM molecules (0.11%, 0.27% and 0.55% molar fractions) were prepared by spin-coating. The respective PL transients are shown in Figure 2.6a. As expected, concentration increase of the quencher causes acceleration on the PL transients decay due to the diffusion-limited exciton quenching⁴⁶.

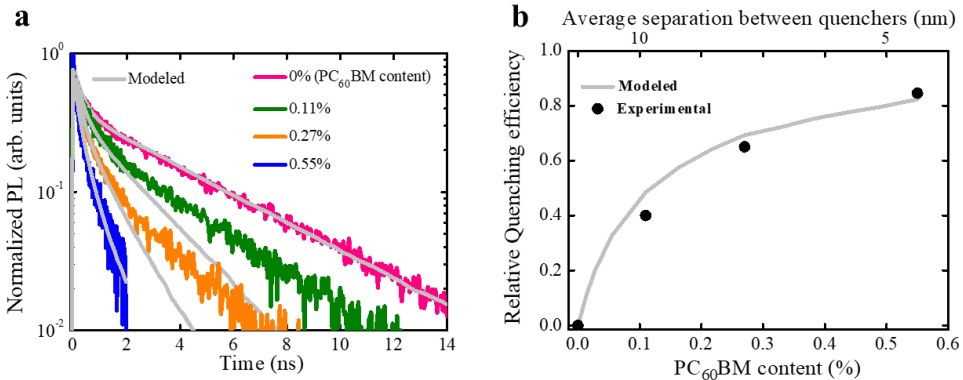


Figure 2.6. (a) Experimental PL transients of neat film and films with different PC₆₀BM content. The respective modeled PL transients from Monte Carlo simulations are depicted in solid gray lines. The input parameters are presented in Section 2.5.5. (b) Relative quenching efficiency versus PC₆₀BM content. The black circles represent the experimental results, the gray line represents the modeled results. The average separation between PC₆₀BM molecules was determined as described in Section 2.5.5.

To quantify the quenching process, we plotted the PL quenching efficiency vs. PC₆₀BM content (Figure 2.6b). The PL quenching efficiency was determined as⁴⁸:

$$Q = 1 - \frac{\int \text{PL}_{\text{quenched}} dt}{\int \text{PL}_{\text{neat}} dt} \quad (2.1)$$

where Q is the PL quenching efficiency, PL_{quenched} is the PL transient for the samples with different $PC_{60}BM$ content, PL_{neat} is the PL transient for the neat film. A quenching efficiency near to zero indicates of minimal exciton quenching, which occurs when the average quencher separation is much greater than the exciton diffusion length. Significant quenching occurs when the average quencher separation is less than the exciton diffusion length.

The experimental measured PL transients were modeled using Monte Carlo simulations of a 3D exciton random walk in a cubic grid (for more details, see Section 2.5.5). As the energetic disorder was obtained earlier, the modeled PL transients (Figure 2.6a) were used to extract the exciton hopping time ($\tau \sim 0.1$ ps), which was the only fit parameter. The PL quenching efficiencies (Figure 2.6b) were calculated using the modeled PL transients. The simulated and experimental results are in good agreement; some discrepancies observed might be attributed to the non-homogenous distribution of $PC_{60}BM$ quencher molecules in the films or even possibly due to the formation of small $PC_{60}BM$ clusters, as reported by Mikhnenko *et al*⁴⁸. The discrepancy only affects a small population of the excited state ($\sim 10\%$); therefore, it has little effect on the obtained results. The dynamical PL mean energy shift (Figure 2.5b) is also satisfactorily described, with some inconsistency at early times most probably caused by the limited resolution of the streak-camera.

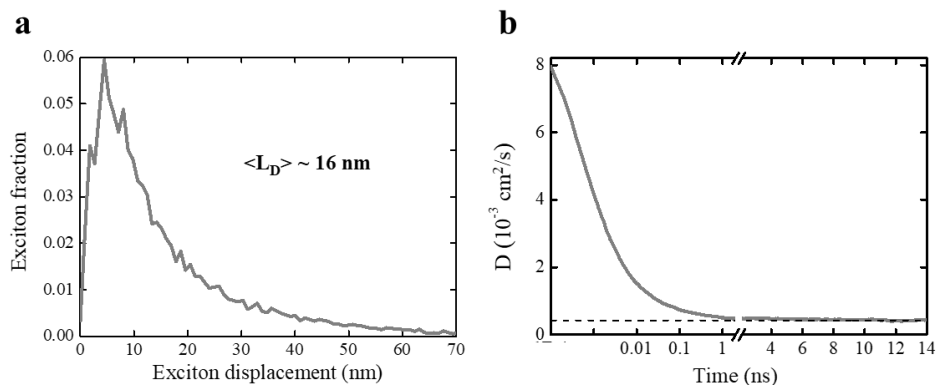


Figure 2.7. (a) Monte-Carlo simulated distribution of exciton displacement in neat thin films of TPA-DVC-Ph-F. (b) Time dependent diffusion coefficient. The dashed line indicates the value where the diffusion coefficient is stabilized at $D \sim 4.2 \times 10^{-4} \text{ cm}^2/\text{s}^{-1}$. The first 2 ns are presented in the log scale.

The Monte Carlo simulation data were used to extract the exciton diffusion length and exciton diffusion coefficient values. An exciton diffusion length of ~16 nm was derived from the exciton displacement statistics as the mean value of displacement (Figure 2.7a). In disordered organic semiconductors, exciton diffusion length typically ranges from 5 nm to 20 nm^{19,49,50}; hence, the 16 nm exciton diffusion length in TPA-T-DCV-Ph-F falls into the longer end of the range. This is attributed to the long exciton average lifetime of ~3.7 ns and the relatively low energetic disorder of ~65 meV.

The differential form of the Einstein-Smoluchowski relation (Section 2.5.5) was used to obtain the time-dependence of the exciton diffusion coefficient (Figure 2.7b). The early times (< 0.1 ns) are dominated by fast exciton cooling followed by slower diffusion where the thermal quasi-equilibrium is reached at exciton diffusion coefficient value of $D \sim 4.2 \times 10^{-4} \text{ cm}^2\text{s}^{-1}$. For comparison, a diffusion coefficient of $D \sim 3.5 \times 10^{-3} \text{ cm}^2\text{s}^{-1}$ was obtained in highly ordered (energetic disorder of < 5 meV) vacuum-deposited C₇₀⁵¹. According to the Monte Carlo simulations, had the energetic disorder been reduced from 65 meV to 5 meV in solution-processed TPA-T-DCV-Ph-F films, the exciton diffusion length would have been 50 nm. Thus, the energetic disorder of ~65 meV limits the exciton diffusion coefficient (and exciton diffusion length) in TPA-T-DCV-Ph-F solution processed films. To overcome this limitation, the energetic disorder should be reduced; this can potentially be achieved by molecular encapsulation^{52,53}.

2.2.6 Device Performance

To study the potential use of TPA-T-DCV-Ph-F as a donor material in OSCs, our collaborators fabricated solution-processed devices^{30,54}, where [6,6]-Phenyl-C₇₁-butyric acid methyl ester (PC₇₀BM) was chosen as the electron-acceptor material. Figure 2.8a shows the current-density-voltage (J - V) curves of the optimized device and the corresponding photovoltaic parameters.

It has been demonstrated that in solution-processed BHJ OSCs with non-optimal morphology, a gradual increase in exciton diffusion length was followed by an increase in short-circuit current when the film crystallinity and roughness were improved through meticulous post-deposition treatments^{55,56}. Hence, we speculate that the shorter exciton diffusion length of ~16 nm in solution-processed TPA-T-DCV-Ph-F films (compared to an exciton diffusion length of ~25 nm in vacuum-evaporated films of its non-fluorinated analog TPA-T-DCV-Ph¹⁵), limits the device

short-circuit current density (J_{sc}) to $\sim 4.87 \text{ mA cm}^{-2}$. To support this supposition, our collaborators fabricated vacuum-processed BHJ devices³⁰ and obtained higher J_{sc} of $\sim 8.06 \text{ mA cm}^{-2}$ (Figure 2.8b), probably indicating improvements in film morphology³⁰.

The obtained results demonstrate the potential use of simple TPA-T-DCV-Ph-F molecules in both vacuum- and solution-processed organic optoelectronics devices.

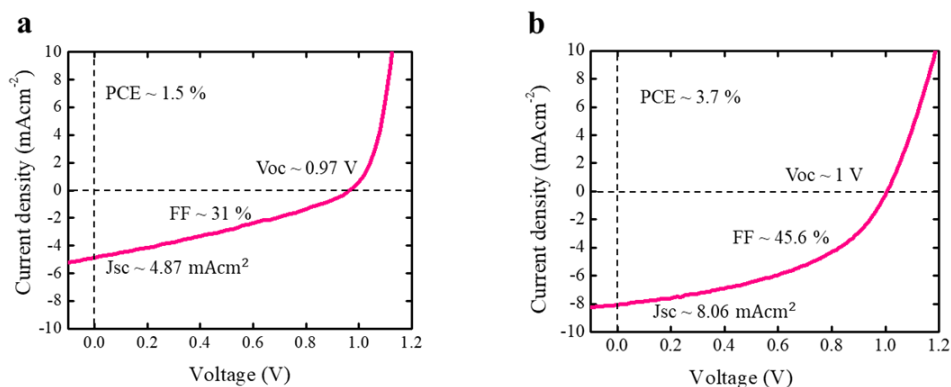


Figure 2.8. (a) Solution processed OSC J - V characteristics and photovoltaic parameters. (b) Vacuum processed OSC J - V characteristics and photovoltaic parameters.

2.3 Conclusions

In this Chapter, we investigated the excited-state and exciton dynamics of a small push-pull molecule TPA-T-DCV-Ph-F. The experimental results revealed that the excited-state lifetime in solutions (0.04 ns in toluene and 0.4 ns in chloroform) are shorter than in the solid state (3 ns in PMMA matrix). With the support of TDDFT calculations, we concluded that this phenomenon is attributed to excited-state non-radiative depopulation in solution from conical intersection between the ground and singlet excited state potential energy surfaces. Furthermore, from time-resolved PL and Monte Carlo simulations we extracted exciton diffusion length of $\sim 16 \text{ nm}$ in solution-processed layer of TPA-T-DCV-Ph-F. To investigate the potential of TPA-T-DCV-Ph-F as donor material in OSCs, our collaborators manufactured vacuum and solution processed solar cells that yielded efficiencies of $\sim 3.7\%$ and 1.5% , respectively. Our findings shed light on the photophysics of TPA-T-DCV-Ph-F and pave the way for vacuum- and solution-processable TPA/DCV-based materials with long exciton diffusion lengths for organic optoelectronics applications.

2.4 Methods

2.4.1 Sample Preparation

Solutions for the neat and mixed thin films were separately prepared using chloroform at a concentration of 10 g/L for TPA-T-DCV-Ph-F and 0.02-0.04 g/L for PC₆₀BM, and stirred for 2 hours at room temperature. The solutions were mixed to achieve the desired PC₆₀BM /TPA-T-DCV-Ph-F molar ratios (0.11%, 0.27%, and 0.55%) and stirred for another 2 hours. The films were prepared by spin-coating the solution in a plain glass substrate (1cm x 1cm). For the matrix, PMMA (Sigma Aldrich, Mw= 120000 g/mol) was dissolved in chloroform at a concentration of 150 g/L and stirred at room temperature for 8 hours. TPA-T-DCV-Ph-F and PMMA solutions were mixed to achieve TPA-T-DCV-Ph-F/PMMA volume ratio of 0.2, and stirred for 2 hours. The matrix was prepared by spin-coating the solution in a plain glass substrate. For highly diluted solutions in toluene and chloroform, the concentrated solutions (10 g/L) were further diluted to obtain optical densities in range of 0.06 to 0.12 at absorption maximum in a 2 mm quartz cuvette.

2.4.2 Time-resolved Photoluminescence, Absorption and Quantum Yield

Time-resolved PL measurements were performed using a streak camera (Hamamatsu, C5680) and a spectrograph. To measure the early time dynamics (< 2 ns), the mode-locked output from the Ti: sapphire oscillator (Mira 900, 76 MHz repetition rate) was focused on the Newport SGC-800 hollow fiber producing a supercontinuum. The excitation wavelength of 520 nm (or 580 nm) was obtained by selecting a portion of the supercontinuum with a bandpass filter with a central wavelength of 520 nm (or 580 nm) and FWHM of 10 nm. For the slower dynamics (< 14 ns), a pulse picker was used to lower the repetition rate of the Ti: sapphire oscillator from 76 MHz to 2 MHz. A long-pass filter was placed before the spectrograph to filter the stray excitation light. The excitation power was set between 0.5 μ W and 4 μ W to prevent exciton-exciton annihilation and photobleaching.

The absorption spectra were obtained with a PerkinElmer Lambda 900 UV/VIS/NIR spectrometer.

The PL QY of solutions in toluene and chloroform were determined by comparing with the known QY of the standard solution of 1,4-bis(5-phenyloxazol-2-yl)benzene (POPOP) in cyclohexane (PL QY ~ 1) using the fluorescence measurement method for optically diluted solutions⁵⁷. PL QY measurements in the PMMA matrix and polycrystalline thin films were conducted using an integrating sphere.

2.5 Supplementary Information

2.5.1 Photoluminescence Maps and Dynamical Stokes Shift (of solutions and matrix)

The PL maps of TPA-T-DCV-Ph-F in toluene solution, chloroform solution, and in the PMMA matrix are depicted in Figure 2.9a, and the respective dynamical Stokes shifts are shown in Figure 2.9b. The dynamical Stokes shift in toluene (40 meV) is less than the shift in chloroform (100 meV), further demonstrating that with an increase in solvent polarity, PL shifts to longer wavelengths. In the solid state (in the PMMA matrix) the dynamical Stokes shift is negligible (~ 0 eV) due to a lack of intermolecular interactions.

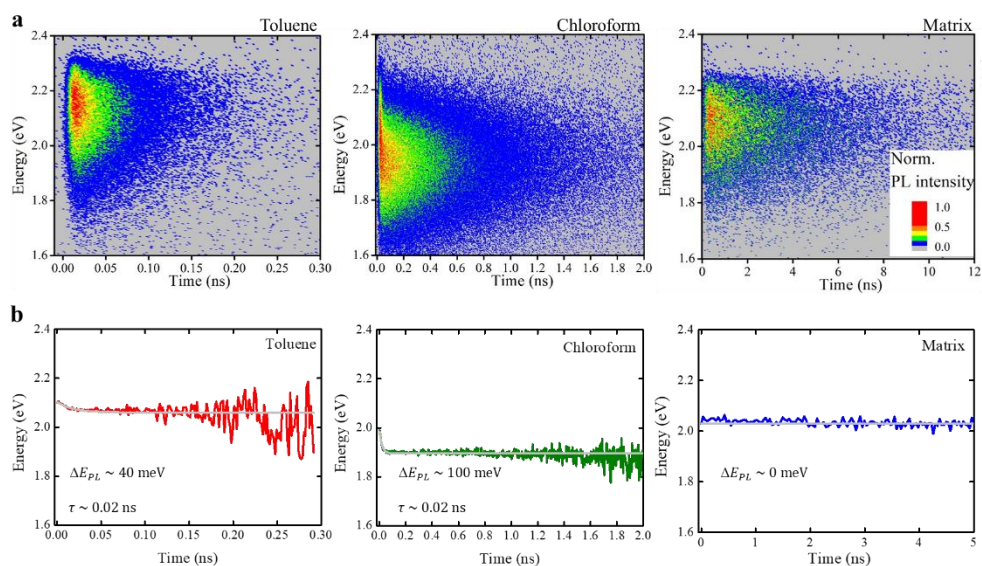


Figure 2.9. (a) PL maps of TPA-T-DCV-Ph-F in toluene solution (left), chloroform solution (middle), and in PMMA matrix (right). The PL maps are normalized to the maximum amplitudes. (b) Respective dynamical Stokes shifts calculated as the time-dependence of the mean frequency $\langle \omega(t) \rangle = \int \omega S(\omega, t) d\omega / \int S(\omega, t) d\omega$ of spectral slices $S(\omega, t)$ at time t . The gray line represents the mono-exponential fitting, with the fitting values indicated next to the transients.

2.5.2 Molecular Orbital Calculations

The HOMO and LUMO levels calculated in chloroform and toluene are identical. The calculation details can be found in reference [30].

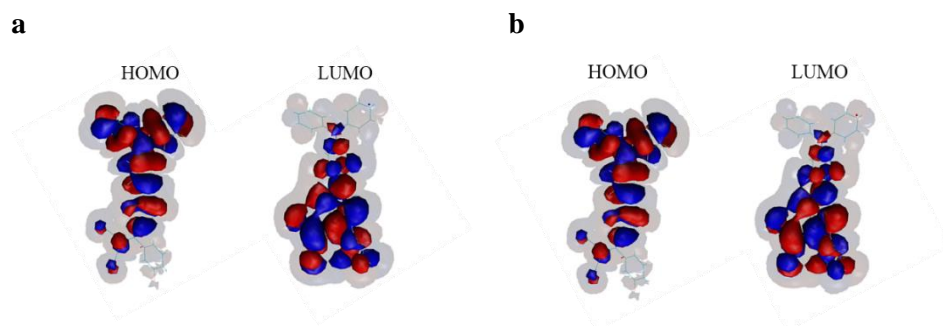


Figure 2.10 Representation of HOMO and LUMO electron density in (a) chloroform solution, and in (b) toluene solution.

2.5.3 Photoluminescence Maps of Neat Film

Figure 2.11 shows the stitched PL maps for the fast (< 2 ns) and slow dynamics (< 14 ns).

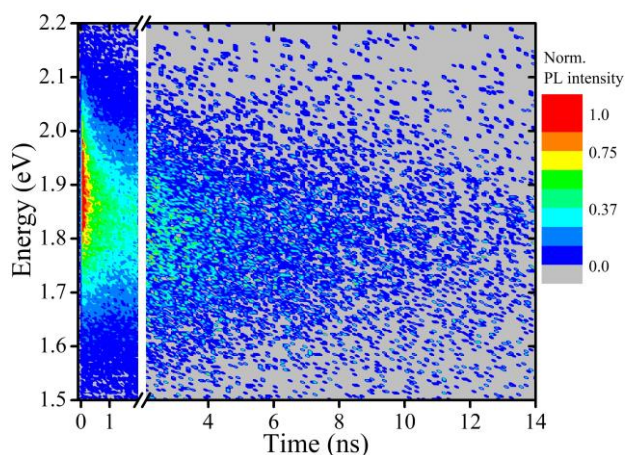


Figure 2.11 Stitched PL maps of TPA-T-DCV-Ph-F neat film. The break separates the experimental data obtained at different streak-camera time bases.

The PL maps were spectrally integrated (in 2.2–1.5 eV range), and the resulting transients were stitched to obtain the final transients presented in the main text. The same procedure was applied for all mixed films.

2.5.4 Average Separation between Quenchers

The average separation between quenchers was calculated as:

$$d = \sqrt[3]{\frac{M_m}{\rho N_A n_r}} = \sqrt[3]{\frac{1}{n_r}} \times 0.89 \text{ [nm]}, \quad (2.1)$$

where for TPA-T-DCV-Ph-F, $\rho \sim 1.17 \text{ g}\cdot\text{cm}^{-3}$ is the density, $M_m \sim 497 \text{ g}\cdot\text{mol}^{-1}$ is the molecular mass and 0.89 nm is the average size of the molecule. N_A is the Avogadro constant, and n_r is the quencher molar ratio with respect to TPA-T-DCV-Ph-F.

2.5.5 Monte Carlo Simulations

The Monte Carlo simulations schematics are shown in Figure 2.12.

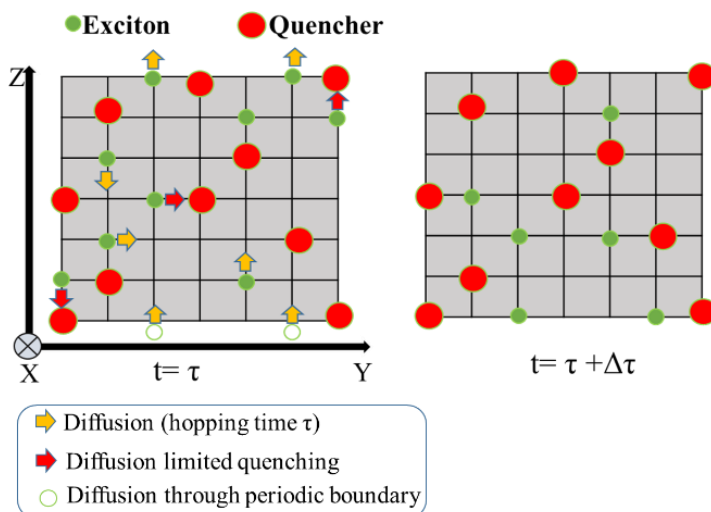


Figure 2.12 Schematics of random walk model for Monte Carlo simulations. $t = \tau$ is the exciton distribution at time τ . $t = \tau + \Delta\tau$, is the exciton distribution at the next time step.

The exciton lifetime, hopping distance and quencher content were used as the input parameters, as shown in Table 2.1. The distance between two grid points (hopping distance) was equal to the size of the molecule (~ 0.89 nm) averaged over three dimensions (see Section 2.5.4 for calculations). Each grid point was assigned an energy generated from a Gaussian distribution function centered at zero:

$$g(\varepsilon) = \frac{1}{\sigma\sqrt{2\pi}} e^{-\frac{\varepsilon^2}{2\sigma^2}}, \quad (2.2)$$

where ε is the grid point energy, and σ is the energetic disorder (standard deviation)⁴⁵.

Table 2.1. Monte Carlo Simulations parameters.

Description	Parameter	Value
Cartesian lattice grid	X-Y-Z	500-500-500
Lifetime-1 fraction	a_1	~ 0.55
Lifetime-1	τ_1	~ 0.3 ns
Lifetime-2	τ_2	~ 4.4 ns
Energetic disorder	σ	~ 65 meV
Hopping distance	d	~ 0.89 nm
Quencher fraction	QF	From 0 to 5.26×10^{-3}
Hopping time	τ	~ 0.1 ps

At the beginning of the simulation, 5000 excitons with a finite lifetime (τ_{av}) were placed randomly at different grids points. The exciton hopping probability p_{if} was set at unity if the initial grid point had an energy (E_i) higher than the final grid point energy (E_f), while for the opposite case ($E_i < E_f$) the probability was determined from a Boltzmann distribution with kT equal to ~ 25 meV (room temperature):

$$p_{if} = e^{-\frac{E_f - E_i}{kT}} \quad E_i < E_f. \quad (2.3)$$

At each time step, every quenched exciton is eliminated from the simulation. The differential form of the Einstein-Smoluchowski relation for random walk was used to obtain the time-dependence of the exciton diffusion coefficient from the known exciton displacement as

$$D(t) = \frac{\partial \langle l^2(t) \rangle}{6\partial t}, \quad (2.4)$$

where $\langle l^2(t) \rangle$ is the average square of the exciton displacement in a single step or hop, and t is the hopping time.

2.5.6 Effect of Intramolecular Acceptor Unit

To complement the investigations presented in this Chapter, time-resolved PL and pump-probe transient absorption measurements were employed to investigate the effect of variation of the intramolecular acceptor unit DCV (in TPA-T-DCV-Ph-F) to TCBD-based acceptors. The chemical structures of three TPA/TCBD-derivatives studied in this section are presented in Figure 2.13. For details about synthesis, electrochemical properties and photovoltaic performance,³⁷ see reference [37].

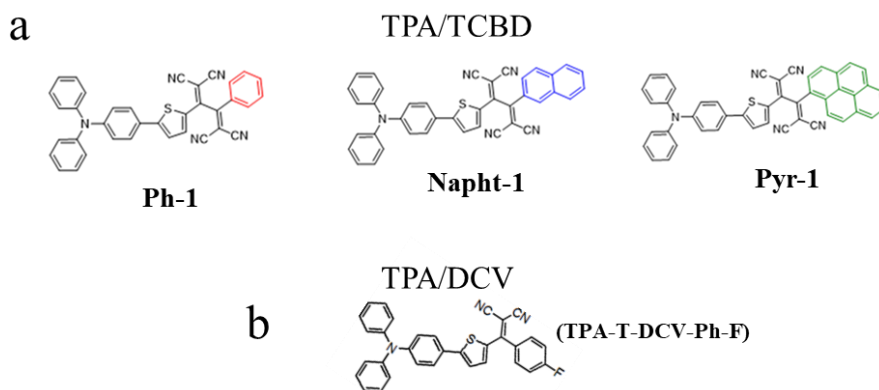


Figure 2.13. (a) Chemical structure of TPA/TCBD small molecules. (b) Chemical structure of TPA/DCV small molecules (TPA-T-DCV-Ph-F) investigated in this Chapter.

Similar to the TPA-T-DCV-Ph-F molecule (TPA/DCV), the TPA/TCBD based push-pull molecules have strong absorption in the visible spectrum (Figure 2.14a). However, with the steady state PL measurements we did not observe any photo-emission from **Ph-1**, **Napht-1**, or **Pyr-1** (ca. 10^{-6} M) in dichloromethane, chloroform, toluene, and hexane. Ultrafast time-resolved PL measurements were performed with the excitation wavelength of 580 ± 10 nm to ensure optimal light absorption and photoexcitation of the lowest excited state. However, no photo-emission was

detected. In agreement with previous investigations on other TCBD derivatives⁵⁸, all these results strongly suggest very short-lived singlet excited states in solutions, which are associated with ultrafast non-radiative relaxation through an energetically accessible conical intersection⁵⁸.

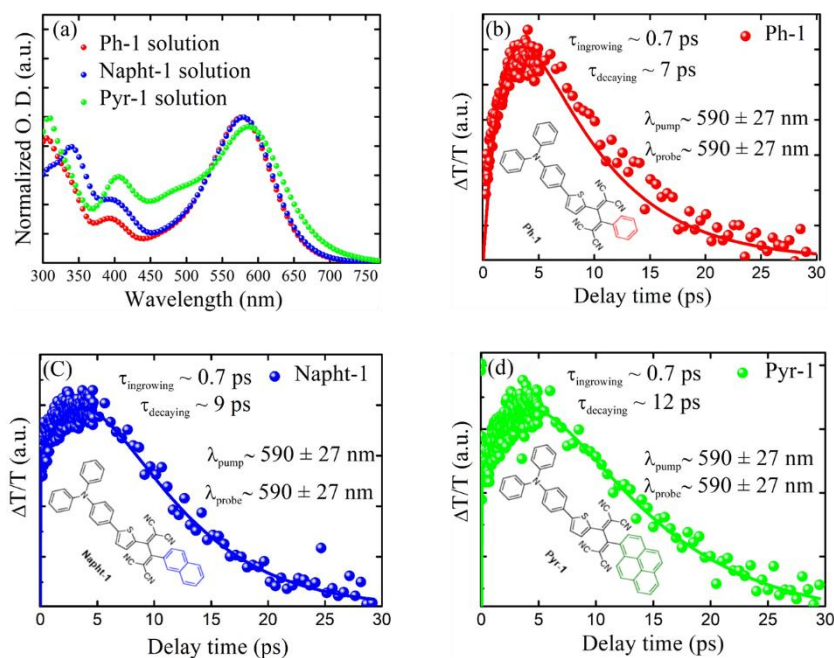


Figure 2.14. (a) Steady state absorption in solution of **Ph-1** (red), **Napht-1** (blue) and **Pyr-1** (green). Pump-probe transients in solution of **Ph-1** (red) (b), **Napht-1** (blue) (c) and **Pyr-1** (green) (d), the spheres correspond to the experimental results, while the solid lines are the exponential fitting with their respective ingrowing and decaying times. Inset is the chemical structure of respective small molecules.

Pump-probe transient absorption measurements were conducted to uncover the lack of PL of the compounds in solutions. The excitation pump and probe wavelengths were chosen in accordance with the region of interest, a central wavelength of 590 nm with a FWHM bandwidth of 27 nm. Figures 2.14b-d show the pump-probe transients consisting of an ingrowing and a decaying component. The ingrowing exponent of ~ 0.7 ps is assigned to vibrational relaxation at the excited state. The subsequent mono-exponential decay is attributed to depopulation of the excited state in ~ 10 ps. The fast excited state relaxation of ~ 10 ps combined with the lack of photo-emission, points to existence of an energetically accessible non-radiative decay channel.

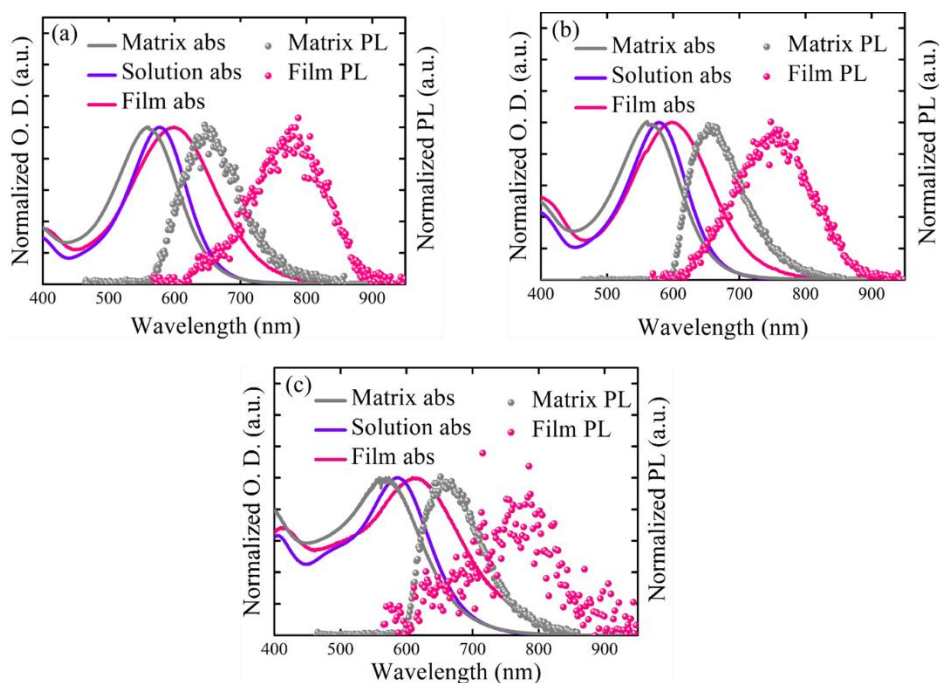


Figure 2.15. Absorption and PL spectra of (a) **Ph-1**, (b) **Napht-1** and (c) **Pyr-1**. Steady state absorption spectra of isolated donor molecules in PMMA matrix (gray), solution (violet) and in film (pink) represented by solid lines and the corresponding PL spectra of matrix (gray) and neat film (violet) represented by spheres. The PL spectra were obtained by time integrating the PL maps (Figure 2.16) over (0-0.8) ns spectral range for the neat films and (0-1.8) ns for the matrix. The excitation wavelength to obtain the PL spectra was $\sim 580 \pm 10$ nm.

As a next step, photophysical experiments were performed in the solid state to assess the singlet excited-state lifetime, which is of interest for photovoltaic conversion. Neat thin films of **Ph-1**, **Napht-1**, and **Pyr-1** of 30 nm on quartz were prepared by evaporation process under high vacuum ($\sim 10^{-6}$ mbar), while films of molecules dispersed in PMMA were deposited on glass by solution process. PMMA matrix provides an environment that restrains molecular conformational (as in the neat films) but keeps the molecules separated (as in solutions). Thus, PMMA matrix is used as benchmark to interrelate solution and neat film environments. Interestingly, whereas PL was not detected in solution as previously mentioned, photoexcitation into the lowest energy absorption band of **Ph-1**, **Napht-1** and **Pyr-1** either dispersed in PMMA matrices or as evaporated neat thin-films, led to photo-emission. Figure 2.15 shows the absorption spectra of molecules in chloroform ($\sim 10^{-5}$ M), in PMMA

matrices, in neat thin films and their respective steady state PL spectra. The PL spectra were obtained by time integrating the PL maps (Figure 2.16) over (0–0.8) ns range for the neat films and (0–1.8) ns for the PMMA matrices.

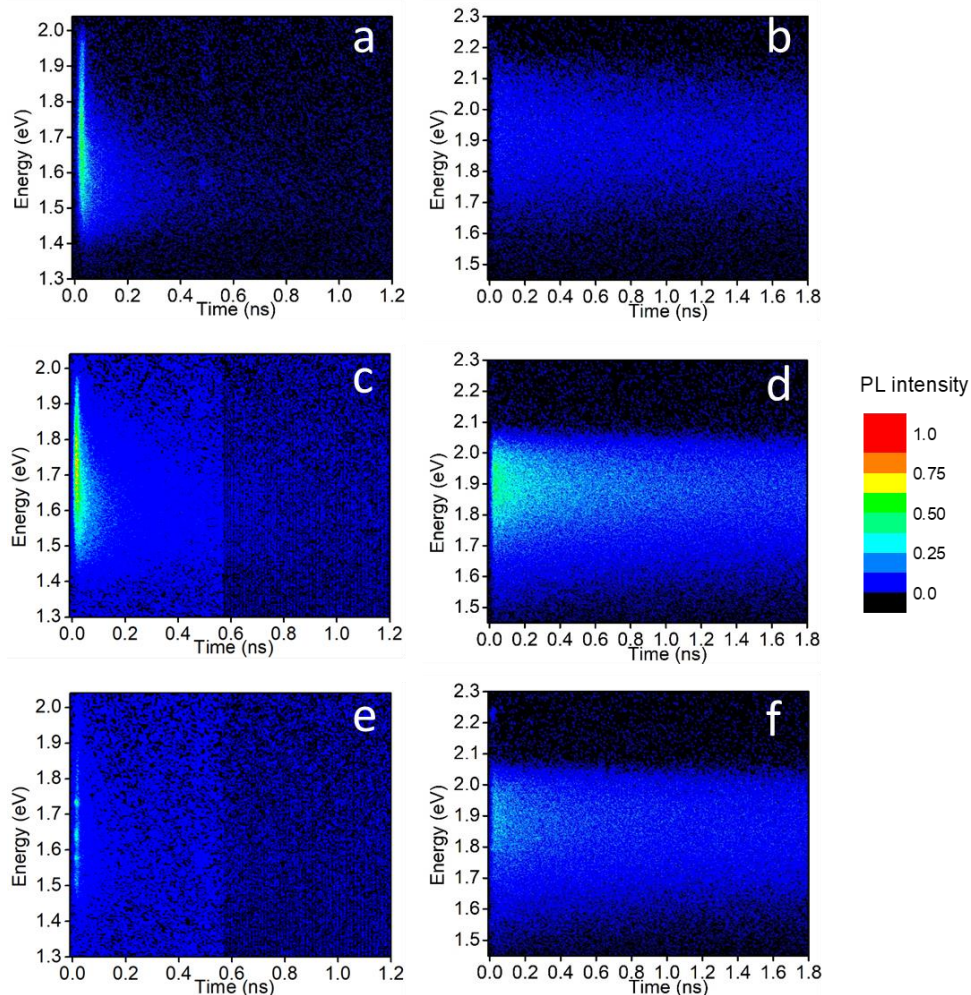


Figure 2.16. PL maps. **Ph-1** (a) neat film, (b) matrix. **Napht-1** (c) neat film, (d) matrix. **Pyr-1** (e) neat film, (f) matrix. The excitation wavelength was set at $\sim 580 \pm 10$ nm.

Compared to the diluted solutions in chloroform for which the target molecules can be considered as isolated, the neat films exhibit a red-shift of the absorption spectra

due to intermolecular interactions. Molecules dispersed in the PMMA matrices exhibit blue-shifted absorption and PL spectra compared to those of the neat films suggesting the absence of intermolecular interactions⁵⁸. The absorption spectra of molecules dispersed in PMMA are even more blue-shifted relative to chloroform solutions probably due to a difference of medium polarity hence affecting the position of the intramolecular charge transfer band.

The appearance of PL in the PMMA matrix with emission maxima between 650–660 nm for **Ph-1**, **Napht-1** and **Pyr-1** may be explained by a motion restriction of the molecules within the PMMA upon photoexcitation. This is also the case for neat thin-films; however due to π – π intermolecular interactions, the PL spectra are significantly shifted to lower energies, giving rise to emission with maxima at 760–780 nm.

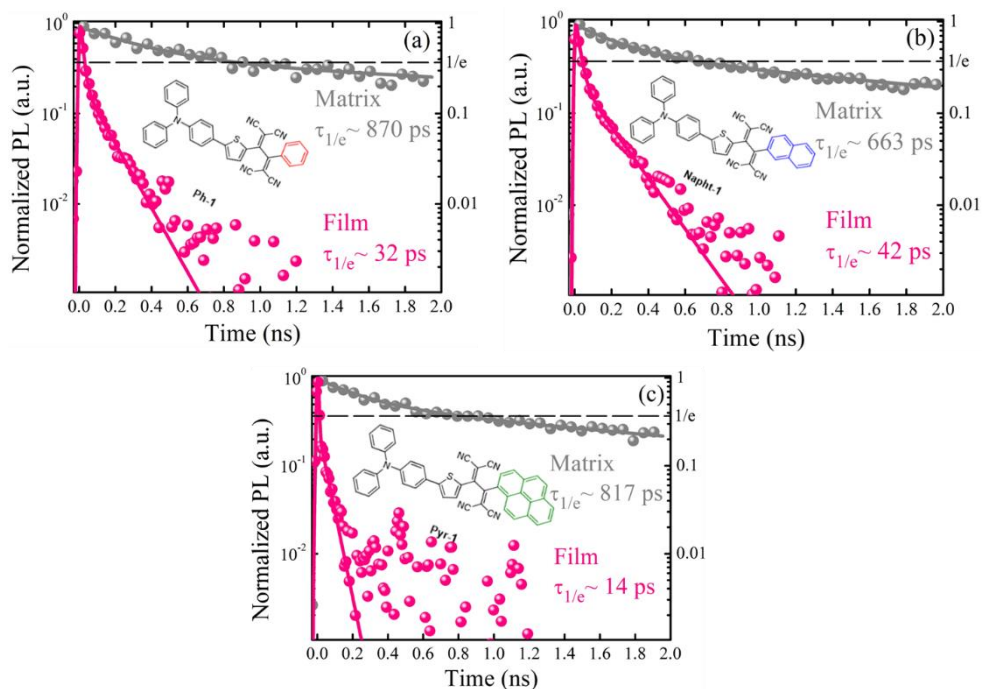


Figure 2.17. Normalized PL transients of (a) **Ph-1**, (b) **Napht-1** and (c) **Pyr-1**. The PL transients of matrices are in gray spheres and neat films are in pink spheres, their respective exponential fitting is in solid lines. The dash black lines represent the PL fitting value at $1/e$ and the corresponding times are written next to the transients.

Figure 2.17 shows the PL transients of the three molecules in PMMA matrices and in neat films. The neat films PL transients exhibit a bi-exponential behavior, which indicates that several photophysical processes contribute to the excited state dynamics. The early times dynamics (<0.1 ns) can be ascribed to intermolecular energy transfer, with possible contributions of non-radiative decay induced by excitonic traps or generation of charge transfer excitons⁶⁰ (see chapter 4 and 5 for details). The singlet exciton lifetimes at $1/e$ level in the neat films amount to ~ 30 ps, 40 ps and 10 ps for **Ph-1**, **Napht-1** and **Pyr-1**, respectively. The lifetimes significantly increase in the PMMA matrices, reaching ~ 870 ps, 660 ps and 810 ps for **Ph-1**, **Napht-1** and **Pyr-1**, respectively. Thus, the increased excited lifetime in the neat films and in PMMA matrix, also demonstrate that restriction of molecules in the solid state causes the recovery of the PL. To gain more insight into the excited state dynamics in TPA/TCBD-derivatives, our colleagues at the University of Mons performed TDDFT calculations.

The computational studies³⁷ indicated that fast relaxation of singlet excited state in solutions is associated with significant conformational changes at the excited state that lead to high values of reorganization energies (0.98 eV) hindering photo-emission. Conversely, by constraining the relaxed excited state optimization (i.e., by freezing all the soft torsion angles of the molecules to mimic the solid state), the reorganization energies were found to be considerably lower (0.47eV) than in solutions, which may explain the PL recovery in the solid state.

To summarize, the combination of time-resolved PL and pump-probe transient absorption measurements allowed us to gain insights into the effect of variation of intramolecular acceptor units from DCV (in TPA-T-DCV-Ph-F) to TCBD-based acceptors. The transient absorption measurements revealed extremely short-lived excited state with lifetime of ~ 10 ps in solution. With time-resolved PL, we measured much longer excited state lifetimes reaching 870 ps in PMMA matrices. All these findings reveal that, the confinement of the molecules in the solid state significantly limits the non-radiative losses. In contrast, the conformational changes in solution, open up an effective non-radiative decay channel that can be related to an energetically accessible conical intersection, as demonstrated in this Chapter with the TPA/DCV based molecule (TPA-T-DCV-Ph-F), and in other previous works⁵⁸.

Methods

Sample Preparation

Steady state absorption spectra of **Ph-1**, **Napht-1** and **Pyr-1** in chloroform were recorded using a concentration of *ca.* 10^{-5} M. For transient absorption measurements in chloroform, measurements were performed using a concentration of *ca.* 2×10^{-4} M and a 1 mm quartz cuvette leading to optical densities of ~ 0.25 at an absorption maximum of ~ 580 nm. For time-resolved PL measurements of well-separated molecules in a matrix, PMMA (Sigma Aldrich, $M_w = 120000$ g/mol) was dissolved in chloroform at a concentration of 150 g/L and stirred at room temperature for 8 hours. Solutions of **Ph-1**, **Napht-1**, and **Pyr-1** (2×10^{-4} M) were separately mixed with PMMA solution to achieve **Ph-1**, **Napht-1** and **Pyr-1**/PMMA volume ratio of 0.4 and stirred for 1 hour. The films were prepared by spin coating the solutions on a plain glass substrate.

Pump-probe transient absorption measurements

To perform the pump-probe transient absorption measurements, a Ti:sapphire regenerative amplifier (Legend Elite Duo, Coherent, 1kHz) was used to seed the two home-built non-collinear optical parametric amplifiers (NOPAs). One of the NOPAs served to generate the pump pulses with central wavelength of 590 nm and FWHM of 27 nm. This output passed through an acoustic-optic programmable dispersive filter (DAZZLER, Fastlite, France) that was used to modulate the amplitude of the pump pulses at 500 Hz and compress the pulses down to 20 fs. The probe beam was obtained from the output of the second NOPA. The probe beam was then directed to a beam-splitter, from which the weak reflected beam was used to pass through the sample while the strong transmitted part was used as a reference beam for pulse-to-pulse intensity normalization by a NMOS linear image sensor (Hamamatsu S3921-128Q, spectral resolution of 14 cm^{-1}), and after the sample, both beams were spectrally dispersed via a spectrograph (Jobin Yvon HR320). Pump and probe beams were focused and spatially overlapped in the quartz cuvette in which the solution was continuously stirred (using a small piece of wire dipped in the solution and a home-built magnetic stirrer).

Author Contributions

B.A.L.R. performed time-resolved PL and transient absorption measurements, Monte-Carlo simulations and interpreted the data under the supervision of M.S.P.; Y.N.L. synthesized and characterized the TPA-T-DCV-Ph-F molecule; W.Y. fabricated the solution-processed solar cells under the supervision of J.M; N.M.S. performed quantum yield measurements under the supervision of S.A.P.; O.D. fabricated the vacuum-processed solar cells; T.L.C.J. performed and interpreted the DFT calculations; P.M and J.A synthesized the TPA/TCBD based molecules under the supervision of C.C and P.B.

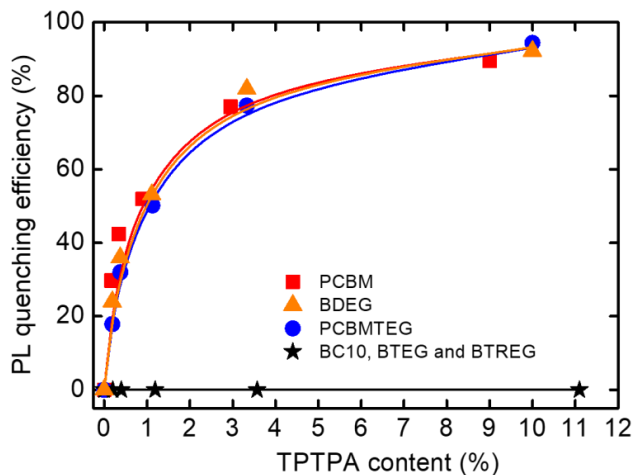
2.6 References

1. Dalton, L. R., Sullivan, P. A. & Bale, D. H. Electric field poled organic electro-optic materials: State of the art and future prospects. *Chem. Rev.* **110**, 25–55 (2010).
2. Raimundo, J. M. *et al.* Design and synthesis of push-pull chromophores for second-order nonlinear optics derived from rigidified thiophene-based π -conjugating spacers. *J. Org. Chem.* **67**, 205–218 (2002).
3. Chen, C. T. Evolution of red organic light-emitting diodes: Materials and devices. *Chem. Mater.* **16**, 4389–4400 (2004).
4. Genin, E. *et al.* ‘Hyper-Bright’ Near-Infrared Emitting Fluorescent Organic Nanoparticles for Single Particle Tracking. *Adv. Mater.* **26**, 2258–2261 (2014).
5. Hardin, B. E., Snaith, H. J. & McGehee, M. D. The renaissance of dye-sensitized solar cells. *Nat. Photonics* **6**, 162–169 (2012).
6. Kim, T. & Lee, K. D- π -A Conjugated Molecules for Optoelectronic Applications. 943–958
7. Roquet, S. *et al.* Triphenylamine-thienylenevinylene hybrid systems with internal charge transfer as donor materials for heterojunction solar cells. *J. Am. Chem. Soc.* **128**, 3459–3466 (2006).
8. Cravino, A., Leriche, P., Alévêque, O., Roquet, S. & Roncali, J. Light-emitting organic solar cells based on a 3D conjugated system with internal charge transfer. *Adv. Mater.* **18**, 3033–3037 (2006).
9. Paek, S. *et al.* Dopant-free hole-transporting materials for stable and efficient perovskite solar cells. *Adv. Mater.* **29**, 1–7 (2017).
10. Ripaud, E., Rousseau, T., Leriche, P. & Roncali, J. Unsymmetrical triphenylamine-oligothiophene hybrid conjugated systems as donor materials for high-voltage solution-processed organic solar cells. *Adv. Energy Mater.* **1**, 540–545 (2011).
11. Cabanetos, C., Blanchard, P. & Roncali, J. Arylamine Based Photoactive Push-Pull Molecular Systems: A Brief Overview of the Chemistry “Made in Angers”. *Chem. Rec.* **19**, 1123–1130 (2019).
12. Sissa, C. *et al.* The effectiveness of essential-state models in the description of optical properties of branched push-pull chromophores. *Phys. Chem. Chem. Phys.* **12**, 11715–11727 (2010).

13. Leliège, A., Régent, C. H. Le, Allain, M., Blanchard, P. & Roncali, J. Structural modulation of internal charge transfer in small molecular donors for organic solar cells. *Chem. Commun.* **48**, 8907–8909 (2012).
14. Zhang, J. *et al.* Solution-processable star-shaped molecules with triphenylamine core and dicyanovinyl endgroups for organic solar cells. *Chem. Mater.* **23**, 817–822 (2011).
15. Kozlov, O. V. *et al.* Simple donor-acceptor molecule with long exciton diffusion length for organic photovoltaics. *Org. Electron.* **53**, 185–190 (2018).
16. Kozlov, O. V. *et al.* Triphenylamine-Based Push-Pull Molecule for Photovoltaic Applications: From Synthesis to Ultrafast Device Photophysics. *J. Phys. Chem. C* **121**, 6424–6435 (2017).
17. Kozlov, O. V. *et al.* Ultrafast charge generation pathways in photovoltaic blends based on novel star-shaped conjugated molecules. *Adv. Energy Mater.* **5**, (2015).
18. Li, Y., Ren, T. & Dong, W. J. Tuning photophysical properties of triphenylamine and aromatic cyano conjugate-based wavelength-shifting compounds by manipulating intramolecular charge transfer strength. *J. Photochem. Photobiol. A Chem.* **251**, 1–9 (2013).
19. Londi, G. *et al.* Comprehensive modelling study of singlet exciton diffusion in donor-acceptor dyads: When small changes in chemical structure matter. *Phys. Chem. Chem. Phys.* **21**, 25023–25034 (2019).
20. Zheng, Z. H. *et al.* A biocompatible colorimetric triphenylamine-dicyanovinyl conjugated fluorescent probe for selective and sensitive detection of cyanide ion in aqueous media and living cells. *Sensors (Switzerland)* **17**, (2017).
21. Salamatova, E. *et al.* Visualization of molecular excitons diffusion. *Phys. Chem. Interfaces Nanomater.* XV **9923**, 99230K (2016).
22. Brédas, J. L., Norton, J. E., Cornil, J. & Coropceanu, V. Molecular understanding of organic solar cells: The challenges. *Acc. Chem. Res.* **42**, 1691–1699 (2009).
23. Köhler, A. *Related Titles Physics of Organic Self-Organized Organic OLED displays fundamentals The Photophysics behind Photovoltaics and Photonics.*
24. Bauer, G. *Lecture Notes in Physics 901 Photovoltaic Solar Energy Conversion.* (2015). doi:10.1007/978-3-662-46684-1
25. Babics, M. *et al.* Negligible Energy Loss during Charge Generation in Small-Molecule/Fullerene Bulk-Heterojunction Solar Cells Leads to Open-Circuit Voltage over 1.10 v. *ACS Appl. Energy Mater.* **2**, 2717–2722 (2019).
26. Fei, Z. *et al.* Influence of backbone fluorination in regioregular poly(3-alkyl-4-fluoro)thiophenes. *J. Am. Chem. Soc.* **137**, 6866–6879 (2015).
27. Nielsen, C. B., White, A. J. P. & McCulloch, I. Effect of Fluorination of 2,1,3-Benzothiadiazole. *J. Org. Chem.* **80**, 5045–5048 (2015).
28. Li, Z. *et al.* Dramatic performance enhancement for large bandgap thick-film polymer solar cells introduced by a difluorinated donor unit. *Nano Energy* **15**, 607–615 (2015).
29. Balakirev, D. O. *et al.* p-Fluorophenyldicyanovinyl as electron-withdrawing group for highly soluble and thermally stable donor–acceptor small molecules. *J. Photonics Energy* **8**, 1 (2018).
30. Raul, B. A. L. *et al.* Excited state dynamics and exciton diffusion in triphenylamine/dicyanovinyl push–pull small molecule for organic optoelectronics. *Sci. Rep.* **10**, 1–10 (2020).

31. Ripaud, E., Olivier, Y., Leriche, P., Cornil, J. & Roncali, J. Polarizability and internal charge transfer in thiophene-triphenylamine hybrid π -conjugated systems. *J. Phys. Chem. B* **115**, 9379–9386 (2011).
32. Yeh, S. C. A., Patterson, M. S., Hayward, J. E. & Fang, Q. Time-resolved fluorescence in photodynamic therapy. *Photonics* **1**, 530–564 (2014).
33. Lakowicz, J. R. *Principles of fluorescence spectroscopy. Principles of Fluorescence Spectroscopy* (2006). doi:10.1007/978-0-387-46312-4
34. Nelson Jr., R. D. Electric Dipole the Gas Phase. *Natl. Stand. Ref. Data Ser.* (1970).
35. Nad, S. & Pal, H. Unusual Photophysical Properties of Coumarin-151. *J. Phys. Chem. A* **105**, 1097–1106 (2001).
36. Shi, J. *et al.* Solid State Luminescence Enhancement in π -Conjugated Materials: Unraveling the Mechanism beyond the Framework of AIE/AIEE. *J. Phys. Chem. C* **121**, 23166–23183 (2017).
37. Marqués, P. S. *et al.* Triphenylamine/Tetracyanobutadiene-based π -Conjugated Push-Pull Molecules End-capped with Arene Platforms: Synthesis, Photophysics, and Photovoltaic Response. *Chem. – A Eur. J.* (2020). doi:10.1002/chem.202002810
38. Theisen, R. F., Huang, L., Fleetham, T., Adams, J. B. & Li, J. Ground and excited states of zinc phthalocyanine, zinc tetrabenzoporphyrin, and azaporphyrin analogs using DFT and TDDFT with Franck-Condon analysis. *J. Chem. Phys.* **142**, (2015).
39. Küppel, H. ULTRAFast NON-RADIATIVE DECAY POTENTIAL-ENERGY VIA CONICAL INTERSECTIONS The processes of non-radiative electronic relaxation in a bound level structure (internal conversion and intersystem crossing) have received much attention in the past , both b. **77**, 359–375 (1983).
40. Kovac, J. D. Physical Chemistry: A Molecular Approach (McQuarrie, Donald A.; Simon, John D.). *J. Chem. Educ.* **75**, 545 (1998).
41. Hildner, R., Lemmer, U., Scherf, U. & Köhler, J. Picosecond excitation energy relaxation processes in a ladder-type π -conjugated polymer. *Chem. Phys. Lett.* **429**, 103–108 (2006).
42. Mikhnenko, O. V. *et al.* Trap-limited exciton diffusion in organic semiconductors. *Adv. Mater.* **26**, 1912–1917 (2014).
43. Lin, J. D. A., Mikhnenko, O. V., Van Der Poll, T. S., Bazan, G. C. & Nguyen, T. Q. Temperature dependence of exciton diffusion in a small-molecule organic semiconductor processed with and without additive. *Adv. Mater.* **27**, 2528–2532 (2015).
44. Rörich, I., Mikhnenko, O. V., Gehrig, D., Blom, P. W. M. & Crăciun, N. I. Influence of Energetic Disorder on Exciton Lifetime and Photoluminescence Efficiency in Conjugated Polymers. *J. Phys. Chem. B* **121**, 1405–1412 (2017).
45. Bäessler, H. Charge Transport in Disordered Organic Photoconductors a Monte Carlo Simulation Study. *Phys. Status Solidi* **175**, 15–56 (1993).
46. Mikhnenko, O. V., Blom, P. W. M. & Nguyen, T. Q. Exciton diffusion in organic semiconductors. *Energy Environ. Sci.* **8**, 1867–1888 (2015).
47. Lin, J. D. A. *et al.* Systematic study of exciton diffusion length in organic semiconductors by six experimental methods. *Mater. Horizons* **1**, 280–285 (2014).
48. Mikhnenko, O. V. *et al.* Exciton diffusion length in narrow bandgap polymers. *Energy Environ. Sci.* **5**, 6960–6965 (2012).
49. Athanasopoulos, S., Hennebicq, E., Beljonne, D. & Walker, A. B. Trap limited exciton transport in conjugated polymers. *J. Phys. Chem. C* **112**, 11532–11538 (2008).

50. Athanopoulos, S., Emelianova, E. V., Walker, A. B. & Beljonne, D. Exciton diffusion in energetically disordered organic materials. *Phys. Rev. B - Condens. Matter Mater. Phys.* **80**, 1–7 (2009).
51. Kozlov, O. V. *et al.* Real-Time Tracking of Singlet Exciton Diffusion in Organic Semiconductors. *Phys. Rev. Lett.* **116**, 1–5 (2016).
52. Royackers, J. *et al.* Doubly Encapsulated Perylene Diimides: Effect of Molecular Encapsulation on Photophysical Properties. *J. Org. Chem.* **85**, 207–214 (2020).
53. Leventis, A. *et al.* Highly Luminescent Encapsulated Narrow Bandgap Polymers Based on Diketopyrrolopyrrole. *J. Am. Chem. Soc.* **140**, 1622–1626 (2018).
54. Wang, W., Sun, R., Guo, J., Guo, J. & Min, J. An Oligothiophene–Fullerene Molecule with a Balanced Donor–Acceptor Backbone for High-Performance Single-Component Organic Solar Cells. *Angew. Chemie - Int. Ed.* **58**, 14556–14561 (2019).
55. Wei, G. *et al.* Efficient, ordered bulk heterojunction nanocrystalline solar cells by annealing of ultrathin squaraine thin films. *Nano Lett.* **10**, 3555–3559 (2010).
56. Zhang, Y. *et al.* Large Crystalline Domains and an Enhanced Exciton Diffusion Length Enable Efficient Organic Solar Cells. *Chem. Mater.* **31**, 6548–6557 (2019).
57. Berlman, I. B. Introduction. *Handb. Fluoresc. Spectra Aromat. Mol.* 1–38 (1971). doi:10.1016/b978-0-12-092656-5.50006-x
58. Monti, F. *et al.* Anilino-Substituted Multicyanobuta-1,3-diene Electron Acceptors: TICT Molecules with Accessible Conical Intersections. *J. Phys. Chem. A* **119**, 10677–10683 (2015).
59. Kozlov, O. V. *et al.* Ultrafast Exciton-to-Polaron Conversion in Densely Packed Small Organic Semiconducting Molecules. *Adv. Opt. Mater.* **5**, 1–7 (2017).
60. Luponosov, Y. N. *et al.* Effect of oligothiophene π -bridge length in D- π -A star-shaped small molecules on properties and photovoltaic performance in single-component and bulk heterojunction organic solar cells and photodetectors. *Mater. Today Energy* **22**, 100863 (2021).



Chapter 3. Exciton Dynamics in Solution-Processed Films of Novel Fullerene Derivatives

Since their inception, fullerenes have been used extensively in the organic semiconductors industry for diversified applications. In this chapter, we investigate the photophysics of PCBM and five novel fullerene derivatives, namely PCBMTEG, BDEG, BC10, BTEG and BTREG. All fullerenes demonstrate similar photophysical properties in the neat films. However, large differences in the crystallinity of the fullerenes influences the exciton dynamics in blends with exciton quenchers; where excitons dissociate into charge carriers in PCBM, PCBMTEG, and BDEG blends, but do not dissociate in BC10, BTEG, and BTREG blends. Through AFM imaging, we rationalize that crystallization of fullerenes precludes fine-intermixing in the blends, thus preventing excitons from reaching the quencher at the course of its random walk. These results highlight the importance of a thorough morphological investigation in the manufacture of organic semiconductor devices.

This chapter is based on the following publication:

Sylvia Rousseva, [Benedito A. L. Raul](#), Felien S. van Kooij, Alexey V. Kuevda, Srikanth Birudula, Jan C. Hummelen, Maxim S. Pshenichnikov, and Ryan C. Chiechi, *Phys. Chem. Chem. Phys.* **24**, 13763-13772 (2022)

3.1 Introduction

The photon absorption in organic semiconductors leads to strongly bound electron-hole pairs called Frenkel excitons¹. In the manufacturing of organic solar cells (OSCs), a heterojunction composed of electron-donor (donor) and electron-acceptor (acceptor) materials are typically used to dissociate the excitons into charge carriers². In the bulk-heterojunction (BHJ) configuration, the donor and acceptor materials are blended to obtain nanoscale phase separated domains, ensuring efficient exciton harvesting over the whole extent of the solar cell³. In BHJ OSCs, if the grain sizes of the donor and acceptor domains are very small, the probability of charge carrier recombination increases. On the other hand, if the grain sizes are very large (exceeding the exciton diffusion length), the excitons may recombine before reaching the donor-acceptor interface. Thus, knowledge of exciton dynamics is fundamental for the morphological optimization of the active layer^{4,5}.

Since the inception of the BHJ, fullerenes have been used extensively as the acceptor material in BHJ OSCs. The excited states in fullerenes are weakly emissive, with reported PL quantum yield of ~0.2 - 0.14% in solutions, and values below the instrument detection limits in films⁶. Such low PL quantum yield values are typically attributed to the high yield of formation of triplet excitons through efficient intersystem crossing of singlet excitons that are induced by the large spin-orbit coupling in the fullerenes⁶⁻¹¹. Additionally, charge transfer transitions⁶ in crystalline fullerenes have been demonstrated to contribute to charge carriers generation^{12,13}, which further contributes to low PL quantum yield values of fullerenes and possibly the short exciton diffusion lengths values^{4,5,14}. The aforementioned photophysical properties of fullerenes are among the most common reasons why there are few investigations reporting time-resolved PL properties of this class of materials^{4,6,9,14}.

In this Chapter, we investigate the photophysical properties of PCBM and five novel C₇₀ derivatives (Figure 3.1), with a particular focus on the role of fullerene derivatives as light absorber. The materials can be separated into two groups: (1) PCBM and BC10-2 with non-polar side chains, and (2) PCBMTEG, BDEG, BTEG and BTREG all containing various lengths of polar ethylene glycol side chains. All fullerenes demonstrate similar photophysical properties in the neat films. With time-resolved PL volume quenching technique, we found that crystallization plays a crucial role on exciton dissociation in the blend films containing fullerenes and exciton quenchers. We observe an effective exciton dissociation in blends films containing PCBM, BDEG or PCBMTEG; however, in blends films of BC10, BTEG or BTREG, no exciton dissociation was observed. With the help of AFM imaging,

we attribute the later to the crystallization of fullerenes which drives their self-assembly rather than allowing for fine-intermixing between the quenchers and fullerene derivatives in the blends. Since the fullerene derivatives domains within the films are much larger than the exciton diffusion lengths of ~ 10 nm, the excitons recombine before reaching the fullerene/quencher interface. These results further reiterate that crystallization dynamics should meticulously be taken into account during the manufacture of BHJ OSCs.

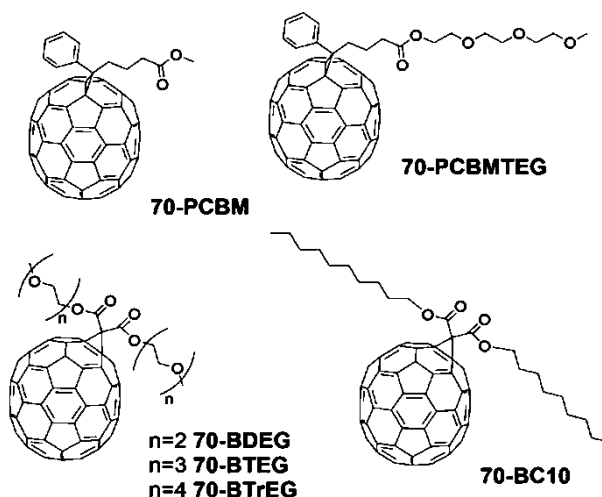


Figure 3.1. Chemical structures of the fullerene derivatives.

3.2 Results and Discussion

3.2.1 Absorption and Photoluminescence

Figure 3.2 shows the absorption spectra of the neat films of fullerene derivatives and the exciton quencher (4-(5-phenylthiophen-2-yl)phenyl)amine (TPTPA). The TPTPA neat films exhibit strong absorption at 400 nm while the absorption of the fullerenes elongates to 700 nm. This allowed us to use an excitation wavelength of 550 nm for a selective generation of excitons in fullerenes derivatives. The PL spectra of the fullerene derivatives in solutions, matrices and neat films obtained upon temporal integration of the PL maps (Figure 3.3) over all the time delays are shown in Section 3.5.1. The dispersion of the molecules in PMMA matrix prevents

intermolecular interactions in the solid state, therefore acting as benchmark between diluted solutions and neat films¹⁵⁻¹⁷. For all the molecules, the PL spectra in solutions and matrices peak at ~ 690 nm (~ 1.8 eV); whereas in the neat films the PL spectra are slightly red shifted to ~ 700 nm (~ 1.77 eV) due to intermolecular interactions.

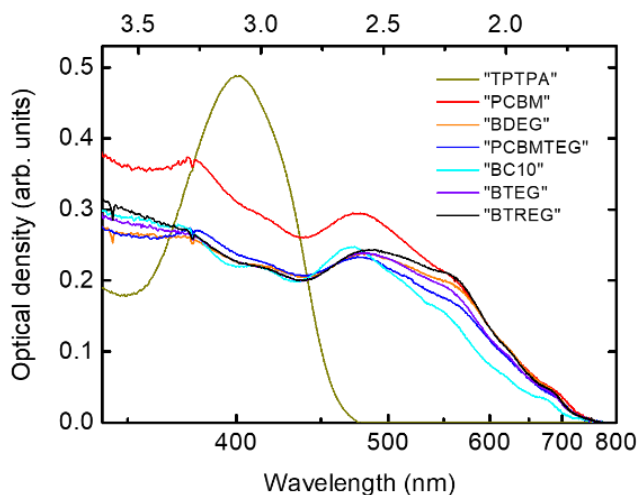


Figure 3.2. Absorption spectra of TPTPA (yellow), PCBM (red), BDEG (orange), PCBMTEG (blue), BC10 (cyan), BTEG (violet) and BTREG (black) neat films.

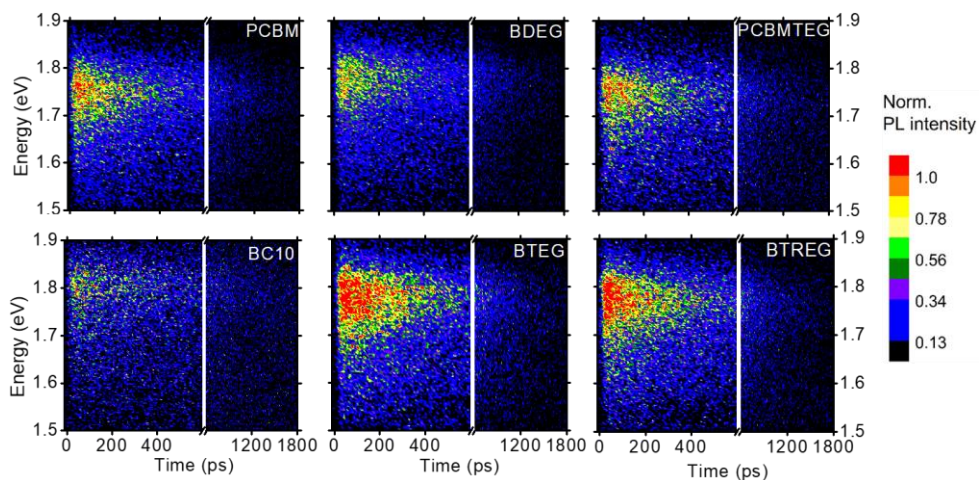


Figure 3.3. Normalized PL maps of fullerene derivatives neat films following excitation at 550 nm.

3.2.2 Exciton Dissociation

The excited-state dynamics of fullerene derivatives were measured in solution, in the PMMA matrix, and in neat films. The excited-state lifetimes were obtained by integrating the PL maps across the measured spectral range (1.4 - 2 eV) and fitting the resulting PL transients with a mono-exponential decay function convoluted with a Gaussian apparatus function. The PL of all six derivatives exhibited mono-exponential decay (Section 3.5.1), with excited state lifetime values ~ 800 ps in solution/PMMA matrices and ~ 550 ps for the neat films (Figure 3.4). It has been demonstrated that in conjugated polymers, excitation migration is faster in films compared to solutions due to the efficient interchain hopping favored by closely packed chains^{18,19}. Consequently, excitons in the neat film diffuse fast towards non-radiative decay channels, which increases the probability of exciton quenching^{20,21}. Using the same analogy, the short-excited state lifetime in fullerene neat films as compared to solutions and matrices can be explained by diffusion limited quenching at non-radiative decay channels.

The neat films of PCBM molecules have been demonstrated to exhibit intermolecular charge transfer (CT) transitions that allows for significant polaron pairs generation¹². Hence, we can reasonably associate the non-radiative decay channels in the fullerene derivatives to intermolecular charge transfer transitions that facilitate charge carrier generation. The concentration (c) of intermolecular CT transitions in the neat films can be estimated using the Stern-Volmer equation²¹:

$$c = \left(\frac{1}{\tau_f} - \frac{1}{\tau_m} \right) \frac{1}{4\pi r D} \quad (3.1)$$

where τ_f is the excited state lifetime in the neat films (550 ps), τ_m is the excited state lifetime in solution or matrix (800 ps), r is the sum of PCBM and exciton radii which is typically set at 1 nm, D is the exciton diffusion coefficient ($5 \times 10^{-4} \text{ cm}^2 \text{ s}^{-1}$) (obtained from Monte Carlo simulations, which will be discussed later). Inserting these parameters in equation (3.1), the concentration of intermolecular CT transitions in neat films is estimated to be $c = 9 \times 10^{17} \text{ cm}^{-3}$, which is in the $10^{17} - 10^{18} \text{ cm}^{-3}$ concentration range reported for non-radiative decay channels for many organic semiconductors²¹.

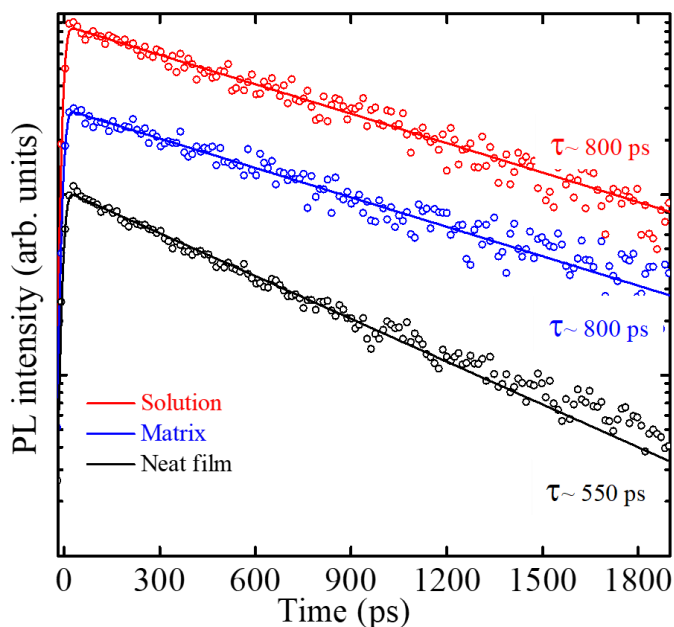


Figure 3.4. Representative logarithmic experimental PL decay transients plots of all the fullerene derivatives in solutions (red), matrices (blue) and neat films (black), and the respective fitting (solid lines) convoluted with a Gaussian apparatus function of ~ 10 ps. Each PL decay transient is re-scaled by a factor of 3 with respect to the previous. See Section 3.5.1 for PL decay transients of all the fullerene derivatives.

We now turn our attention to the exciton diffusion length (L_D), which is another important parameter for organic photovoltaics. We used the PL volume quenching technique combined with Monte Carlo simulations to determine the value of exciton diffusion length. In the PL volume quenching experiments, the material of interest is mixed with a small amount of another material that behaves as an exciton quencher. When the PL is measured, an acceleration in the PL decay is observed due to exciton quenching. This method alleviates the difficulties involved in controlling the thickness of the films and intercalation at the interface, which is necessary in the case of surface/bilayer quenching techniques²². In the PL volume quenching technique, the quencher is assumed to be miscible and randomly distributed throughout the material of interest. The selected quencher molecules should have suitable energy level alignment such that electron (or hole) transfer from the donor (or acceptor) to the quencher molecule is possible. Furthermore, the selected quencher should not

absorb at the excitation wavelength so that excitons can selectively be generated in the host material (in this case the fullerene).

In this study, we selected TPTPA as the quencher material, as it has been previously used to investigate the exciton diffusion in organic semiconductor films^{23,24}. Blended films with molar ratios of quencher: fullerene varying from 0.165 % to 11 % were fabricated and the time-resolved PL was measured. An excitation wavelength of 550 nm was used where TPTPA does not absorb (Figure 3.2).

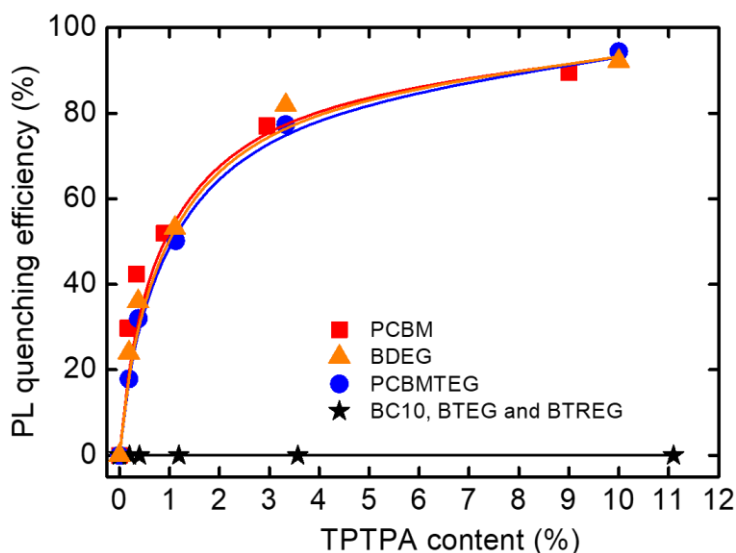


Figure 3.5. Experimental (symbols) PL quenching efficiencies versus TPTPA content for PCBM (red), BDEG (orange), PCBMTEG (blue) and BC10/BTEG/BTREG (black). Solid lines represent the Monte Carlo modeled results.

The PL quenching experiments results separated the fullerene derivatives into two categories. For PCBM, PCBMTEG, and BDEG, the PL decay demonstrated the expected trend: as the quencher concentration was increased, the PL decayed faster due to quenching of the exciton by hole transfer at the fullerene/TPTPA interfaces²⁴.

The PL quenching efficiency (Q) is quantified as $Q = 1 - \frac{\int PL_{blend} dt}{\int PL_{neat} dt}$, where PL_{blend} is the normalized PL decay transient for samples with different TPTPA content, PL_{neat} is normalized PL decay transient of the neat films. The PL quenching efficiency increases to nearly 100% with increase in quencher concentration for the mixed blends of PCBM, BDEG and PCBMTEG (Figure 3.5). In contrast, for BC10, BTEG and BTREG no change in the rate of PL decay was observed relative to the neat films implying a lack of PL quenching.

The exciton diffusion lengths for PCBM, PCBMTEG and BDEG was determined by using Monte Carlo simulations to model the PL dynamics²⁵ (details in Section 3.5.3). Exciton dynamics in disordered organic systems are inherently characterized by a two-step process. Initially, the exciton undergoes spectral diffusion towards lower energy sites until a quasi-equilibrium is reached at $\frac{\sigma^2}{kT}$ below the center of the Gaussian density of states (DOS), after which exciton diffusion proceeds via a thermally activated hopping mechanism²². The energetic disorder, $\sigma \sim 25$ meV was obtained experimentally from the PL mean energy shift (Figure 3.6) and the exciton hopping time was used as the only fitting parameter for the Monte Carlo simulations and determined to be ~ 2 ps. With these values, the experimental results were satisfactorily reproduced and an exciton diffusion length of ~ 10 nm was calculated from the exciton displacement distribution (Figure 3.7a). The diffusion coefficient (D) was initially $D \sim 6.5 \times 10^{-4} \text{ cm}^2\text{s}^{-1}$ but stabilized at $D \sim 5 \times 10^{-4} \text{ cm}^2\text{s}^{-1}$ after the initial fast downhill migration through the DOS in the first 300 ps (Figure 3.7b). The small magnitude of the initial drop is a result of the small energetic disorder which at ~ 25 meV lies on the order of kT . These values are in agreement with previous measurements for PCBM^{4,5,24,26}.

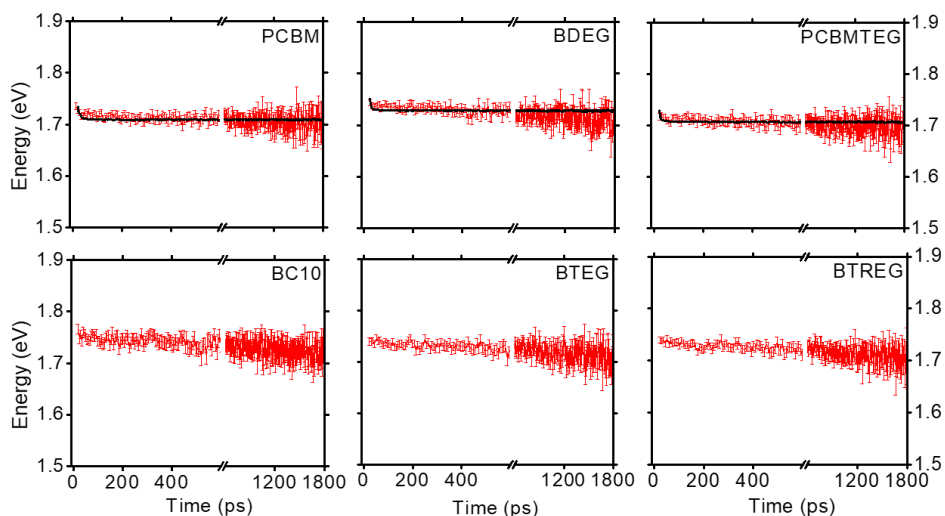


Figure 3.6. Experimental (red lines) and MC modeled (black lines) PL mean energy shift. The MC simulations were not performed for the derivatives where PL quenching was observed in the mixed films.

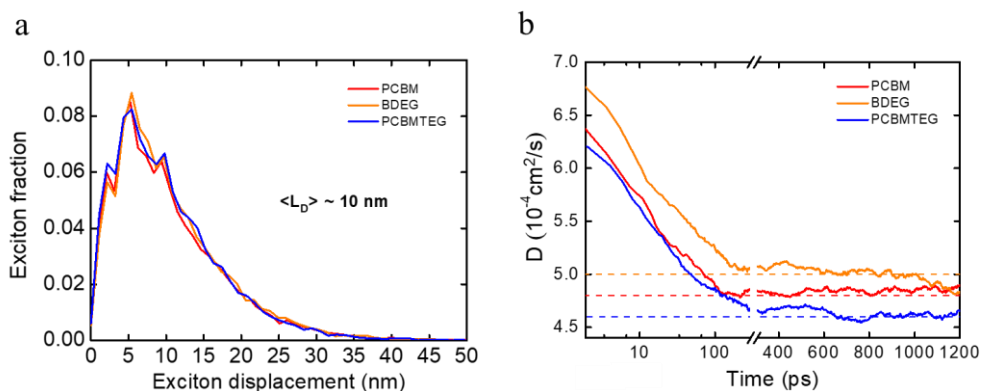


Figure 3.7. Monte Carlo simulated exciton displacement distribution (a) and exciton diffusion coefficients (b), in PCBM (red), BDEG (orange) and PCBMTEG (blue) neat films. The first 300 ps in (b) are in logarithmic scale.

For the other three fullerene derivatives BC10, BTEG and BTREG, additional films were fabricated with quencher/fullerene molar ratios of 14 %, 20 % and 50%; however, even at 50% quencher loading, the PL transients still demonstrated similar decays with the same lifetime as the neat films. The absorption spectra of the blend films confirmed that the quencher TPTPA was in fact present in the films, and no signs of a new band appearing in the spectrum due to ground-state interactions was observed²⁷. We presume that the lack of PL quenching could arise due to phase separation between the quencher and the fullerene derivatives, negating the assumption that the blended films are homogeneous.

To gain more insight about lack of PL quenching in BC10, BTEG and BTREG, our colleague Sylvia Rousseva (Stratingh Institute for Chemistry & Zernike Institute for Advanced Materials, Groningen) used atomic force microscopy (AFM) to measure the surface morphology of the films. From the AFM images our colleague observed that the blends films of TPTPA with PCBM, PCBMTEG and BDEG (Figure 3.8) appear amorphous, while the blends films of BC10, BTEG and BTREG have some structural features when the quencher TPTPA concentration is increased²⁷. Moreover, the AFM images of the neat fullerene films of BTEG and BC10, demonstrate a crystalline phase. All this suggests that the lack of PL quenching observed in the time-resolved PL measurements of the mixed films is caused by the crystallinity of fullerene derivatives which drives self-assembly of the fullerenes rather than allowing for intermixing with the TPTPA molecules. Since the fullerene domains

within the film are much larger than the expected exciton diffusion length, there is a very low probability of an exciton reaching the interface with the quencher at the course of its random walk.

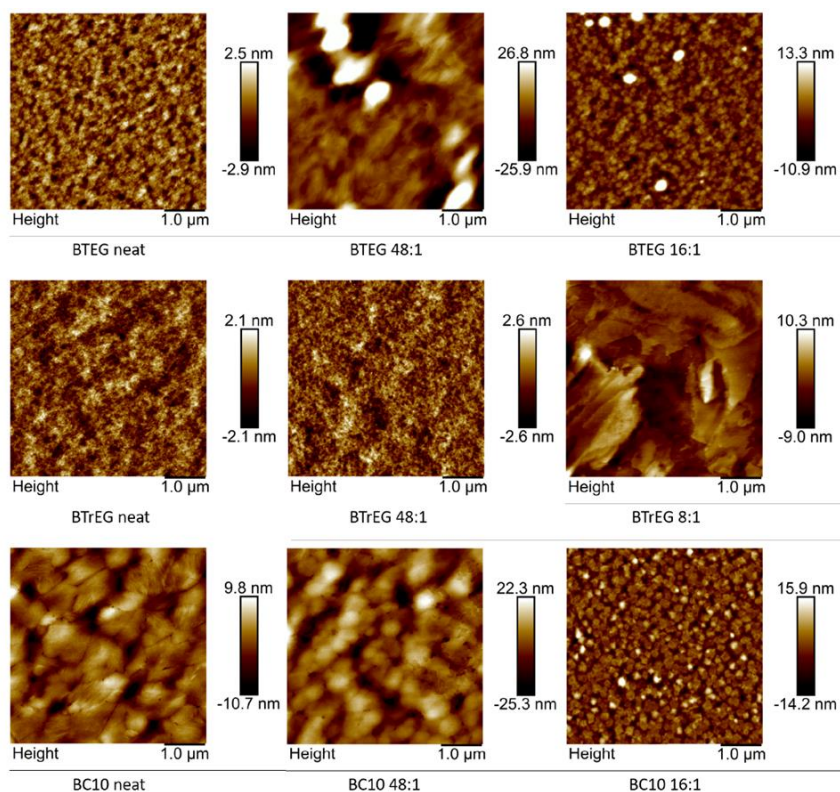


Figure 3.8. AFM images of BTEG, BTREG and BC10 films with an increasing amount (left to right) of TPTPA. The fullerene/TPTPA weight ratios are given. The AFM measurements were performed by Sylvia Rousseva (Stratingh Institute for Chemistry & Zernike Institute for Advanced Materials, Groningen). AFM images were measured using a Bruker Multimode.

In an attempt to minimize phase separation, films using a variety of spin-coating conditions and different solvents for BTEG and BTREG were fabricated, but we still did not obtain different results (Section 3.5.2). Furthermore, to test if a mismatch in the polarities of TPTPA and the fullerenes was an influencing factor, two new quencher molecules, BDTPHTEG²⁷ and OT²⁸ were tested with BTEG and BC10.

BDTPhTEG contains polar EG chains similar to BTEG whereas OT contains alkyl solubilizing chains similar to BC10. Both in the case of matched and mismatched polarities, no PL quenching was observed (Section 3.5.2). The presence of the quencher in the fabricated films was confirmed by measuring the absorption of the films²⁷.

Finally, we estimated an upper limit on exciton diffusion in films of BTEG, BTREG, and BC10 by performing exciton-exciton annihilation experiments²². For this technique, the PL of the material is measured with increasing excitation power such that the exciton density in the neat films substantially increases. At higher excitation powers, when the average distance between excitons become similar to exciton diffusion length, exciton-exciton annihilation (EEA) is more likely to occur and it is observed as the acceleration on the PL decay transients. We measured the PL decay of BTEG, BTREG, and BC10 with a range of excitation power from 10-200 μW , where 200 μW was the maximum power achievable with the experimental set-up. Within this range, no EEA was observed, thus we estimate an upper limit of ~ 30 nm on the exciton diffusion from the exciton density (Section 3.5.4). We repeated these experiments with higher pulse energy at the excitation wavelength of 405 nm which allowed us to lower the no-EEA range down to 15 nm (Section 3.5.4). The further increase of excitation fluence was limited by sample photo-degradation which was more prominent at 405 nm than at 550 nm. Therefore, the EEA experiments place the singlet exciton diffusion length of BC10, BTEG, and BTREG within the same range as PCBM.

3.3 Conclusions

In this Chapter, we investigated the photophysics of novel fullerene derivatives. By combining PL volume quenching technique and MC simulations we extracted exciton diffusion length of ~ 10 nm in solution processed layers of PCBM, PCBMTEG and BDEG, whilst for BC10, BTEG and BTREG it was not possible to accurately measure the exciton diffusion lengths with the PL volume quenching method due to the microcrystalline nature of the films. Nevertheless, we estimated an upper limit on the exciton diffusion length of 15 nm for BC10, BTEG and BTREG which is in the same order of magnitude as PCBM. Since small changes in the length or polarity of side chains can have large effects on the crystallinity and morphology, comparison in terms of BHJ devices performance might provide ambiguous results unless the morphology is thoroughly analyzed. Thus, the findings presented in this

Chapter, highlights the importance to meticulously take into account the crystallization dynamics during the fabrication of BHJ devices.

3.4 Methods

3.4.1 Sample Preparation

The samples were prepared as described in reference [27].

3.4.2 Time-resolved Photoluminescence and Absorption

Time-resolved photoluminescence data were acquired using a streak camera (C5680 from Hamamatsu) equipped with a spectrograph. The excitation wavelength was obtained by focusing the output from the mode-locked Ti: sapphire laser (Mira 900) into the Newport SGC-800 hollow fiber and selecting the portion of the white light with a band pass filter of 550 nm central wavelength and FWHM of 10 nm. The excitation power was 50 μ W. A long pass filter (OG 610) was placed before the spectrograph to filter residual excitation light.

The absorption spectra were measured using a PerkinElmer Lambda 900 UV/VIS/NIR spectrometer.

3.5 Supplementary Information

3.5.1 Photoluminescence Spectra and Transients

The PL spectra of the fullerene derivatives in solutions, matrices and neat films obtained upon temporal integration of the PL maps over all the time delays are shown in Figure 3.9. For all the molecules, the PL spectra in solutions and matrices peak at ~ 690 nm (~ 1.8 eV), whereas in the neat films the PL spectra are slightly red shifted to ~ 700 nm (~ 1.77 eV) compared to the spectra in solutions and matrices. This is attributed to intermolecular interactions between closed packed PCBM molecules in the neat films which causes changes in the energetic landscape, thus allowing for intermolecular non-radiative decay.

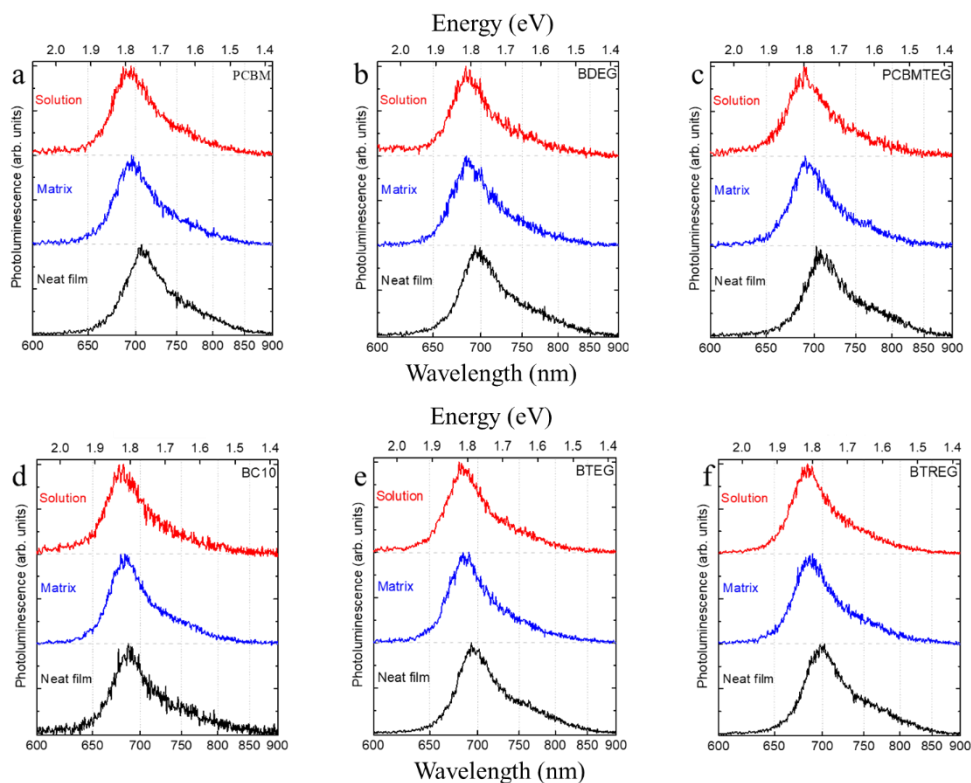


Figure 3.9. Normalized PL spectra of solutions (red), matrices (blue) and neat films (black). Each PL spectrum is offset by the corresponding dashed lines. (a) PCBM, (b) BDEG, (c) PCBMTEG, (d) BC10, (e) BTEG, (f) BTREG.

Figure 3.10 shows the PL decay transients of solutions, matrices and neat films obtained by integrating the PL maps in the 1.4 -2 eV spectral range.

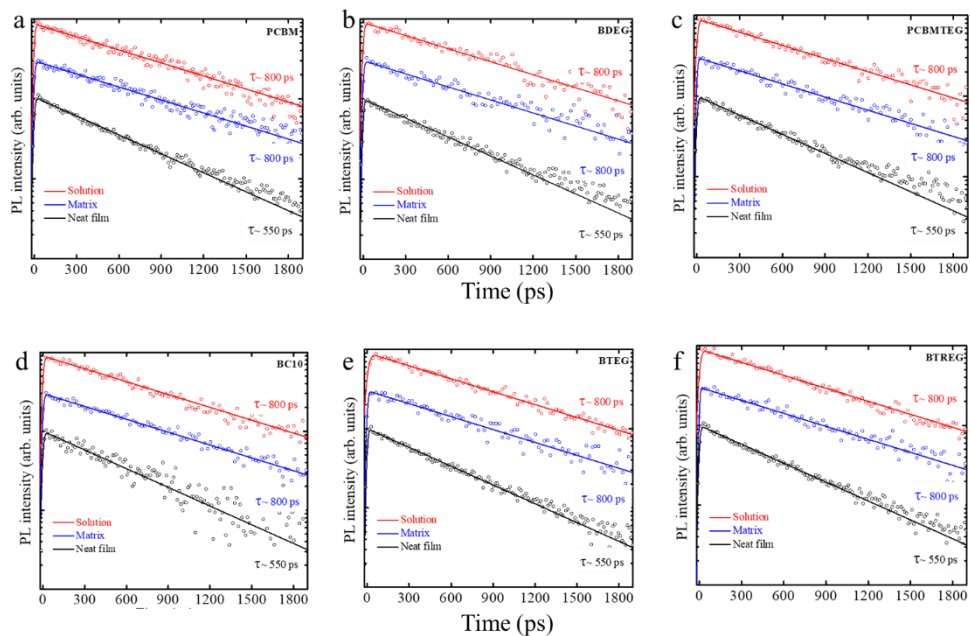


Figure 3.10. Logarithmic plots of the experimental PL decay transients of solutions (red), matrices (blue) and neat films (black) and the respective fitting (solid lines) convoluted with a Gaussian apparatus function of ~ 10 ps. Each PL transient is re-scaled by a factor of 3 with respect to the previous. (a) PCBM, (b) BDEG, (c) PCBMTEG, (d) BC10, (e) BTEG, (f) BTREG.

3.5.2 Photoluminescence Volume Quenching

Figure 3.11 shows the PL decay transients of neat and mixed films. As stated in the main text, concentration increase of the quencher causes acceleration on the PL decay transients for PCBM, BDEG and PCBMTEG. However, for BC10, BTEG and BTREG the PL decay transients do not change with the increase in quencher content.

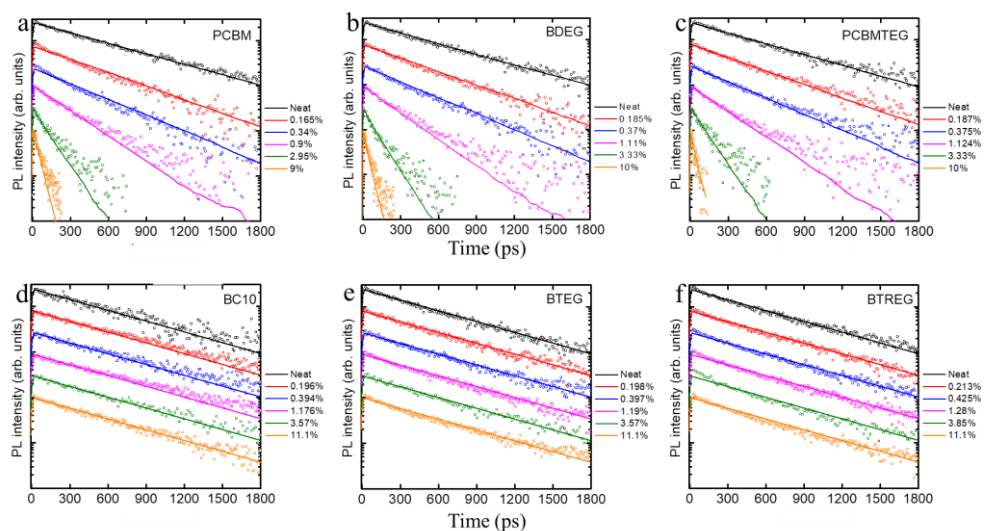


Figure 3.11. Normalized logarithmic PL transients of the neat films (black circles) and mixed films with different quencher/donor molar ratios (colored circles). The solid lines in (a), (b) and (c) corresponds to Monte Carlo modeled PL decay transients, while in (d), (e) and (f) are mono-exponential fitting with a lifetime of 550 ps. For clarity, each PL decay transient is re-scaled by a factor of 3 with respect to the previous. (a) PCBM, (b) BDEG, (c) PCBMTEG, (d) BC10, (e) BTEG, (f) BTREG.

To ensure that the PL dynamics of the blends with quenching (PCBM, BDEG and PCBMTEG) is independent on processing conditions, we prepared neat and mix films using different spinning parameters (Figure 3.12). By applying the same Monte Carlo simulations input parameters as used for Figure 3.11, the simulated results reproduced accurately the PL decay transients, hence demonstrating no change in dynamics due to spinning parameters.

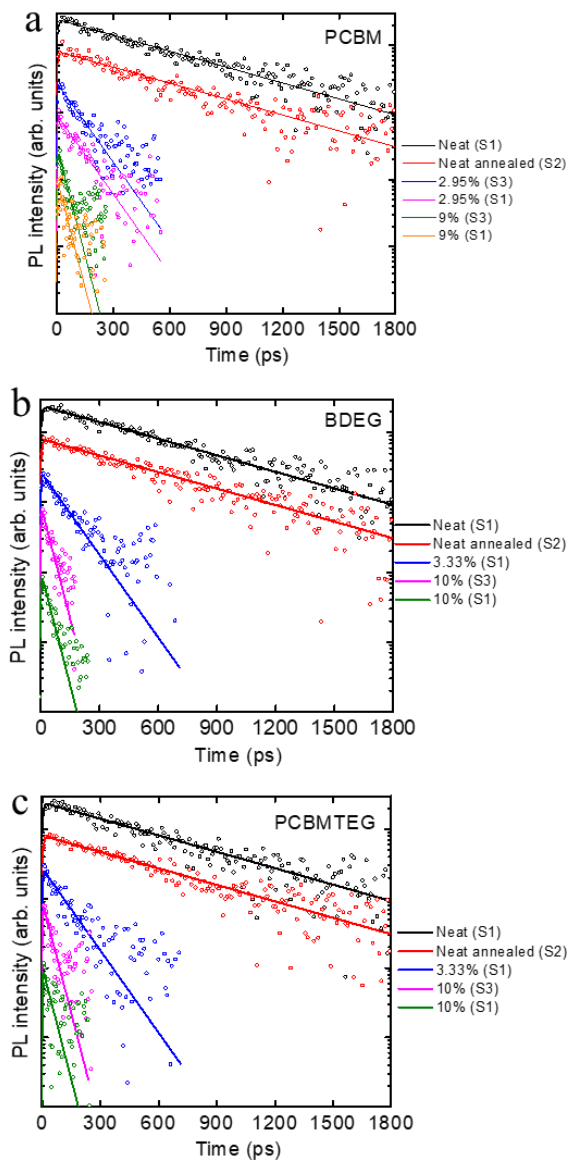


Figure 3.12. Normalized logarithmic PL decay transients of the neat films (black circles) and mixed films with different quencher/donor molar ratios (colored circles) prepared using different spinning parameters S1 = 250 rpm 1s, 700 rpm 40s; S2 = 500 rpm 40s, 1000 rpm 10s; S3 = 800 rpm 40s, 1000 rpm 10s. The solid lines show the Monte Carlo modeled PL decay transients. For clarity, each PL transient is re-scaled by a factor of 3 with respect to the previous. (a) PCBM, (b) BDEG, (c) PCBMTEG.

We now shift our focus to the samples without quenching (BTEG and BTREG). Here, we firstly checked the possibility of PL dynamics change with respect to spinning parameters and concentration of solution for blends with 11.1% molar ratio (Figure 3.13). All the PL decay transients were fit with a mono-exponential decay function with lifetime of 550 ps same as the neat films, which demonstrates no change in PL decay due to spinning parameters and concentration of solutions. Additionally, we prepared the BTREG blends using different solvents (Figure 3.14) and still did not observe any quenching. The fast component of PL decay transient in Figure 3.13a (sample, 800 rpm -S2-magenta) is due to leakage of excitation light into the streak camera.

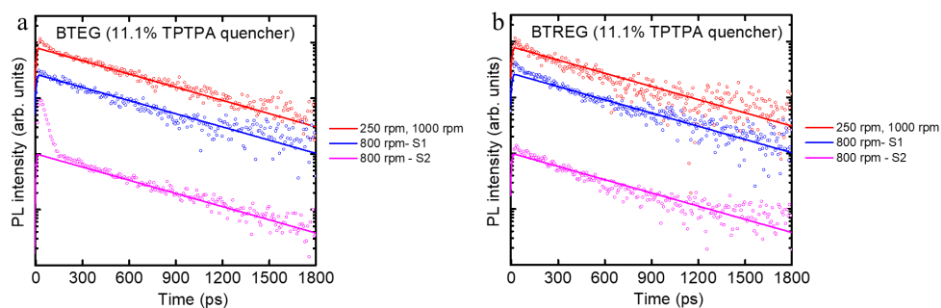


Figure 3.13. Normalized logarithmic PL transients of mixed films with 11.1% quencher/donor molar ratios (colored circles) prepared with different concentrations. The solid lines are the mono-exponential fitting with a decay time of 550 ps. (a) BTEG, (b) BTREG.

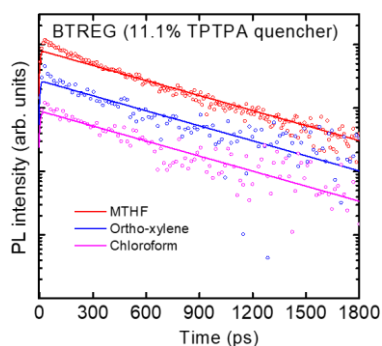


Figure 3.14. Normalized logarithmic PL decay transients of mixed films with 11.1% quencher/donor molar ratio (colored circles) prepared using different solvents, MTHF

(red), ortho-xylene (in blue) and chloroform (magenta). The solid lines are the mono-exponential fitting with a decay time of 550 ps.

To finalize we used different quenchers, namely OT and BDT. Surprisingly enough, still no signature of PL quenching was observed even at molar ratios as high as 50 % (Figure 3.15).

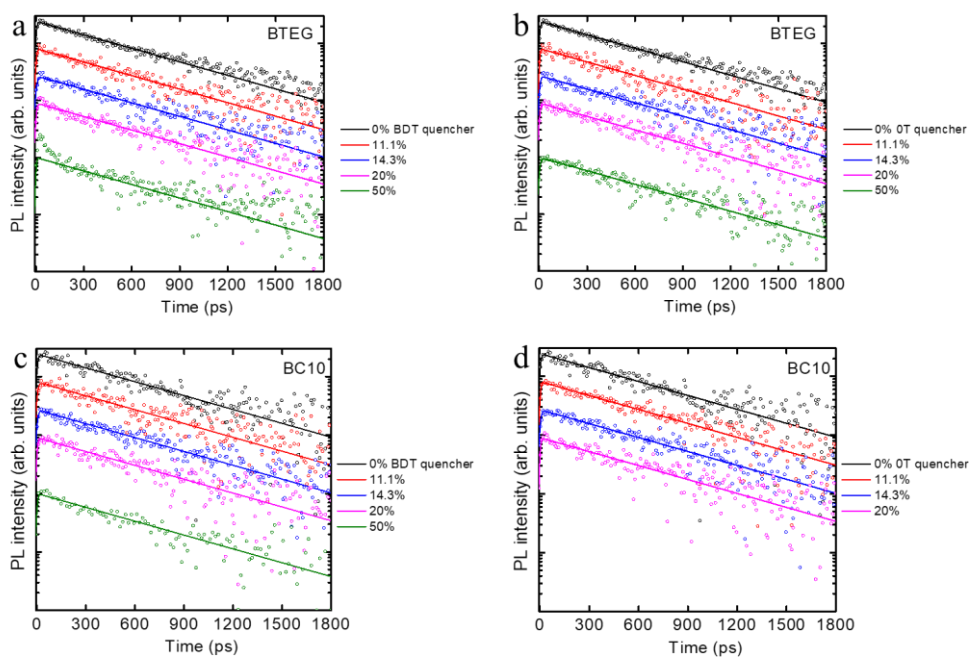


Figure 3.15. Normalized logarithmic PL decay transients of the neat films (black circles) and mixed films with different quencher/donor molar ratios (colored circles). The solid lines are the mono-exponential fitting with a decay time of 550 ps. (a) BTEG and BDT, (b) BTEG and OT, (c) BC10 and BDT, (d) BC10 and OT.

3.5.3 Monte Carlo Simulations

The description of Monte Carlo simulations can be found in chapter 2 and the input and output parameters are shown in Table 3.1.

The average size of the molecules over three dimensions was estimated as:

$$S = \sqrt[3]{\frac{M_m}{\rho N_A}} \quad (3.2)$$

where S is the size of the molecule, ρ is the density of the molecules (1.5 g.cm^{-3}), M_m is the molecular mass, N_A is the Avogadro constant.

Table 3.1. Monte Carlo Simulations parameters.

Description	Parameter	Value
Lifetime	τ	550 ps
Hopping distance	S	$\sim 1.1 \text{ nm}$
Quencher fraction	QF	Variable from 0 to 0.1
Energetic disorder	σ	$\sim 25 \text{ meV}$
Hopping time	τ	$\sim 2 \text{ ps}$
Exciton diffusion length	L_D	$\sim 10 \text{ nm}$
Exciton diffusion coefficient	D	$\sim 5 \times 10^{-4} \text{ cm}^2 \text{ s}^{-1}$

The exciton diffusion length of $\sim 10 \text{ nm}$ was determined from the displacement statistics as the mean value (Figure 3.7). The exciton diffusion coefficient of $D \sim 5 \times 10^{-4} \text{ cm}^2 \text{ s}^{-1}$ was determined using the differential form of Einstein-Smoluchowski relation $D = \frac{\partial \langle l^2(t) \rangle}{6\partial t}$, where $\langle l^2(t) \rangle$ is the average square of excitons displacement and t is the hopping time.

3.5.4 Estimation of Average Distance between Excitons

The number of excitons per unit area (i.e., the exciton density) is calculated as

$$n_e = \left(\frac{P_{avg}}{f_{rep}} \right) \left(\frac{\lambda_{exc}}{hc} \right) (1 - 10^{-OD(\lambda_{exc})}) \left(\frac{1}{\pi r_{focal}^2} \right) \quad (3.3)$$

where P_{avg} is the average excitation power, f_{rep} is the repetition rate of laser pulses, λ_{exc} is the excitation wavelength, h is the Planck constant, c is the speed of light, $OD(\lambda_{exc})$ is the optical density at the excitation wavelength, r_{focal} is the radius of excitation spot. The terms in the first and second brackets account to the number of excitons, the term in the third bracket factors in the percentage of absorbed photons at the excitation wavelength and the last bracket term computes the area of the excitation spot. The average distance between excitons can be estimated as one over square root of the exciton density, $d = \frac{1}{\sqrt{n_e}}$.

Table 3.2. Average distance between excitons parameters.

Description	Parameter	Values	
Average excitation power	P_{avg}	10-200 μ W	30-340 μ W
Repetition rate of laser pulses	f_{rep}	76 MHz	2 MHz
Excitation wavelength	λ_{exc}	550 nm	450 nm
Optical density at excitation wavelength	$OD(\lambda_{exc})$	0.22	0.3
Radius of the excitation spot	r_{focal}	30 μ m	110 μ m
Exciton density	n_e	$5 \times 10^{13} - 1 \times 10^{15} \text{ cm}^{-2}$	$4 \times 10^{14} - 5 \times 10^{15} \text{ cm}^{-2}$
Average distance between excitons	d	140 - 30 nm	50 - 15 nm

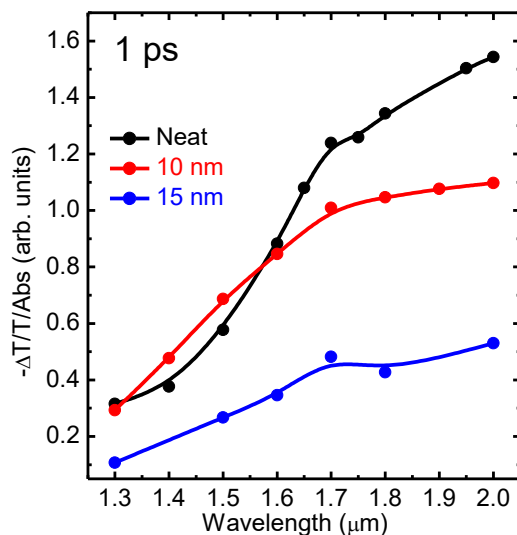
Author Contributions

B.A.L.R. performed time-resolved PL measurements, Monte Carlo simulations and interpreted the data. A. V. K. performed the EEA experiments at 405 nm. S.R and F.S.v.K synthesized the C70 derivatives under supervisor of J.C.H. S.B. synthesized BDT-PhTEG under the supervision of R.C.C. S.R prepared the samples and performed the AFM measurements. Y.N.L. synthesized the 0T molecule. R.C.C and M.S.P supervised the research.

3.6 References

1. Frenkel, J. On the transformation of light into heat in solids. i. *Phys. Rev.* **37**, 17–44 (1931).
2. Tang, C. W. Two-layer organic photovoltaic cell. *Appl. Phys. Lett.* **48**, 183–185 (1986).
3. Seo, J. W. *et al.* Columnar-Structured Low-Concentration Donor Molecules in Bulk Heterojunction Organic Solar Cells. *ACS Omega* **3**, 929–936 (2017).
4. Hedley, G. J. *et al.* Determining the optimum morphology in high-performance polymer-fullerene organic photovoltaic cells. *Nat. Commun.* **4**, 2867 (2013).
5. Firdaus, Y. *et al.* Long-range exciton diffusion in molecular non-fullerene acceptors. *Nat. Commun.* **11**, 5220 (2020).
6. Chow, P. C. Y., Albert-Seifried, S., Gélinas, S. & Friend, R. H. Nanosecond Intersystem Crossing Times in Fullerene Acceptors: Implications for Organic Photovoltaic Diodes. *Adv. Mater.* **26**, 4851–4854 (2014).
7. Bensasson, R. V. *et al.* Pulse radiolysis study of buckminsterfullerene in benzene solution. Assignment of the C60 triplet-triplet absorption spectrum. *Chem. Phys. Lett.* **201**, 326–335 (1993).
8. Guldi, D. M. & Prato, M. Excited-State Properties of C 60 Fullerene Derivatives. *Acc. Chem. Res.* **33**, 695–703 (2000).
9. Watanabe, A., Ito, O., Watanabe, M., Saito, H. & Koishi, M. Excited States of C 70 and the Intersystem Crossing Process Studied by Picosecond Time-Resolved Spectroscopy in the Visible and Near-IR Region. *J. Phys. Chem.* **100**, 10518–10522 (1996).
10. Wasielewski, M. R., O’Neil, M. P., Lykke, K. R., Pellin, M. J. & Gruen, D. M. Triplet states of fullerenes C60 and C70. Electron paramagnetic resonance spectra, photophysics, and electronic structures. *J. Am. Chem. Soc.* **113**, 2774–2776 (1991).
11. Arbogast, J. W. *et al.* Photophysical properties of sixty atom carbon molecule (C60). *J. Phys. Chem.* **95**, 11–12 (1991).
12. Keiderling, C., Dimitrov, S. & Durrant, J. R. Exciton and Charge Generation in PC 60 BM Thin Films. *J. Phys. Chem. C* **121**, 14470–14475 (2017).
13. Causa’, M., Ramirez, I., Martinez Hardigree, J. F., Riede, M. & Banerji, N. Femtosecond Dynamics of Photoexcited C 60 Films. *J. Phys. Chem. Lett.* **9**, 1885–1892 (2018).

14. Cook, S., Furube, A., Katoh, R. & Han, L. Estimate of singlet diffusion lengths in PCBM films by time-resolved emission studies. *Chem. Phys. Lett.* **478**, 33–36 (2009).
15. Raul, B. A. L. *et al.* Excited state dynamics and exciton diffusion in triphenylamine/dicyanovinyl push–pull small molecule for organic optoelectronics. *Sci. Rep.* **10**, 1–10 (2020).
16. Simón Marqués, P. *et al.* Triphenylamine/Tetracyanobutadiene-Based π -Conjugated Push–Pull Molecules End-Capped with Arene Platforms: Synthesis, Photophysics, and Photovoltaic Response. *Chem. – A Eur. J.* **26**, 16422–16433 (2020).
17. Qian, D. *et al.* Design rules for minimizing voltage losses in high-efficiency organic solar cells. *Nat. Mater.* **17**, 703–709 (2018).
18. Hennebicq, E. *et al.* Exciton Migration in Rigid-Rod Conjugated Polymers: An Improved Förster Model. *J. Am. Chem. Soc.* **127**, 4744–4762 (2005).
19. Beljonne, D. *et al.* Interchain vs. intrachain energy transfer in acceptor-capped conjugated polymers. *Proc. Natl. Acad. Sci.* **99**, 10982–10987 (2002).
20. Athanasopoulos, S., Hennebicq, E., Beljonne, D. & Walker, A. B. Trap Limited Exciton Transport in Conjugated Polymers. *J. Phys. Chem. C* **112**, 11532–11538 (2008).
21. Mikhnenko, O. V. *et al.* Trap-Limited Exciton Diffusion in Organic Semiconductors. *Adv. Mater.* **26**, 1912–1917 (2014).
22. Mikhnenko, O. V., Blom, P. W. M. & Nguyen, T.-Q. Exciton diffusion in organic semiconductors. *Energy Environ. Sci.* **8**, 1867–1888 (2015).
23. Reuswig, P. D., Congreve, D. N., Thompson, N. J. & Baldo, M. A. Enhanced external quantum efficiency in an organic photovoltaic cell via singlet fission exciton sensitizer. *Appl. Phys. Lett.* **101**, 113304 (2012).
24. Kozlov, O. V. *et al.* Real-Time Tracking of Singlet Exciton Diffusion in Organic Semiconductors. *Phys. Rev. Lett.* **116**, 057402 (2016).
25. Raul, B. A. L. *et al.* Excited state dynamics and exciton diffusion in triphenylamine/dicyanovinyl push–pull small molecule for organic optoelectronics. *Sci. Rep.* **10**, 21198 (2020).
26. Kim, T.-M., Shim, H.-S., Choi, M.-S., Kim, H. J. & Kim, J.-J. Multilayer Epitaxial Growth of Lead Phthalocyanine and C 70 Using CuBr as a Templating Layer for Enhancing the Efficiency of Organic Photovoltaic Cells. *ACS Appl. Mater. Interfaces* **6**, 4286–4291 (2014).
27. Rousseva, S. *et al.* Investigating the dielectric properties and exciton diffusion in C 70 derivatives. *Phys. Chem. Chem. Phys.* **24**, 13763–13772 (2022).
28. Luponosov, Y. N. *et al.* Effect of oligothiophene π -bridge length in D- π -A star-shaped small molecules on properties and photovoltaic performance in single-component and bulk heterojunction organic solar cells and photodetectors. *Mater. Today Energy* **22**, 100863 (2021).



Chapter 4. Charge Carrier Generation in Star-Shaped Molecule for Single-Component Organic Solar Cells

Star-shaped molecules represent a promising class of organic materials for optoelectronics applications due to their multiple channels of charge generation. In this chapter, we elucidate the role of intermolecular interactions on the excited state lifetime and charge carrier generation in BTI(2T – CNA – EHex)₃ molecule using time-resolved photoluminescence and femtosecond pump-probe transient absorption measurements. By varying the intermolecular separation, we found that the bi-exponential photoluminescence decay in the neat film is attributed to the formation of inter-molecular charge transfer (CT) excitons that undergo charge carrier generation. In this manner, the promotion of intermolecular CT excitons is found to be a feasible way to improve charge carrier generation. These findings are further discussed in terms of applications for single-component organic solar cells based on small molecule homojunctions.

4.1 Introduction

Organic solar cells (OSCs) have recently been in the spotlight owing to their continuously rising power conversion efficiency (PCE) and stability¹⁻⁹. Several processes determining the power conversion efficiency of OSCs are different from those of their inorganic counterparts¹⁰⁻¹². Consequently, despite extensive research in organic photovoltaics field, many fundamental aspects of light-to-charge conversion are still open for debate¹³⁻¹⁵. Due to the intrinsically low dielectric constant of organic materials, the photoexcitation of organic semiconductors results in a strongly bound electron-hole pair called Frenkel exciton¹³. The Frenkel exciton binding energy is usually above the average thermal energy at room temperature of ~25 meV, which makes exciton dissociation at room temperature less probable¹³. Typically, for an efficient exciton-to-charge carrier conversion in OSCs, a heterojunction consisting of electron donating and accepting materials with different energy levels is used to create an energy level offset that overcomes the Coulomb attraction between the electrons and holes.

There are several classes of donor materials^{16,17}, and among them star-shaped molecular donors are the most promising for efficient exciton dissociation¹⁷⁻¹⁹. The reason for this is their distinctive structure that involves a combination of intramolecular donor and acceptor units, which promotes the delocalization of electron density at the lowest unoccupied molecular orbital to be mainly along the acceptor units of the molecule¹⁸. As a result, the initial exciton dissociation is achieved – or even in some cases a complete exciton dissociation into charge carriers is possible – without the need of an external acceptor¹⁹. In this regard, star-shaped molecules represent a very attractive class of materials not only for bulk heterojunction (BHJ) architecture, but also for single-component OSCs^{17,19-22}. Although there has been some in-depth research on the photo-physics of star-shaped molecules^{18,19,23}, the role of intermolecular interactions on the bimodal nature of photoluminescence (PL) decay^{18,19,23} and charge carrier generation has not been unambiguously elucidated.

In this Chapter, we focus on photophysical studies of the BTI(2T – CNA – EHex)₃ molecule²⁴ (Figure 4.1) as a model system geared toward applications in single-component OSCs based on small-molecules homojunctions. To clarify the nature of bi-exponential PL decay in neat films^{18,19,23}, we compare the PL decay transients of BTI(2T – CNA – EHex)₃ molecules at different intermolecular separations. The time-resolved PL results are combined with pump-probe transient absorption measurements, from which we demonstrate that the bi-exponential PL decay in neat

film is due to the formation of intermolecular charge transfer (CT) excitons that undergo charge carrier generation. The obtained results elucidate the role of intermolecular interactions for charge carrier generation.

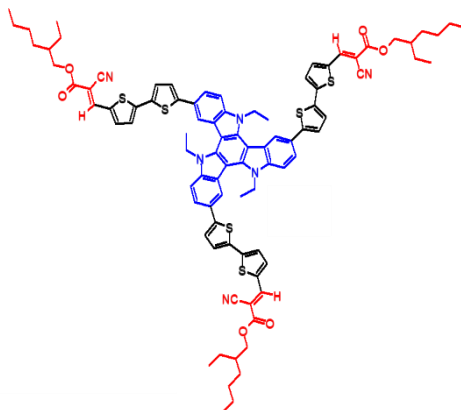


Figure 4.1. Chemical structure of BTI(2T – CNA – EHex)₃. The molecule was provided by Dr. Yuriy N. Luponosov, and the synthesis details can be found in reference [24].

4.2 Results and Discussion

4.2.1 Absorption and Photoluminescence Spectra

The normalized absorption and PL spectra of BTI(2T – CNA – EHex)₃ neat film and at different intermolecular separations in poly(methyl methacrylate) (PMMA) matrix are presented in Figure 4.2a. PMMA acts as an optically inactive dispersing agent that allows for comparison of the densely packed molecules in the neat films versus the isolated molecules in the solid state^{25,26}. The absorption spectra is typical of star-shaped molecules^{19,27–37} with two bands (below 410 nm and in the 410–700 nm range) usually assigned as having a mixed character from the $\pi - \pi^*$ transition in BTI-2T unit and the intramolecular charge transfer between the electron-donating (BTI) and electron-withdrawing (CNA) units. As the intermolecular separation decreases, the intermolecular interactions become stronger, resulting in pronounced red-shift of the absorption maximum peak from 500 nm (~ 2.48 eV) in highly isolated molecules (at 25 nm intermolecular separation) to 530 nm (~ 2.34 eV) in the neat film. Similarly, there is red-shift of PL spectra from 600 nm (2.07 eV) in highly isolated molecules to 690 nm (~ 1.8 eV) in neat films. The PL spectral width becomes broader (from 0.3 eV to 0.5 eV, as measured at the full width at half maximum) as the intermolecular separation decreases from 25 nm to 10 nm. This reflects the fact that

in the intermediate separation regime (between 25 nm to neat film), the PL spectra possesses contributions from both densely packed molecules (as in the neat film) and highly isolated molecules (as at 25 nm intermolecular separation).

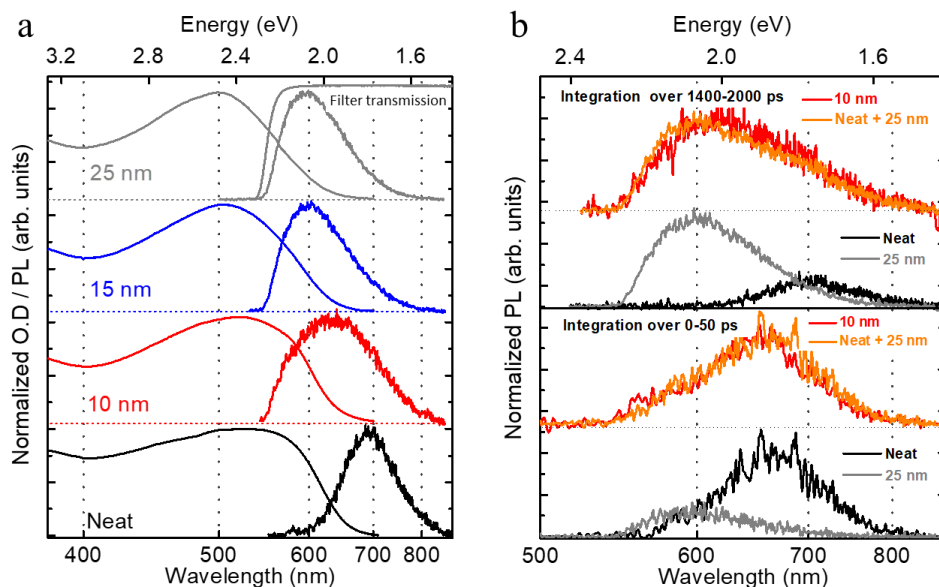


Figure 4.2. (a) Absorption and PL spectra of neat film and at different intermolecular separations. The transmission of 550 nm long-pass filter used to suppress the excitation light in the detection channel during all the experiments is represented by a gray solid line. (b) PL spectra of 10 nm (red lines), 25 nm (gray lines) and neat film (black lines) integrated over the time range of 1400–2000 ps (top panel) and 0–50 ps (bottom panel). The orange color represent the PL spectra of 10 nm obtained as a linear combination of neat film and 25 nm at the different integration times. The PL spectra of 10 nm was scaled to unit integral (i.e., converted to a probability density function).

In Figure 4.2b, we demonstrate the decomposition of PL spectra of the sample with 10 nm intermolecular separation into a linear combination of PL spectra of neat film and the sample with 25 nm intermolecular separation. At early times (0–50 ps) and lower energies, the contributions to the PL spectra of the sample with 10 nm intermolecular separation is 70% from densely packed molecules and 30% from highly isolated molecules. At later times (1400–2000 ps) and higher energies, the relative contributions switch with 70% of the PL belonging to highly isolated molecules and the remaining 30% to densely packed molecules. This further reiterates that in the intermediate separation regime, the PL bears both contributions

from densely packed and isolated molecules. Such contributions will also be reflected in the PL decay transients as it will be discussed later.

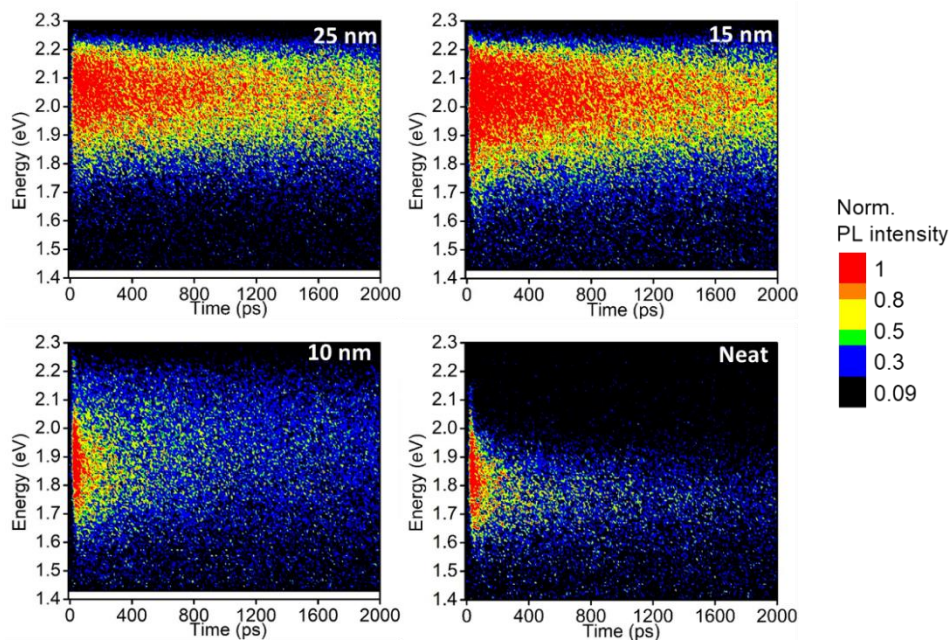


Figure 4.3. Normalized PL maps of molecules at different intermolecular separations. The excitation wavelength was 520 nm.

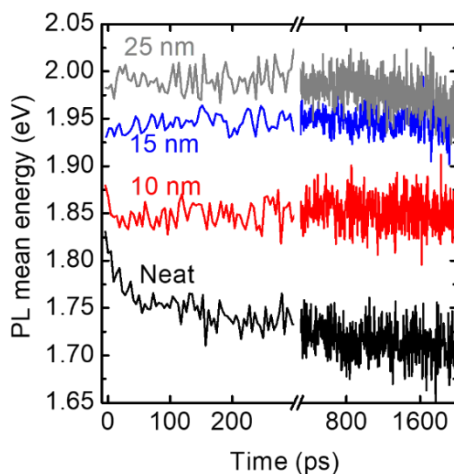


Figure 4.4. PL mean energy shifts of molecules at different intermolecular separations. The PL mean energy as a function of time was calculated as $\langle \omega(t) \rangle = \int \omega S(\omega, t) d\omega / \int S(\omega, t) d\omega$.

The PL mean energy shift is calculated as the time-dependence of the mean frequency of spectral slices of PL maps (Figure 4.3). In disordered medium, the PL mean energy shift originates from exciton downhill migration to lower energy sites³⁸. With a lack of intermolecular interactions, the excitations become highly localized at 25 nm intermolecular separation, thus, the PL mean energy shift is ~ 0 eV (Figure 4.4). Conversely, in a neat film with stronger intermolecular interactions, the excitation is no longer confined to a particular molecule, thus, the excitation can migrate over several molecules, and the PL mean energy shift is ~ 0.1 eV (Figure 4.4). Note that at short delays, the PL mean energy shift for 15 nm intermolecular separation (Figure 4.4) may not be noticeable. This is because the filter (OG 550) used to suppress the excitation light in the detection channel during all the experiments cropped a portion of high energy photons as shown in Figure 4.2a. In the excited state lifetimes section, we demonstrate that the PL transient of 15 nm captures the fast relaxation at early times, reinforcing that there is a PL mean energy shift at 15 nm, albeit a small one.

The observed PL mean energy shifts clearly indicate that relaxation channels with lower energies emerge with gradual increase of intermolecular interactions. We assign the relaxation channels with lower energies to intermolecular CT states, as we next demonstrate that they are associated with PL nonradiative decay and the generation of charge carriers. Intermolecular CT states refers to the intermediate state that precedes exciton dissociation in the neat film, and the hole partially resides in the intramolecular donor unit of one molecule and the electron in the intramolecular acceptor unit of another molecule. This should not be confused with interfacial charge transfer state of heterojunctions where the hole and electrons partially reside in different donor and acceptor materials, respectively.

4.2.2 Excited State Lifetimes

Figure 4.5 shows PL decay transients of neat film and at different intermolecular separations, the respective fitting parameters are presented in Table 4.1. At 25 nm intermolecular separation, when the molecules are highly isolated and the intermolecular interactions are negligible, the PL decays mono-exponentially with a lifetime of 2.7 ns. As the intermolecular separation decreases, the transients become bi-exponential. At 15 nm intermolecular separation, the fastest decaying component of 90 ps contributes with 24% of the relaxation dynamics, and the remaining 76% is contributed by the slower component of 2.4 ns. The share of the fastest component

increases from 24% at 15 nm intermolecular separation to 60% in neat film and the time constant decrease from 90 ps to 60 ps, respectively. This is an indication that the relaxation channels with lower energies (intermolecular CT states) emerging from gradual increase of intermolecular interactions promote the initial fast relaxation of the PL decay. The slower component's shares also change from 76% at 15 nm intermolecular separation to 30% in the neat film and the time constants decreases from 2.4 ns to 1.2 ns, which shows that relaxations through the intermolecular CT states are still prevalent at later times. Thus, the fast and slow PL decay components are attributed to the prompt and delayed formation of intermolecular CT excitons, respectively. These results indicate that the measured PL decay time constants in neat film are associated with exciton decay rates through the intermolecular CT states, i.e., the formation rate of intermolecular CT excitons. Intermolecular CT excitons arise from a partial charge separation of Frenkel excitons in the neat film, where the electrons and holes despite still being coupled to a similar lattice distortion, experience a weaker Coulomb attraction compared to Frenkel excitons.

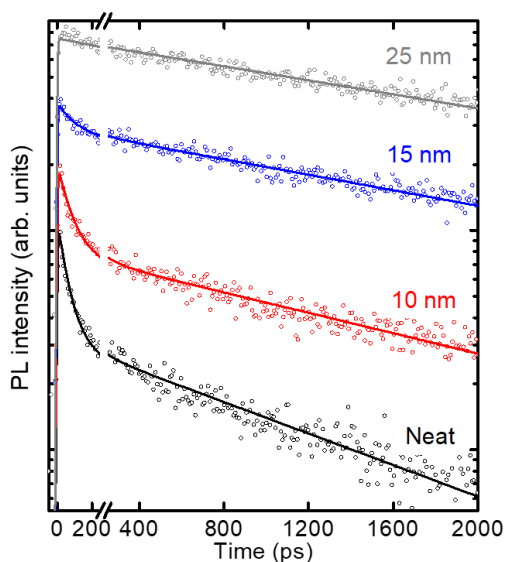


Figure 4.5. PL decay transients of neat film and at different intermolecular separations. The dots represent the experimental data, the lines are the respective fittings convoluted with a Gaussian apparatus function of ~ 10 ps according to Table 1. The excitation wavelength was 520 nm.

The measured PL decay rates at different intermolecular separations (K) can be described as the sum of radiative (K_r) and nonradiative (K_{nr}) decay rates:

$$K = K_r + K_{nr} = K_{25\text{ nm}} + K_{ICT} \quad (4.1)$$

where K is the measured PL decay rates (obtained using $K = 1/\tau_{avg}$), $K_{25\text{ nm}}$ is the measured PL decay rate at 25 nm intermolecular separation and corresponds to the radiative decay rate, K_{ICT} is the rate of intermolecular CT excitons formation which corresponds to the nonradiative decay rate. From Equation (4.1), it follows that the rate of intermolecular CT exciton formation is expressed as $K_{ICT} = K - K_{25\text{ nm}}$. The decay rate values are presented in Table 4.1. As the intermolecular separation decreases more intermolecular CT states are formed, which leads to increase in the rate of formation of intermolecular CT excitons from $0.5 \times 10^{-4} \text{ ps}^{-1}$ at 15 nm intermolecular separation to $5.6 \times 10^{-4} \text{ ps}^{-1}$ in the neat films.

The relative yield of intermolecular CT exciton formation (Y_{ICT}) can be derived using the decay rates as

$$Y_{ICT} = \frac{K_{ICT}}{K_{ICT} + K_{25\text{ nm}}} = \frac{K_{ICT}}{K} \quad (4.2)$$

thus, for the neat film $Y_{ICT} = 0.6$, i.e., 60 % of absorbed photons generate intermolecular CT excitons, and the remaining 40% are the conventional Frenkel excitons that either contribute to light emission or undergo thermal relaxation.

The formation of charge carriers is typically preceded by the dissociation of charge transfer excitons¹³⁻¹⁵. To support our assignment of the fast relaxation of the PL decay in the neat film is due to formation of intermolecular CT excitons, we performed transient absorption measurements to investigate the charge carrier dynamics.

Table 4.1. PL lifetimes obtained from exponential fitting convoluted with a Gaussian apparatus function of ~10 ps and the PL decay rates.

	25 nm	15 nm	10 nm	Neat
$\tau_1(a_1)$, ps	-	90 (0.24)	80 (0.6)	60 (0.7)
$\tau_2(a_2)$, ns		2.4 (0.76)	1.8 (0.4)	1.2 (0.3)
τ_{avg} , ns	2.7	2.4	1.7	1.08
K , $\text{ps}^{-1}(10^{-4})$	3.7	4.2	5.8	9.3
K_{ICT} , $\text{ps}^{-1}(10^{-4})$	0	0.5	2.1	5.6
Y_{ICT} , %	0	12	36	60

4.2.3 Charge Carrier Dynamics

Numerous studies have demonstrated that when charge carriers are generated on conjugated molecules, additional absorption bands emerge in the near-infrared region^{13–15}. It should be noted that the intensity of such near-infrared bands is proportional to the number of charge carriers. Hence, for the transient absorption measurements (see Figure 4.10 for setup), the samples were excited with an ultrashort visible laser pulse (pump), and a near-infrared delayed pulse (probe) was used to detect the absorption of the charge carriers.

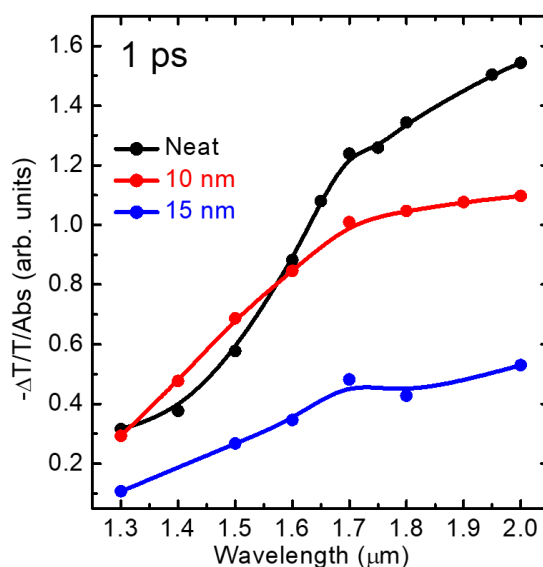


Figure 4.6. Excited state absorption (ESA) spectra of neat film and at different intermolecular separations taken at 1 ps time delay. The spectra were constructed using the ESA transients measured at different probe wavelengths upon 550 nm excitation, and normalized by the absorption of the samples (i.e., the number of absorbed photons) to allow direct comparison of different samples.

Figure 4.6 shows the near-infrared excited state absorption (ESA) spectra of neat film and at different intermolecular separations upon 550 nm excitation. The spectra were constructed from the ESA transients measured at several probe wavelengths, and normalized by the number of absorbed photons. For highly isolated molecules (at 25 nm intermolecular separation) the ESA signal was not at the detectable level even at higher excitation fluences. At 15 nm intermolecular separation, the ESA signal is clearly detectable, albeit weak. With further decrease of intermolecular

separation, the ESA signal became stronger with the maximum amplitude attained in the neat film. This is clear evidence that the ESA spectra mostly reflects the optical signature from intermolecular excitations (intermolecular CT excitons) rather than “intramolecular” excitations (strongly bound Frenkel excitons). Hence, we can reasonably conclude that most of the signal in the neat film is from intermolecular CT excitons.

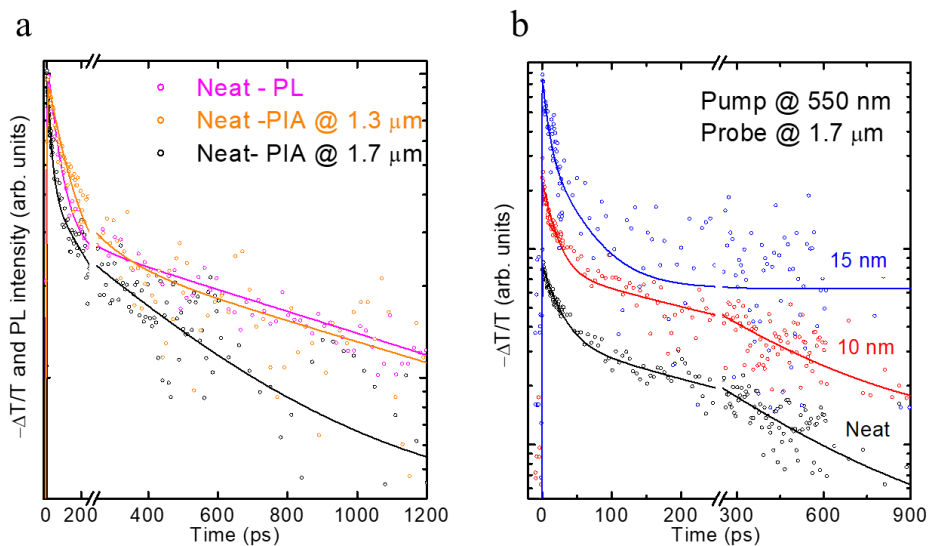


Figure 4.7. (a) Normalized PL decay (magenta) and ESA transients of neat film measured at 1.3 μm (orange) and 1.7 μm (black) probe wavelengths. (b) ESA transients of neat film (black) and at different intermolecular separations (different colors), obtained upon 550 nm excitation and probed at 1.7 μm . Circles represent the experimental data while solid lines are the respective bi-exponential fitting convoluted with a Gaussian apparatus function of ~ 0.2 ps according to Table 4.2.

Table 4.2. ESA transients fitting convoluted with a Gaussian apparatus function of ~ 0.2 ps.

	25 nm	15 nm	10 nm	Neat
$\tau_1(a_1)$, ps	-	10 (0.6)	15 (0.7)	25 (0.6)
$\tau_2(a_2)$, ps	-	50 (0.4)	380 (0.3)	400 (0.4)
τ_{avg} , ps	-	40	350	370

Figure 4.7 shows the ESA transients of the neat film and at different intermolecular separations, the respective fitting parameters are presented in Table 4.2. In Figure 4.7a, we compare the neat film PL decay with the neat film ESA transients at 1.3 μm and 1.7 μm probe wavelengths. There is a clear match between PL decay and the ESA transients at 1.3 μm after considering the 10 ps instrument response of PL measurements. This presumably demonstrates that the excited state evolution leads to the recovery of the initial unperturbed state, i.e., the absorption at 1.3 μm is mainly due to intermolecular CT excitons that contribute to PL. However, the ESA transient at 1.7 μm is faster compared to PL decay transient. As the intermolecular CT excitons are the precursors of charge carrier generation¹³, we assign the ESA signal at 1.7 μm to be caused mainly by charge carrier absorption. Note that unlike the charge carriers generated in heterojunctions, in the neat film the charge carrier belongs to the same material and still experiences a coulomb attraction. Therefore, a further step is needed for the final charge carrier separation, for instance a built in or applied electric fields can drive the electron and holes towards opposite electrodes³⁹. This is in full agreement with our recent findings¹⁹ (see chapter 5), where we attribute a complete charge carriers separation in single-component OSCs based on small molecules homojunctions to be mediated by the electric fields.

In Figure 4.7b, we compare the ESA transients of different intermolecular separations probed at 1.7 μm where the charge carrier absorption is predominant. Similar to the neat film, all the ESA transients demonstrate a bi-exponential decay behavior. As the charge carrier generation is preceded by the intermolecular CT excitons formation (where the fast and slow PL decay components are associated with the prompt and delayed formation of intermolecular CT excitons), we associate the fast and slower ESA decay components to prompt and delayed generation of charge carriers, respectively. In the neat film, 60% of the relaxation dynamics is contributed by the fastest component (~ 25 ps time constant) and the remaining 40% by the slower component (~ 400 ps time constant). As the intermolecular separation increase, the ESA transients accelerate, and at 15 nm intermolecular separation the time constant of the fastest component reaches 10 ps and the slower component 50 ps. Such differences point towards a reduced probability of charge carrier generation through intermolecular CT states with increase of intermolecular separation.

The obtained results indicate that charge carrier generation in neat films is mainly mediated by the intermolecular charge separation between neighboring BTI(2T – CNA – EHex)₃ molecules. In this manner, we reason that the rate of intermolecular charge separation should also be directly dictated by the proximity between the intramolecular donor units of one molecule with the acceptor units of another

molecule in the film. An immediate implication of these results should be that, increasing the number of acceptor units in the star-shaped molecules would effectively increase the probability of intermolecular CT excitons formation, therefore maximizing charge carrier generation. We next demonstrate this scenario in the next PL volume quenching section, by mixing the BTI(2T – CNA – EHex)₃ molecules with small concentrations of external acceptor molecules as a way of mimicking the increase of intramolecular acceptor units.

4.2.4 Photoluminescence Volume Quenching

As previously mentioned, a possible way to maximize charge carrier generation would be to increase the number of intramolecular acceptor units in the star-shaped molecule. To that end, we blended the BTI(2T – CNA – EHex)₃ molecule with small concentrations of non-fullerene acceptor to mimic the increase of intramolecular acceptor units. A planar fused-ring electron acceptor (IC-C6IDT-IC) based on indacenodithiophene (Figure 4.8) was selected as the acceptor for having suitable energy level alignment with BTI(2T – CNA – EHex)₃ molecule^{24,40} which ensures minimum energy loss and efficient charge carrier generation. Furthermore, IC-C6IDT-IC has strong absorption in the 600-800 nm range⁴⁰, thus combined with BTI(2T – CNA – EHex)₃, the blend provides a wide absorption range from 400-800 nm (Figure 4.8) which maximizes sunlight harvesting for OSCs.

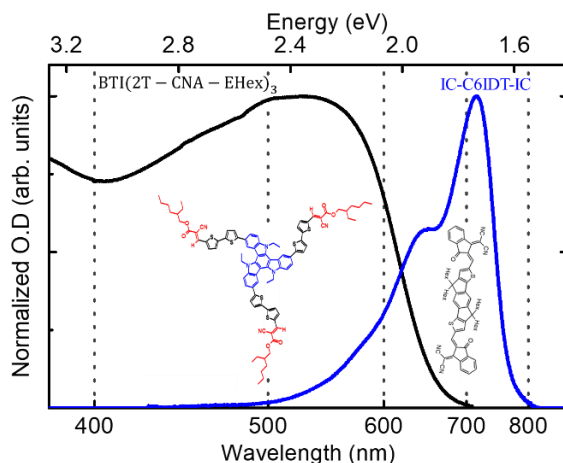


Figure 4.8. Absorption spectra of donor BTI(2T – CNA – EHex)₃ and acceptor IC-C6IDT-IC neat films with the respective chemical structures.

Figure 4.9 shows the PL decay transients of the BTI(2T – CNA – EHex)₃ neat films with increasing concentration of IC-C6IDT-IC. The IC-C6IDT-IC /BTI(2T – CNA – EHex)₃ molar ratios are kept in the low concentration regime varying from 0.95 % – 3%, such that IC-C6IDT-IC molecules simply acts as exciton quenching site facilitating charge generation through electron transfer. Incremental addition of IDIC molecules induces increase of shares of the fast PL decay component from 70% to 94% (at 3% molar ratio) and reduction of shares of the slow component from 30% to 6%. Note that the both the fast and slow time constants values remain the same as 60 ps and 1210 ps, respectively. Hence, if we assume the small added concentrations of IDIC as additional intramolecular acceptor units, the Y_{ICT} value increases from 60% to 75% (at 3% molar ratio).

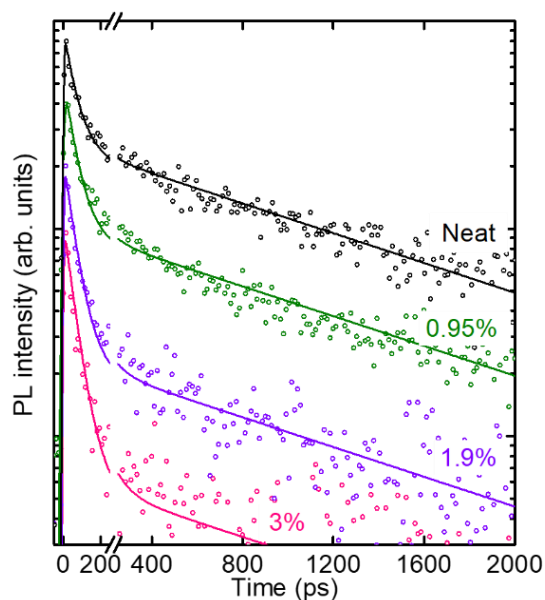


Figure 4.9. PL decay transients of neat film and films with different IDIC content. The dots represent the experimental data, the lines are the respective fittings convoluted with a Gaussian apparatus function of ~ 10 ps according to Table 4.3. The excitation wavelength was 520 nm. Each PL transient is re-scaled by a factor of 3 with respect to the previous for better visibility.

Balakirev *et al*²⁴, have demonstrated that the BTI(2T – CNA – EHex)₃ molecule when used in single-component OSCs produces an EQE of 4% which is quite low when compared to similar star shaped materials with EQE as high as 23% obtained by Mannanov *et al*⁴¹. Recently, we have studied the effect of oligothiophene bridge

elongation on the ultrafast photophysics of star-shaped molecules and made a correlation between the increases in Y_{ICT} with the increase in EQE in single-component OSCs¹⁹ (see chapter 5). By taking into account the aforementioned findings^{19,24,41}, the low EQE value of the BTI(2T – CNA – EHex)₃ single-component OSCs can be attributed to the lower $Y_{ICT} = 0.6$ value, compared to higher $Y_{ICT} = 0.85$ value of 3T molecule¹⁹ (see chapter 5) and possibly lower geminate recombination of intermolecular CT excitons. The obtained results suggest that increasing the number of intramolecular acceptor units improves the amount of charge generation in single-component OSCs.

Table 4.3. PL quenching fitting convoluted with a Gaussian apparatus function of ~10 ps

	Neat	0.95 %	1.9 %	3 %
$\tau_1(a_1)$, ps	60 (0.7)	60 (0.8)	60 (0.88)	60 (0.94)
$\tau_2(a_2)$, ps	1210 (0.3)	1210 (0.2)	1210 (0.12)	1210 (0.06)
τ_{avg} , ps	1090	1020	900	700

4.3 Conclusions

We have demonstrated that the bimodal nature of PL decay in BTI(2T – CNA – EHex)₃ neat film is driven by intermolecular interactions between neighboring molecules. We attribute this to be the reason behind the formation of intermolecular CT excitons that either contribute to the PL or undergo charge carrier generation. These results suggest that promoting intermolecular CT excitons is a feasible way to improve charge generation in single-component OSCs based on small molecules homojunctions. In the case of star-shaped materials, the further promotion of intermolecular CT excitons is possible either by increasing the numbers of intramolecular acceptor units²³ or by spatially increasing the separation between the intramolecular donor and acceptor units^{19,42} (see Chapter 5). This Chapter further highlights the broad potential of star-shaped molecules for the development of single material devices.

4.4 Methods

4.4.1 Sample Preparation

Neat and mixed films. BTI(2T – CNA – EHex)₃ and IDIC (provided by Dr. Yuriy N. Luponosov) were separately dissolved in chloroform at a concentration of 2 g/L and stirred at room temperature for 10 hours. The solutions were then mixed to achieve the desired IDIC/BTI(2T – CNA – EHex)₃ molar ratios (0.95% - 3%) and stirred for another 5 hours. The films were prepared by drop casting the solution in a plain glass substrate.

Matrices. PMMA (sigma Aldrich, Mw= 120000 g/mol) was dissolved in chloroform at a concentration of 150 g/L and stirred at room temperature for 8 hours. Solutions of star-shaped molecule BTI(2T – CNA – EHex)₃ and PMMA were mixed to achieve the desired average separation between BTI(2T – CNA – EHex)₃ molecules of 10 nm, 15 nm and 25 nm and stirred for 5 hours. The intermolecular separations were calculated as:

$$d = \sqrt[3]{\frac{M_m}{\rho N_A n_r}} = \sqrt[3]{\frac{1}{n_r}} \times 5.5 \text{ nm}, \quad (4.3)$$

where, $\rho = 1.18 \text{ g. cm}^{-3}$ is the density of PMMA, $M_m = 120000 \text{ g. mol}^{-1}$ is the molecular mass of PMMA, N_A is the Avogadro constant, n_r is the BTI(2T – CNA – EHex)₃ /PMMA molar ratio.

The matrices were prepared by drop casting the mixed solutions in microscope cover glass substrates.

4.4.2 Time-resolved Photoluminescence

Time-resolved photoluminescence measurements were performed using a streak camera (Hamamatsu, C5680) and a spectrograph. The mode-locked output from the Ti:sapphire oscillator (Mira 900, 76 MHz repetition rate) was focused on the Newport SGC-800 hollow fiber producing a supercontinuum. The excitation wavelength of 520 nm was obtained by selecting a portion of the supercontinuum with a bandpass filter of 520 nm central wavelength and FWHM of 10 nm. A long pass filter (OG550) was placed before the spectrograph to filter the excitation stray light. The excitation power was set between 1-5 μW to avoid the possibility of exciton-exciton annihilation or photobleaching.

4.4.3 Transient Absorption

Excited state pump-probe absorption measurements were performed using the Light Conversion Carbide CB5 (230 fs, 1025 nm, 60 kHz repetition rate) to feed two optical parametric amplifiers (OPA) operating in the visible range of 520-900 nm (Light Conversion Orpheus-N-3H) and in the mid-IR range of 1300-2000 nm (Light Conversion Orpheus-ONE). The Orpheus-N-3H was set at 550 nm (25 fs, pulse duration) near the absorption maximum of the samples and used as the excitation source (pump). The Orpheus-ONE output was varied in the 1300-2000 nm range (pulse duration of 100-350 fs) and used as the probe.

The polarization of the pump and probe pulses were linear and kept parallel during all the experiments. Neutral density filters were placed right after the outputs of Orpheus-N-3H and Orpheus-ONE to control the pump and probe powers. A low excitation fluence of $10 \mu\text{J cm}^{-2}$ was employed to avoid exciton-exciton annihilation. The pump beam was directed into a LS-110 linear stage to control the time delay between the pump and probe pulses, subsequently on to a mechanical chopper set at 500 Hz to control the pump on and off stages, and then focused on to the sample. The probe beam was split to produce a reference beam (detected using a nitrogen cooled InAs detector) to account for intensity variations with the wavelength, and into the actual probe beam which was focused on to sample and spatially overlapped with the pump beam.

After the sample, the pump beam was blocked and the probe beam was directed into the nitrogen cooled InAs detector connected to a lock-in amplifier. Finally, the detected transmittance changes of the sample $-\Delta T$ with and without the excitation pulse (at 500 Hz chopper frequency) was normalized with the reference probe signal T to obtain $-\Delta T/T$. To allow for comparison between signals of different samples, $-\Delta T/T$ was further normalized by the absorption of the samples.

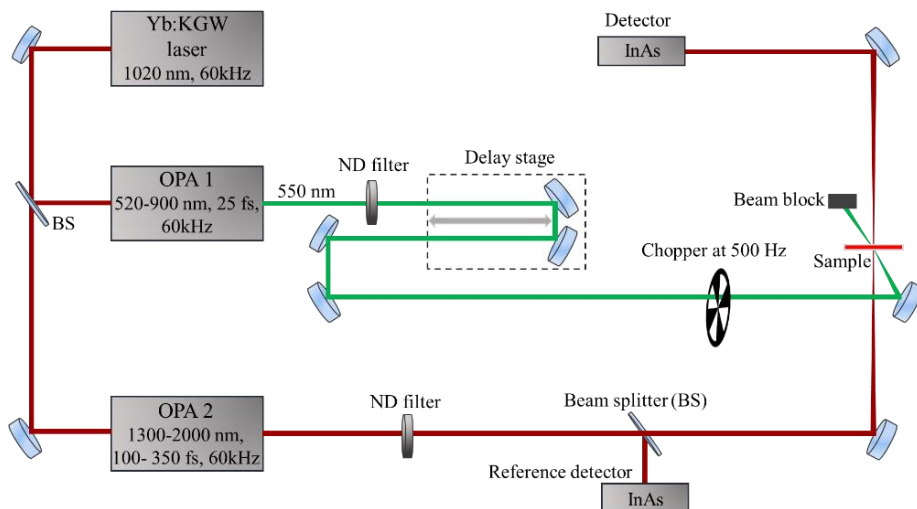


Figure 4.10. Schematic of the experimental apparatus for TA absorption.

Author Contributions

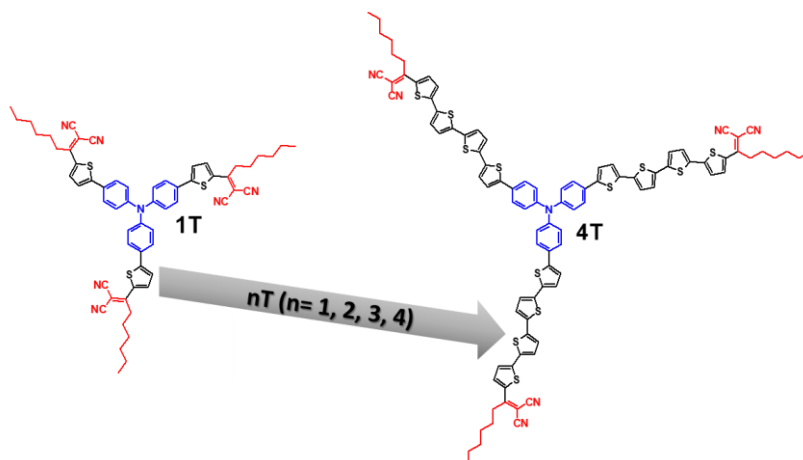
B.A.L.R and M.S.P conceptualized the project. B.A.L.R. performed the measurements and interpreted the data under the supervision of M.S.P. Y.N.L. provided the molecule.

4.5 References

1. Cheng, P. & Zhan, X. Stability of organic solar cells: challenges and strategies. *Chem. Soc. Rev.* **45**, 2544–2582 (2016).
2. Li, N. *et al.* Abnormal strong burn-in degradation of highly efficient polymer solar cells caused by spinodal donor-acceptor demixing. *Nat. Commun.* **8**, 14541 (2017).
3. Lee, J.-W. *et al.* Donor–Acceptor Alternating Copolymer Compatibilizers for Thermally Stable, Mechanically Robust, and High-Performance Organic Solar Cells. *ACS Nano* **15**, 19970–19980 (2021).
4. Cui, Y. *et al.* Single-Junction Organic Photovoltaic Cell with 19% Efficiency. *Adv. Mater.* **33**, 2102420 (2021).
5. Hong, L. *et al.* 18.5% Efficiency Organic Solar Cells with a Hybrid Planar/Bulk Heterojunction. *Adv. Mater.* **33**, 2103091 (2021).
6. Lin, Y. *et al.* 17.1% Efficient Single-Junction Organic Solar Cells Enabled by n-Type Doping of the Bulk-Heterojunction. *Adv. Sci.* **7**, 1903419 (2020).
7. Burlingame, Q. *et al.* Intrinsically stable organic solar cells under high-intensity illumination. *Nature* **573**, 394–397 (2019).
8. Jiang, Z. *et al.* Highly efficient organic photovoltaics with enhanced stability through the formation of doping-induced stable interfaces. *Proc. Natl. Acad. Sci.* **117**, 6391–6397 (2020).
9. Li, Y. *et al.* Non-fullerene acceptor organic photovoltaics with intrinsic operational lifetimes over 30 years. *Nat. Commun.* **12**, 5419 (2021).
10. Miles, R. W., Zoppi, G. & Forbes, I. Inorganic photovoltaic cells. *Mater. Today* **10**, 20–27 (2007).
11. Wang, J. *et al.* Highly efficient all-inorganic perovskite solar cells with suppressed non-radiative recombination by a Lewis base. *Nat. Commun.* **11**, 177 (2020).
12. Riede, M., Spoltore, D. & Leo, K. Organic Solar Cells—The Path to Commercial Success. *Adv. Energy Mater.* **11**, 2002653 (2021).
13. Few, S., Frost, J. M. & Nelson, J. Models of charge pair generation in organic solar cells. *Phys. Chem. Chem. Phys.* **17**, 2311–2325 (2015).
14. Gao, F. & Inganäs, O. Charge generation in polymer–fullerene bulk-heterojunction solar cells. *Phys. Chem. Chem. Phys.* **16**, 20291–20304 (2014).
15. Ostroverkhova, O. Organic Optoelectronic Materials: Mechanisms and Applications. *Chem. Rev.* **116**, 13279–13412 (2016).
16. Collins, S. D., Ran, N. A., Heiber, M. C. & Nguyen, T.-Q. Small is Powerful: Recent Progress in Solution-Processed Small Molecule Solar Cells. *Adv. Energy Mater.* **7**, 1602242 (2017).
17. Roncali, J. Single-Material Organic Solar Cells Based on Small Molecule Homo Junctions: An Outdated Concept or a New Challenge for the Chemistry and Physics of Organic Photovoltaics? *Adv. Energy Mater.* **11**, 2102987 (2021).
18. Kozlov, O. V. *et al.* Ultrafast Exciton-to-Polaron Conversion in Densely Packed Small Organic Semiconducting Molecules. *Adv. Opt. Mater.* **5**, 1700024 (2017).

19. Luponosov, Y. N. *et al.* Effect of oligothiophene π -bridge length in D- π -A star-shaped small molecules on properties and photovoltaic performance in single-component and bulk heterojunction organic solar cells and photodetectors. *Mater. Today Energy* **22**, 100863 (2021).
20. Jiang, X. *et al.* Miscibility-Controlled Phase Separation in Double-Cable Conjugated Polymers for Single-Component Organic Solar Cells with Efficiencies over 8 %. *Angew. Chemie Int. Ed.* **59**, 21683–21692 (2020).
21. Li, S. *et al.* Narrow-Bandgap Single-Component Polymer Solar Cells with Approaching 9% Efficiency. *Adv. Mater.* **33**, 2101295 (2021).
22. Wu, Y. *et al.* A conjugated donor-acceptor block copolymer enables over 11% efficiency for single-component polymer solar cells. *Joule* **5**, 1800–1815 (2021).
23. Salamatova, E. *et al.* Visualization of molecular excitons diffusion. in (eds. Bakulin, A. A., Lovrincic, R. & Banerji, N.) 99230K (2016). doi:10.1117/12.2237620
24. Balakirev, D. O. *et al.* Star-shaped benzotriindole-based donor-acceptor molecules: Synthesis, properties and application in bulk heterojunction and single-material organic solar cells. *Dye. Pigment.* **181**, 108523 (2020).
25. Raul, B. A. L. *et al.* Excited state dynamics and exciton diffusion in triphenylamine/dicyanovinyl push-pull small molecule for organic optoelectronics. *Sci. Rep.* **10**, 21198 (2020).
26. Simón Marqués, P. *et al.* Triphenylamine/Tetracyanobutadiene-Based π -Conjugated Push-Pull Molecules End-Capped with Arene Platforms: Synthesis, Photophysics, and Photovoltaic Response. *Chem. – A Eur. J.* **26**, 16422–16433 (2020).
27. Min, J. *et al.* Alkyl Chain Engineering of Solution-Processable Star-Shaped Molecules for High-Performance Organic Solar Cells. *Adv. Energy Mater.* **4**, 1301234 (2014).
28. Nicolas, Y. *et al.* Planarized Star-Shaped Oligothiophenes with Enhanced π -Electron Delocalization. *Org. Lett.* **6**, 273–276 (2004).
29. Leliège, A., Blanchard, P., Rousseau, T. & Roncali, J. Triphenylamine/Tetracyanobutadiene-Based D-A-D π -Conjugated Systems as Molecular Donors for Organic Solar Cells. *Org. Lett.* **13**, 3098–3101 (2011).
30. Min, J. *et al.* Interface Design to Improve the Performance and Stability of Solution-Processed Small-Molecule Conventional Solar Cells. *Adv. Energy Mater.* **4**, 1400816 (2014).
31. Min, J. *et al.* A solution-processable star-shaped molecule for high-performance organic solar cells via alkyl chain engineering and solvent additive. *Org. Electron.* **14**, 219–229 (2013).
32. Ponomarenko, S. A. *et al.* Design of donor-acceptor star-shaped oligomers for efficient solution-processible organic photovoltaics. *Faraday Discuss.* **174**, 313–339 (2014).
33. Luponosov, Y. N. *et al.* Effects of electron-withdrawing group and electron-donating core combinations on physical properties and photovoltaic performance in D- π -A star-shaped small molecules. *Org. Electron.* **32**, 157–168 (2016).

34. Kozlov, O. V. *et al.* Ultrafast Charge Generation Pathways in Photovoltaic Blends Based on Novel Star-Shaped Conjugated Molecules. *Adv. Energy Mater.* **5**, 1401657 (2015).
35. Luponosov, Y. N., Solodukhin, A. N. & Ponomarenko, S. A. Branched triphenylamine-based oligomers for organic electronics. *Polym. Sci. Ser. C* **56**, 104–134 (2014).
36. Luponosov, Y. N. *et al.* Star-shaped D– π –A oligothiophenes with a tris(2-methoxyphenyl)amine core and alkyldicyanovinyl groups: synthesis and physical and photovoltaic properties. *J. Mater. Chem. C* **4**, 7061–7076 (2016).
37. Min, J. *et al.* Integrated molecular, morphological and interfacial engineering towards highly efficient and stable solution-processed small molecule solar cells. *J. Mater. Chem. A* **3**, 22695–22707 (2015).
38. Bäessler, H. Charge Transport in Disordered Organic Photoconductors a Monte Carlo Simulation Study. *Phys. status solidi* **175**, 15–56 (1993).
39. Deibel, C. & Dyakonov, V. Polymer–fullerene bulk heterojunction solar cells. *Reports Prog. Phys.* **73**, 096401 (2010).
40. Lin, Y. *et al.* A Facile Planar Fused-Ring Electron Acceptor for As-Cast Polymer Solar Cells with 8.71% Efficiency. *J. Am. Chem. Soc.* **138**, 2973–2976 (2016).
41. Mannanov, A. L. *et al.* Charge photogeneration and recombination in single-material organic solar cells and photodetectors based on conjugated star-shaped donor-acceptor oligomers. *Org. Electron.* **78**, 105588 (2020).
42. Wang, J. *et al.* Increasing donor-acceptor spacing for reduced voltage loss in organic solar cells. *Nat. Commun.* **12**, 6679 (2021).



Chapter 5. Tailored Charge Carrier Generation in Star-Shaped Molecules for Enhanced Device Performance

Donor-acceptor molecules with thiophene fragments as the π -bridge represent a promising class of materials for organic photovoltaics especially in single-component organic solar cells and other related applications. In this chapter, we present an approach for controlling the charge carrier generation in star-shaped molecules films through variation of oligothiophene π -bridge length. We investigate the charge carrier generation and exciton diffusion of a series of star-shaped donor-acceptor molecules (**1T–4T**) by employing time-resolved photoluminescence measurements and Monte Carlo simulations. We found that variation of the π -bridge length from **1T** to **4T** results with decrease in excited state lifetime, which is attributed to efficient exciton-to-charge carrier conversion in the neat films. Exciton diffusion length is also found to decrease with the elongation of the π -bridge length as most of photo-generated excitons are immediately converted into charge carriers within the first 100 ps. The approach for manipulating charge carrier generation presented here opens up new pathways for the future development of novel materials for single-component organic solar cells.

This chapter is based on the following publication:

Yuriy N. Luponosov, Alexander N. Solodukhin, Artur L. Mannanov, Petr S. Savchenko, [Benedito A. L. Raul](#), Svetlana M. Peregudova, Nikolay M. Surin, Artem V. Bakirov, Maxim A. Shcherbina, Sergei N. Chvalun, Maxim S. Pshenichnikov, Dmitry Yu Paraschuk, and Sergey A. Ponomarenko, *Materials Today Energy* 22, 100863 (2021)

5.1 Introduction

The performance of bulk-heterojunction (BHJ) organic solar cells (OSC) have been significantly improving as a result of the development of novel donor and acceptor materials with better optoelectronic properties¹⁻³. In the BHJ configuration, a nanoscale of phase separated domains of donor and acceptor materials is produced, which ensures efficient exciton harvesting over the whole extent of the solar cell. However, due to the less order in the nano-morphology, well define pathways for charges towards the electrodes are harder to produce which decreases the efficiency of charge collection⁴. Furthermore, the nano-morphology is thermodynamically unstable^{5,6} and the progressive macro-phase separation of donor and acceptor materials are among the most pertinent causes of instability of BHJ configurations. In this manner, the fabrication of OSCs based on a single material presents several benefits over the multi-component BHJ configuration such as, mitigation of morphological instability, cost reduction and further simplification of the fabrication process⁷⁻¹⁰.

There are several classes of materials used in the fabrication of single-component (SC) OSCs ranging from polymers to conjugated donor (D)- π bridge-acceptor (A) small molecules¹¹⁻¹⁵. It has been demonstrated that the utilization of the so-called “double-cable” molecular architecture in which small molecule acceptor fragments are linked covalently but without π -conjugation to the donor polymer backbone allows achieving remarkable power conversion efficiency over 8 % in SC OSC¹⁶. SC OSC based on simple conjugated small molecules have also achieved a modest efficiency of 2.9 %¹⁷. Despite the encouraging progress in device performance, the basic working principle of SC OSC still need to be clarified. It is fundamental to critically asses the ultrafast photophysical processes leading to photocurrent generation, which may help accelerate further improvements in device performance and potentially reach commercial scale applications.

One of the central aspects that determines the process of exciton-to-charge carrier conversion in SC OSCs is the probability of exciton dissociation. The π -bridge length in D- π -A systems controls the extent of intramolecular photoinduced electron-hole separation, which results in a charge-transfer state a precursor for free charges in OSCs¹⁸. Hence, it is reasonable to expect that the probability of exciton dissociation into charge carriers should be controlled by the extent of intramolecular D-A separation.

We have demonstrated in Chapter 4 that intermolecular interactions play a central role on exciton dissociation into charge carriers. In this Chapter, we extend our investigations to the effect of oligothiophene (T) π -bridge length for charge carrier generation and exciton diffusion. With time-resolved photoluminescence (PL) measurements, we show that the elongation of oligothiophene π -bridge in star-shaped molecules from **1T** to **4T** (Figure 5.1) leads to decrease in exciton lifetime which is attributed to the formation of intermolecular CT excitons that facilitates efficient exciton dissociation into charge carriers. Furthermore, with Monte Carlo simulations, we show that the exciton diffusion length decreases with the elongation of oligothiophene π -bridge reaching 2 nm for the **4T** molecule. The short exciton diffusion length is found to be least important for SC OSCs based on the star shaped molecules, in particular when the formation of charge carriers is predominant as in the case of **3T** and **4T** molecules. The obtained results provide insight into how the intramolecular D-A separation in star shaped molecules affects the exciton dynamics and charge carrier generation, which is beneficial for future development of novel materials for highly efficient SC OSCs.

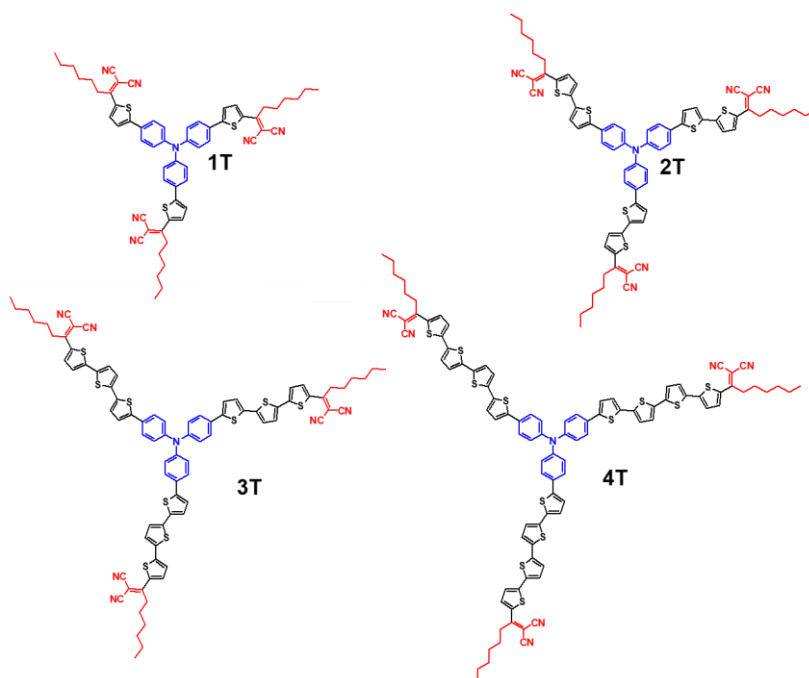


Figure 5.1. Chemical structures of the star-shaped molecules: **1T**, **2T**, **3T** and **4T**.

5.2 Results and Discussion

5.2.1 Absorption and Photoluminescence

Figure 5.2 shows the absorption spectra for **1T-4T** neat films. Two types of absorption bands are observed. The bands in the region of 3.5–2.75 eV are attributed to the π - π^* transition in the conjugated phenylene-oligothiophene fragment and the intense bands in the lower energy region (2.75–2 eV) are attributed to intramolecular charge transfer (CT) between the electron-donating triphenylamine and electron-withdrawing dicyanovinyl blocks^{19,20} or to their mixed characters²¹. The absorption maxima is red shifted with increase of the oligothiophene length from **1T** to **2T** and less pronounced from **2T** to **3T**. And finally, a more pronounced red shift is observed from **3T** to **4T**. This trend is attributed to increase in the conjugation length^{22,23}, with the addition of thiophene units.

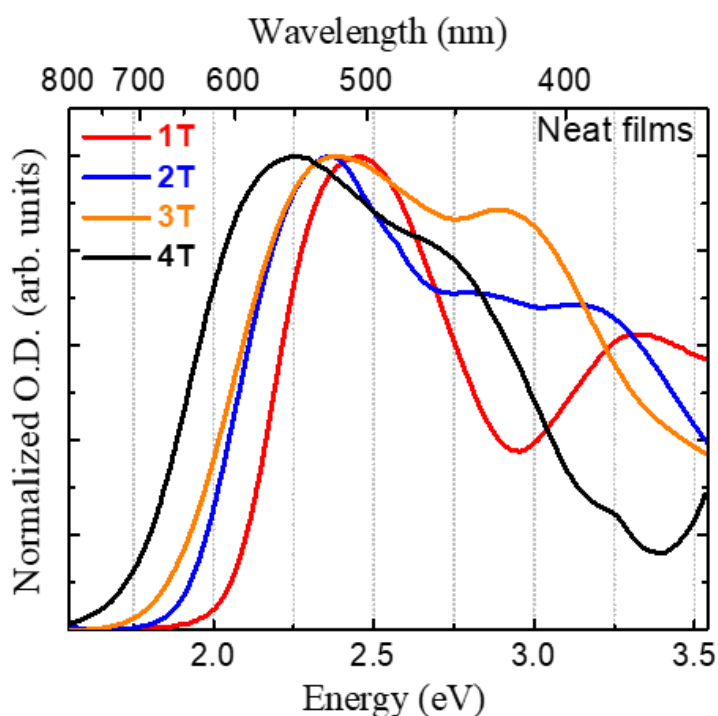


Figure 5.2. Absorption spectra of neat films. **1T** (red), **2T** (blue), **3T** (orange) and **4T** (black).

Figure 5.3 shows the PL spectra of the molecules in PMMA matrix and neat films obtained by integrating the PL maps (Figure 5.4) in the 0-1500 ps range. The molecules dispersed in PMMA matrix at low concentration were used as a reference solid-state environment without intermolecular interactions²³⁻²⁷.

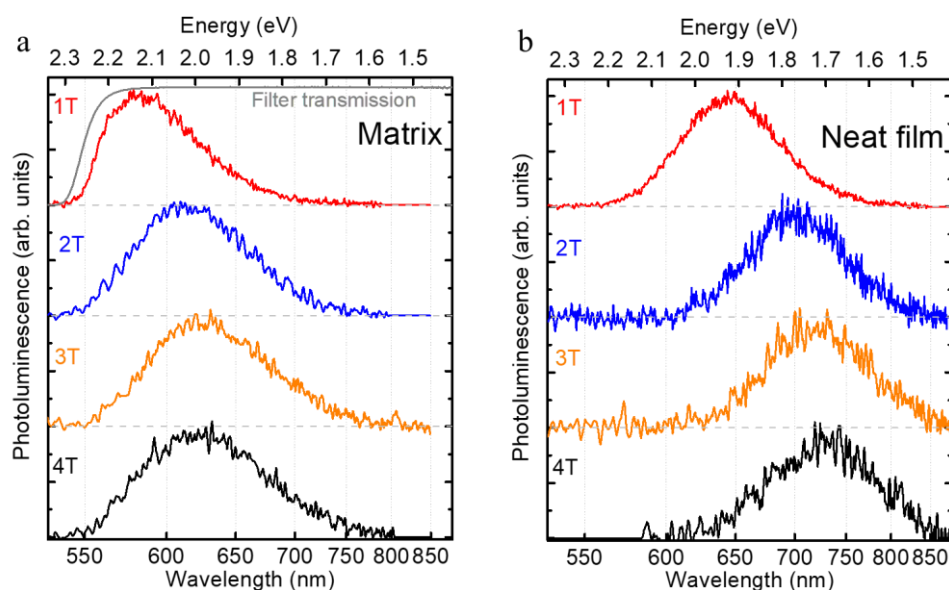


Figure 5.3. Normalized PL spectra of molecules in PMMA matrix (a) and of neat films (b) for 1T (red), 2T (blue), 3T (orange) and 4T (black). The spectra were obtained by averaging the PL maps (Figure 5.4) over all time delays. Gray solid line in (a) represent the transmission of 550 nm long-pass filter used during the experiments; the 1T spectrum is slightly cropped by the filter in the higher energy region. For clarity, each PL spectrum is vertically shifted with respect to the previous one.

The PL maximum positions as determined from fitting the 25-70% (depending on spectrum's signal to noise ratio) top part of the spectra with a Gaussian function are shown in Table 5.1. The increase in thiophene units results in a red shift of the PL spectra in both matrix (by 0.14 eV) and neat films (by 0.23 eV). However, in the matrices, the shift is only observed from **1T** to **3T**. The PL maximum from **3T** to **4T** matrices do not vary and its position is centered at 625 nm. This feature can be explained by the following reasons. On one hand, (i) the **4T** fragment (the longest within this series of molecules) may lead to an intense and red-shifted π - π^* transition band²⁸ overlapping partly with the intramolecular CT band. On the other hand, (ii) with the addition of thiophene units, the number of torsion angles between thiophene units increases making non-planar and hence less conjugated conformations more probable²⁹⁻³¹. As a result, these two factors (i-ii) can decrease the intramolecular CT efficiency and lead to a blue shift of the corresponding intramolecular CT band^{32,33}. In the neat films, these two factors (i-ii) are not predominant, as demonstrated by the variation of the PL maximum position from the **3T** molecule (at 720 nm) to **4T** (at 730 nm).

Table 5.1. PL spectra fitting parameters

Material	PL maximum (nm)	Fitting percentage
1T-matrix	585	25%
2T-matrix	615	35%
3T-matrix	625	35%
4T-matrix	625	35%
1T-neat film	645	25%
2T-neat film	700	40%
3T-neat film	720	50%
4T-neat film	730	70%

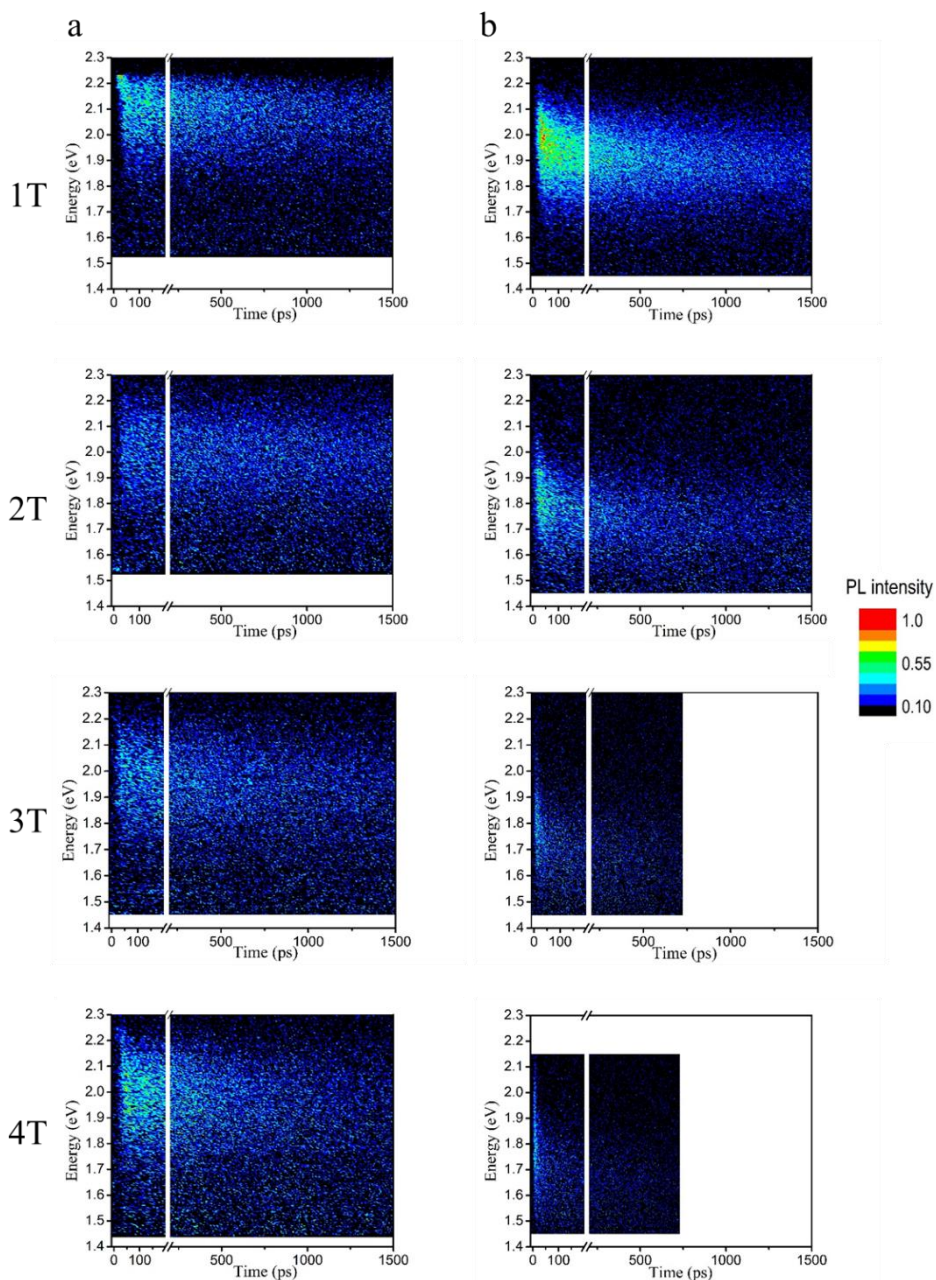


Figure 5.4. Normalized PL maps of the 1T – 4T molecules in PMMA matrix (a) and of neat films (b). The excitation wavelength was set at 520 nm.

5.2.2 Charge Carrier Generation

Figure 5.5 shows PL decay transients in matrices and neat films obtained by integrating the PL maps (Figure 5.4) in the 550–820 nm (2.25–1.5 eV) spectral range. All the matrices exhibit mono-exponential decays with lifetime of 1600 ps for **1T**, **2T**, **3T**, and 800 ps for **4T** (see Table 5.2 for fitting parameters). The shorter lifetime of **4T** matrix as compared to other molecules is also attributed to the two factors (i-ii) mentioned above, that is, (i) possible overlapping between the π - π^* transition band with the intramolecular CT band, (ii) higher conformations (torsions) along the oligothiophene bridge with the addition of thiophene units. These two factors (i-ii) can lead to highly efficient non-radiative recombination of intramolecular CT excitations.

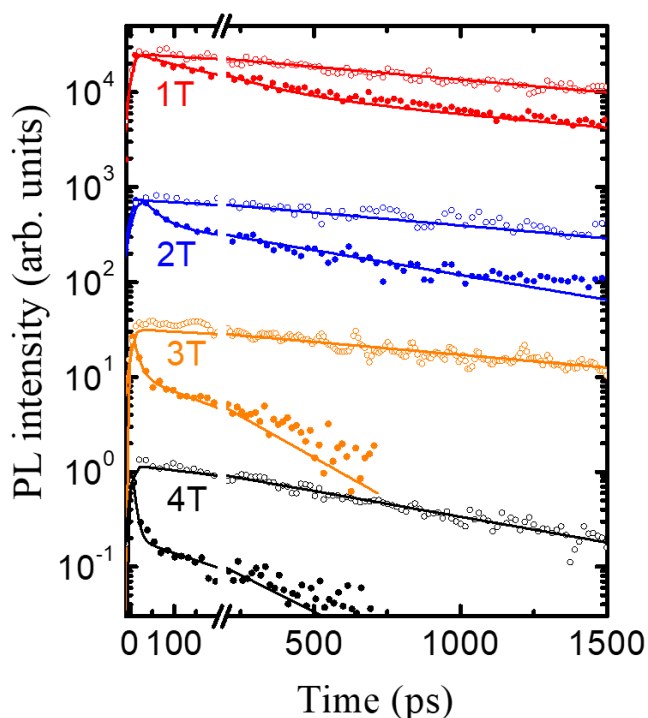


Figure 5.5. PL decay transients for **1T-4T** compounds. Experimental PL decay transients data in the matrices and neat films are depicted by open and close circles, respectively, while the solid lines show the respective fitting convoluted with a Gaussian apparatus function of ~ 3 – 10 ps. For clarity, the PL transients of **1T**, **2T** and **3T** are offset by multiplying by a factor of 30 with respect to the previous transient.

In sharp contrast to the matrices measurements, all the molecules demonstrate bi-exponential PL decays in the neat films. There is a clear decrease in exciton lifetime with the elongation of the oligothiophene bridge (**nT**, **n=1–4**). The shortest component decreases from 200 ps to 10 ps from **1T** to **4T**, and its share increases (Table 5.2). By using time-resolved PL and pump-probe transient absorption measurements, in chapter 4 we demonstrated that in neat films of densely packed star-shaped small molecule efficient exciton-to-charge carrier conversion occurs within the first 200 ps, which leads to generation of intermolecular CT excitons. Similarly, we assign the shortest (within the first 100 ps) components of PL decay transients in the **nT** star shaped molecules to the prompt formation of intermolecular CT excitons, which facilitates the generation of quasi-free charges. This is in line with the increasing values of the external quantum efficiencies, the respective short circuit current density, and an increase in the radius of the initial charge separation observed from **1T** to **4T** as demonstrated by Luponosov et al³⁴.

The slower component in the PL decay transients is attributed to delayed formation of the intermolecular CT excitons during exciton diffusion. The share of this component gradually decreases from ~0.4 in **1T** to ~0.1 in **4T** (Table 5.2) making the almost immediate formation of the intermolecular CT excitons the dominant channel. Note that both increase in the lifetimes and disappearance of the fast-decaying PL component in the matrices signify no formation of the intermolecular CT excitons due to the lack of intermolecular interactions (see Section 5.5.2 for details).

Table 5.2 Excited-state lifetimes, efficiencies of formation of intermolecular CT excitons and exciton diffusion lengths. The values in parenthesis show shares of the exponents. The average exciton lifetime was determined as: $\tau_{avg} = \frac{\sum_i a_i \tau_i^2}{\sum_i a_i \tau_i}$. Note that 10 ps is at the verge of the apparatus resolution.

		1T	2T	3T	4T
Matrix	τ , ps	1600	1600	1600	800 (or 1600)
	$\tau_1 (a_1)$, ps	200 (0.6)	40 (0.65)	15 (0.72)	10 (0.87)
Neat film	$\tau_2 (a_2)$, ps	1600 (0.4)	830 (0.35)	280 (0.28)	250 (0.13)
	τ_{avg} , ps	1400	770	250	200
	Q_{CTE} , %	13	50	85	75 (or 87.5)
	L_D , nm	10	5	3	2

We define the yield Q_{CTE} of formation of the intermolecular CT excitons as $Q_{CTE} = 1 - \frac{\tau_{avg}}{\tau}$, where τ_{avg} is the average PL lifetime in the neat films and τ is the PL lifetime in the PMMA matrices. Hence, in the neat films Q_{CTE} =13, 50, 85 and 75% for **1T**, **2T**, **3T** and **4T**, respectively. As previously mentioned, the main two factors (i-ii) causing the shorter lifetime in the **4T** matrix are not predominant in the neat film; for this reason, the Q_{CTE} value for **4T** can also be estimated not taking into account the non-radiative recombination caused by those two factors (i-ii). Hence, the lifetime in **4T** matrix can be considered to be similar to the other molecules (1600 ps), which results with an Q_{CTE} value of 87.5 % for the neat film of **4T** molecule. These results imply that for **4T** and **3T** there are only 12.5% and 15% excitons available for subsequent diffusion, while for **2T** and **1T** this number increases to 50% and 87%, respectively. Evidently, the higher the amount of excitons available for subsequent diffusion, the higher will be the probability of long-range diffusion. This is demonstrated in the next section, where is shown that the exciton diffusion length decreases with the elongation of oligothiophene bridge.

The obtained results demonstrate the efficiency of exciton dissociation in the solution-processed neat films of the star-shaped molecules, especially for **4T** and **3T**, rendering them highly suitable for single component OSCs as demonstrated by Luponosov *et al*³⁴.

5.2.3 Exciton Diffusion

The next issue to address is the distance over which the excitons can diffuse. The knowledge of exciton diffusion length (L_D) is an essential aspect to be considered for morphology optimization of bulk heterojunction solar cells³⁵⁻⁴⁰, but least important for SC OSCs if fast formation of the charge carriers is predominant. To investigate the exciton diffusion in solution processed films, time-resolved volume quenching experiments (Section 5.5.2) were performed⁴¹. The fullerene derivative PC₆₀BM was used as a quencher molecule and dispersed at different concentrations in the films of the molecules under investigation. Figure 5.6 summarizes the PL quenching efficiencies as a function of average separation between the quenchers. For all the molecules, the PL quenching efficiency is minimal at large separation between quenchers (i.e., at low PC₆₀BM concentrations). Considerable quenching is achieved when the average separation between quenchers is short.

To obtain quantitative information about the effect of the oligothiophene bridge length (nT , $n = 1-4$) on exciton dynamics, we performed Monte Carlo simulations (see Section 5.5.3 for details) to extract the values of exciton diffusion lengths. The exciton diffusion lengths amount to ~ 10 nm, ~ 5 nm, ~ 3 nm, and ~ 2 nm for **1T**, **2T**, **3T** and **4T** (Table 5.2), respectively, which is mostly determined by the number of excitons available for subsequent diffusion after the prompted generation of charge transfer excitons as detailed in previous section. Note that due to fast initial PL decay in **3T** and **4T** (Figure 5.5 and Table 5.2) approaching the apparatus resolution, the uncertainty in exciton displacement might be substantial.

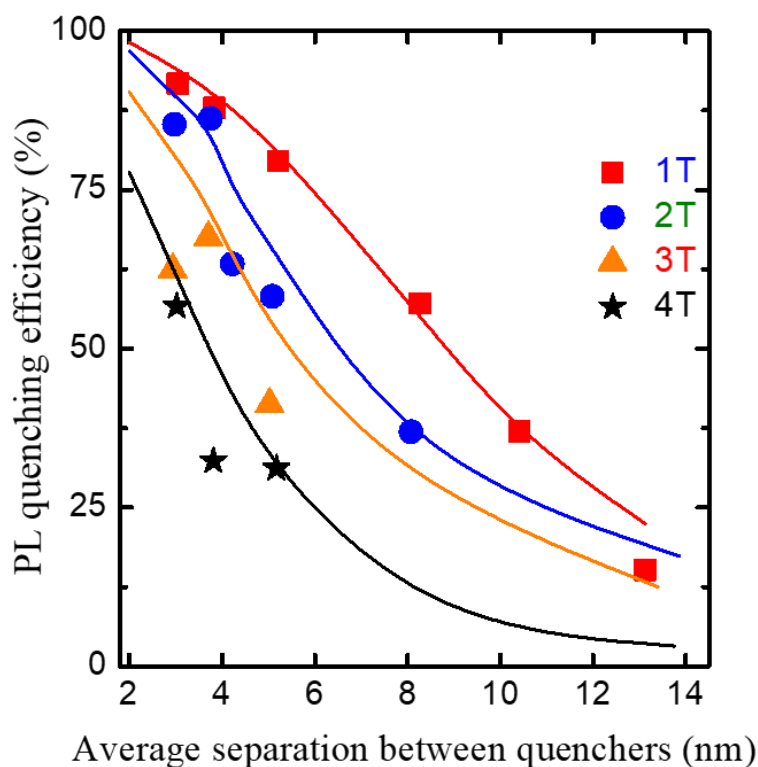


Figure 5.6. PL quenching efficiencies versus average separation between quenchers for **1T** (blue square), **2T** (green circle), **3T** (red triangle) and **4T** (black star). The PL quenching efficiencies and average separation between quenchers were determined as described in Section 5.5.2. The solid lines are the Monte Carlo modeled results (Section 5.5.3).

The obtained results demonstrate a clear correlation of the exciton diffusion length with the length of the oligothiophene bridge. Similarly, to the exciton lifetime, the exciton diffusion length decreases with increase of thiophene units. Therefore, it is reasonable to argue that these two are interconnected, i.e., the intramolecular CT excitation is transferred to the intermolecular CT exciton almost immediately if the energetic conditions are favorable, otherwise the formation of intermolecular CT exciton is delayed, so that the available excitons can contribute to the diffusion process. For these reasons, the short exciton diffusion lengths are not detrimental for high performance SC OSCs as charge photogeneration is predominant.

5.3 Conclusions

We have demonstrated that significantly enhanced charge carrier generation can be realized in star-shaped molecules by varying the intramolecular donor-acceptor spacing. The variation of the oligothiophene π -bridge length from **1T** to **4T** units leads to a significant decrease in excited state lifetime due the formation of intermolecular charge transfer excitons which are the precursors of charges carriers. Thus, the more spatially separated the donor and acceptor units are, i.e., the longer the π -bridge, the more efficient the dissociation of intra- and intermolecular excitons occurs and hence more free charges are generated. The elongation of oligothiophene π -bridge also leads to a decrease in exciton diffusion length as most of photo-generated excitons are immediately converted into charge carriers. The concept presented in this Chapter opens up new avenues for future development of novel donor-acceptor small molecules for highly efficient organic photovoltaic devices.

5.4 Methods

5.4.1 Sample Preparation

Matrices

PMMA (sigma Aldrich, $M_w = 120000$ g/mol) was dissolved in chloroform at a concentration of 150 g/L and stirred at room temperature for 8 hours. Solutions of star-shaped molecules (vide infra) and PMMA were mixed to achieve the mass ratio star-shaped/PMMA of 2.75×10^{-5} and stirred for 4 hours. The matrices were prepared by drop casting the mixed solutions in microscope cover glass substrates.

Neat and mixed films

The solutions of 2 g/L of star-shaped molecules (**1T**, **2T**, **3T** and **4T**) and PC₆₀BM solutions (0.02-0.04 g/L) were separately prepared using chloroform and let stir for 8 hours at room temperature. The solutions were then mixed to achieve the desired PC₆₀BM/(1T, 2T, 3T and 4T) molar ratios (0%-9.4%) and stirred for another 4 hours. The films were prepared by spin coating the solution in microscope cover glass substrates.

5.4.2 Time-resolved Photoluminescence and Absorption

Time-resolved photoluminescence measurements were performed using a Hamamatsu C5680 streak camera and a polychromator. The supercontinuum from the Newport SGC-800 hollow fiber was produced by using the focused output from the mode-locked Ti: sapphire oscillator (Mira 900) as the pump source. A band-pass filter of 520 nm central wavelength and FWHM of 10 nm, was used to generate the excitation wavelength of 520 nm by selecting the portion of the supercontinuum. The excitation power was set between 2-10 μ W. A long pass filter (OG 550) was placed before the polychromator to filter the excitation light.

The absorption spectra were obtained with a PerkinElmer Lambda 900 UV/VIS/NIR spectrometer.

5.5 Supplementary Information

5.5.1 Photoluminescence Mean Energy Shift

Figure 5.7 shows the PL mean energy shift of the molecules in the PMMA matrix and as neat films. In the matrices where intermolecular interactions are mostly suppressed, the PL mean energy shift is negligible (~ 0 eV). However, in the neat films the shift is substantial indicating exciton cooling toward lower energy states, signaling the formation of intermolecular charge transfer excitons as discussed in the main text.

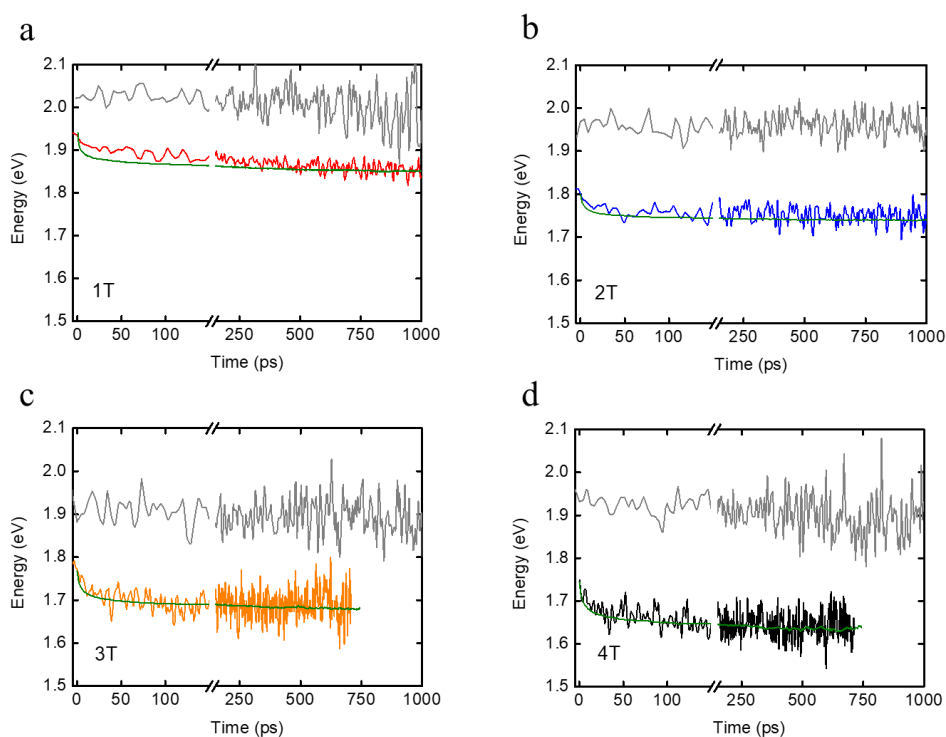


Figure 5.7. PL mean energy shift of the molecules in PMMA matrix (gray lines) and of the neat films. (a) 1T (red), (b) 2T (blue), (c) 3T (orange) and (d) 4T (black). The green solid lines represent the Monte Carlo modeled PL mean energy shift.

5.5.2 Photoluminescence Volume Quenching

The PL decay transients of neat films and films mixed with different PC₆₀BM/(**1T**, **2T**, **3T** and **4T**) molar ratios are shown in Figure 5.8. Concentration increase of the quencher causes acceleration on PL decay transient due to exciton dissociation at the donor-quencher interface.

As the exciton lifetimes for **3T** and **4T** are at the verge of the apparatus resolution it is difficult to distinguish any PL quenching at small concentrations of quencher (< 1.6% molar ratio). To circumvent this limitation, the PL quenching efficiencies values (Figure 5.9) were calculated using the Monte-Carlo modeled PL transients.

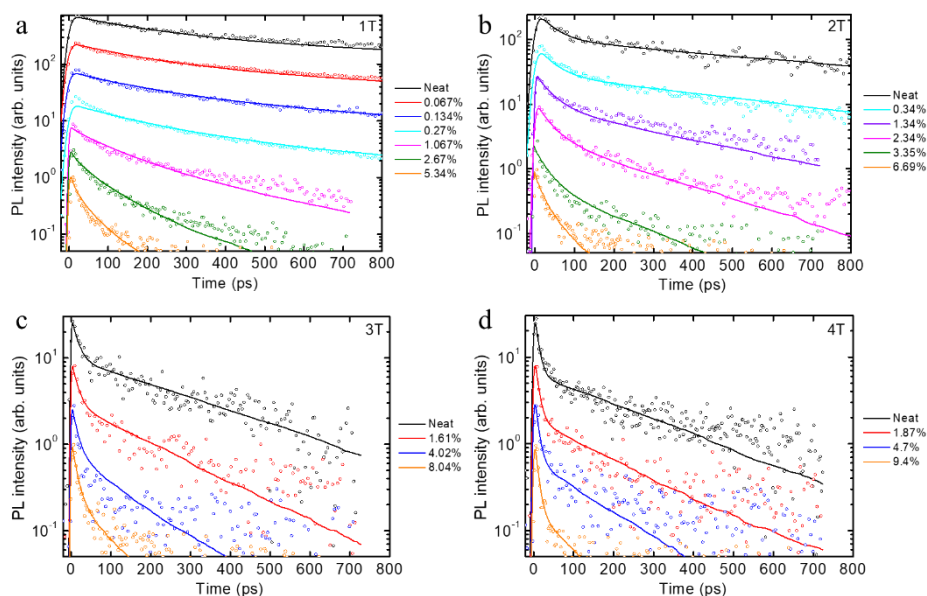


Figure 5.8. Logarithmic plots of the normalized PL decay transients of the neat films (black circles) and mixed films with different content of PC₆₀BM (colored circles). The PC₆₀BM/star-shaped molecule molar ratios are indicated in the legends. The solid lines represent the modeled PL decay transients with Monte Carlo simulations. For better representation, each PL decay transient is multiplied by a factor of 3 with respect to the previous. **(a) 1T**, **(b) 2T**, **(c) 3T**, **(d) 4T**.

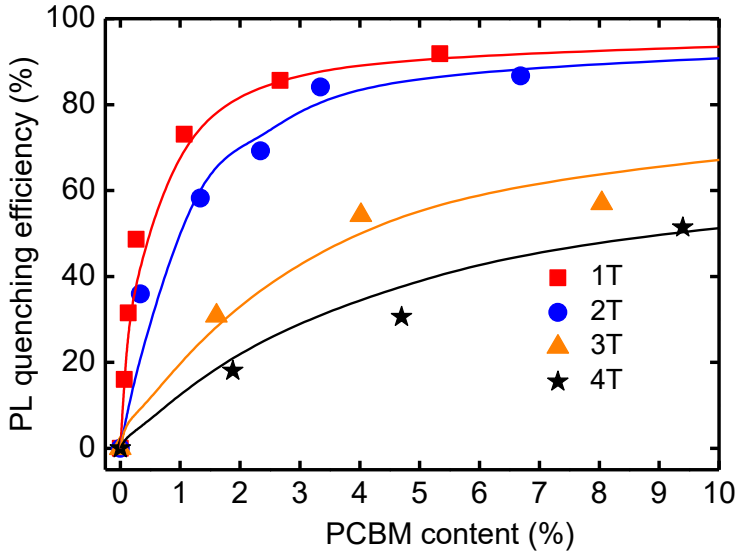


Figure 5.9. PL quenching efficiencies versus PC₆₀BM molar content for 1T (red square), 2T (blue circle), 3T (orange triangle) and 4T (black star). The solid lines represent the results obtained from the Monte Carlo simulations.

Figure 5.9 shows the PL quenching efficiencies as a function of molar concentration. PL quenching efficiency Q was determined as:

$$Q = 1 - \frac{\int \text{PL}_{\text{quenched}} dt}{\int \text{PL}_{\text{neat}} dt} \quad (5.1)$$

where $\text{PL}_{\text{quenched}}$ is the PL decay transient for the samples with different PC₆₀BM content, PL_{neat} is the PL decay transient for the neat film.

Average separation between quenchers was calculated as:

$$d = \sqrt[3]{\frac{M_m}{\rho N_A n_r}} = \sqrt[3]{\frac{1}{n_r}} \times S, \quad (5.2)$$

where ρ is the density of the molecules, M_m is the molecular mass, N_A is the Avogadro constant, n_r is the PCBM/ star-shaped molecule molar ratio, and $S = \sqrt[3]{\frac{M_m}{\rho N_A}}$ is the size of the molecule (averaged over three dimensions). The corresponding values are presented in Table 5.3.

Table 5.3. The density, molecular mass and average size of the molecules.

Material	ρ (g·cm ⁻³)	M_m (g·mol ⁻¹)	S (nm)
1T	1.07	972.36	1.147
2T	1.15	1218.74	1.207
3T	1.19	1465.11	1.269
4T	1.09	1711.48	1.376

5.5.3 Monte Carlo Simulations

Monte Carlo simulations were performed as described in Chapter 2. The simulation input parameters are shown in Table 5.4.

Table 5.4. Monte Carlo Simulations parameters.

Description	Parameter	Value
Cartesian lattice grid	X-Y-Z	300-300-300
Lifetime-1 fraction	a_1	See Table 5.2
Lifetime-1	τ_1	
Lifetime-2	τ_2	
Energetic disorder	σ	~ 60, 40, 50 and 60 meV (for 1T , 2T , 3T and 4T , respectively)
Hopping distance	S	Size of the molecule (see Table S5.2)
Exciton fraction	EF	10^{-4}
Quencher fraction	QF	Variable from 0 to 9.4×10^{-2}
Hopping time (variable parameter)	τ	~ 0.25 and 1.8 ps (for 1T and 2T/3T/4T , respectively)

The energetic disorder values were determined as described in Chapter 2 and the hopping time was the only variable parameter. The modeled dynamical PL mean energy shifts (Figure 5.7) are in good agreement with the experimental results, except for some discrepancy at the early dynamics of **1T** (< 200 ps) which presumably originates from the limited resolution of the streak camera.

Figure 5.10a shows the distribution of exciton displacement from which the exciton diffusion lengths were extracted as the mean values. The exciton diffusion coefficients (Figure 5.10b) were obtained by using the differential form of the Einstein-Smoluchowski relation (see chapter 2 for details). The initial part of the time dependent exciton diffusion coefficient is dominated by fast exciton cooling, and subsequently the thermal quasi-equilibrium is reached from which the values of exciton diffusion coefficient were extracted.

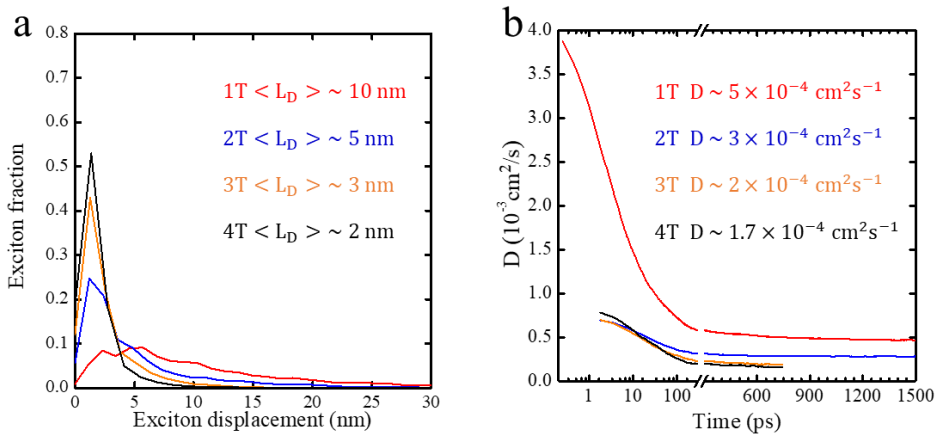


Figure 5.10. Distribution of exciton displacement (a) and time dependent diffusion coefficient (b) for **1T** (red), **2T** (blue), **3T** (orange), **4T** (black).

Author Contributions

B.A.L.R. performed time-resolved PL measurements, Monte Carlo simulations and interpreted the data under supervision of M.S.P; Y.N.L. synthesized and provided the materials.

5.6 References

1. Green, M. A. *et al.* Solar cell efficiency tables (version 52). *Prog. Photovoltaics Res. Appl.* **26**, 427–436 (2018).
2. Meng, L. *et al.* Organic and solution-processed tandem solar cells with 17.3% efficiency. *Science (80-.)*. **361**, 1094–1098 (2018).
3. Liu, Q. *et al.* 18% Efficiency organic solar cells. *Sci. Bull.* **65**, 272–275 (2020).
4. Deibel, C. & Dyakonov, V. Polymer–fullerene bulk heterojunction solar cells. *Reports Prog. Phys.* **73**, 096401 (2010).
5. Cheng, P. & Zhan, X. Stability of organic solar cells: Challenges and strategies. *Chem. Soc. Rev.* **45**, 2544–2582 (2016).
6. Li, N. *et al.* Abnormal strong burn-in degradation of highly efficient polymer solar cells caused by spinodal donor-acceptor demixing. *Nat. Commun.* **8**, 1–9 (2017).
7. Jiang, X. *et al.* Miscibility-Controlled Phase Separation in Double-Cable Conjugated Polymers for Single-Component Organic Solar Cells with Efficiencies over 8 %. *Angew. Chemie Int. Ed.* **59**, 21683–21692 (2020).
8. Jiang, X. *et al.* Miscibility-Controlled Phase Separation in Double-Cable Conjugated Polymers for Single-Component Organic Solar Cells with Efficiencies over 8 %. *Angew. Chemie - Int. Ed.* **59**, 21683–21692 (2020).
9. Wu, Y. *et al.* A conjugated donor-acceptor block copolymer enables over 11% efficiency for single-component polymer solar cells. *Joule* **5**, 1800–1815 (2021).
10. Roncali, J. & Grosu, I. The Dawn of Single Material Organic Solar Cells. *Adv. Sci.* **6**, (2019).
11. Bin, H. *et al.* High-Efficiency All-Small-Molecule Organic Solar Cells Based on an Organic Molecule Donor with Alkylsilyl-Thienyl Conjugated Side Chains. *Adv. Mater.* **30**, 1706361 (2018).
12. Roncali, J., Leriche, P. & Blanchard, P. Molecular Materials for Organic Photovoltaics: Small is Beautiful. *Adv. Mater.* **26**, 3821–3838 (2014).
13. Collins, S. D., Ran, N. A., Heiber, M. C. & Nguyen, T.-Q. Small is Powerful: Recent Progress in Solution-Processed Small Molecule Solar Cells. *Adv. Energy Mater.* **7**, 1602242 (2017).
14. Bogdan, A. *et al.* Structure-properties relationships in triarylamine-based push-pull systems-C60 dyads as active material for single-material organic solar cells. *Dye. Pigment.* **184**, 108845 (2021).
15. Lucas, S. *et al.* Molecular Donor–Acceptor Dyads for Efficient Single-Material Organic Solar Cells. *Sol. RRL* **5**, 2000653 (2021).
16. Jiang, X. *et al.* Miscibility-Controlled Phase Separation in Double-Cable Conjugated Polymers for Single-Component Organic Solar Cells with Efficiencies over 8 %. *Angew. Chemie* **132**, 21867–21876 (2020).
17. Dong, Y. *et al.* Orientation dependent molecular electrostatics drives efficient charge generation in homojunction organic solar cells. *Nat. Commun.* **11**, 4617 (2020).

18. Few, S., Frost, J. M. & Nelson, J. Models of charge pair generation in organic solar cells. *Phys. Chem. Chem. Phys.* **17**, 2311–2325 (2015).
19. Leliège, A. *et al.* Small D- π -A Systems with o-Phenylene-Bridged Accepting Units as Active Materials for Organic Photovoltaics. *Chem. - A Eur. J.* **19**, 9948–9960 (2013).
20. Ripaud, E., Rousseau, T., Leriche, P. & Roncali, J. Unsymmetrical Triphenylamine-Oligothiophene Hybrid Conjugated Systems as Donor Materials for High-Voltage Solution-Processed Organic Solar Cells. *Adv. Energy Mater.* **1**, 540–545 (2011).
21. Kozlov, O. V. *et al.* Ultrafast Charge Generation Pathways in Photovoltaic Blends Based on Novel Star-Shaped Conjugated Molecules. *Adv. Energy Mater.* **5**, 1401657 (2015).
22. Oldham, J., Miao, Y. J., Lachicotte, R. J. & Bazan, G. C. Stilbenoid dimers: Effect of conjugation length and relative chromophore orientation. *J. Am. Chem. Soc.* **120**, 419–420 (1998).
23. Salamatova, E. *et al.* Visualization of molecular excitons diffusion. in (eds. Bakulin, A. A., Lovrincic, R. & Banerji, N.) 99230K (2016). doi:10.1117/12.2237620
24. Simón Marqués, P. *et al.* Triphenylamine/Tetracyanobutadiene-Based π -Conjugated Push–Pull Molecules End-Capped with Arene Platforms: Synthesis, Photophysics, and Photovoltaic Response. *Chem. – A Eur. J.* **26**, 16422–16433 (2020).
25. Kozlov, O. V. *et al.* Triphenylamine-Based Push–Pull Molecule for Photovoltaic Applications: From Synthesis to Ultrafast Device Photophysics. *J. Phys. Chem. C* **121**, 6424–6435 (2017).
26. Raul, B. A. L. *et al.* Excited state dynamics and exciton diffusion in triphenylamine/dicyanovinyl push–pull small molecule for organic optoelectronics. *Sci. Rep.* **10**, 21198 (2020).
27. Kozlov, O. V. *et al.* Ultrafast Exciton-to-Polaron Conversion in Densely Packed Small Organic Semiconducting Molecules. *Adv. Opt. Mater.* **5**, 1700024 (2017).
28. Kanemitsu, Y. *et al.* Optical properties of quasi-one-dimensional thiophene-based oligomers. *Phys. Rev. B* **50**, 2301–2305 (1994).
29. Kagan, J. & Arora, S. K. Synthesis of .alpha.-thiophene oligomers via 1,3-butadiynes. *J. Org. Chem.* **48**, 4317–4320 (1983).
30. Fitzner, R. *et al.* Dicyanovinyl-Substituted Oligothiophenes: Structure-Property Relationships and Application in Vacuum-Processed Small Molecule Organic Solar Cells. *Adv. Funct. Mater.* **21**, 897–910 (2011).
31. Luponosov, Y. N. *et al.* In search of efficient solubilizing groups for liquid and luminescent oligo(phenylene-thiophene) chromophores. *J. Mater. Chem. C* **8**, 17074–17082 (2020).
32. Meier, H., Gerold, J. & Jacob, D. The effect of 2,2-dicyanovinyl groups as electron acceptors in push–pull substituted oligo(1,4-phenylenevinylene)s. *Tetrahedron Lett.* **44**, 1915–1918 (2003).
33. Meier, H. Conjugated Oligomers with Terminal Donor–Acceptor Substitution. *Angew. Chemie Int. Ed.* **44**, 2482–2506 (2005).

34. Luponosov, Y. N. *et al.* Effect of oligothiophene π -bridge length in D- π -A star-shaped small molecules on properties and photovoltaic performance in single-component and bulk heterojunction organic solar cells and photodetectors. *Mater. Today Energy* **22**, 100863 (2021).
35. Cha, H. *et al.* Exciton and Charge Carrier Dynamics in Highly Crystalline PTQ10:IDIC Organic Solar Cells. *Adv. Energy Mater.* **10**, 2001149 (2020).
36. Liu, X. *et al.* Unveiling Excitonic Dynamics in High-Efficiency Nonfullerene Organic Solar Cells to Direct Morphological Optimization for Suppressing Charge Recombination. *Adv. Sci.* **6**, 1802103 (2019).
37. Terao, Y., Sasabe, H. & Adachi, C. Correlation of hole mobility, exciton diffusion length, and solar cell characteristics in phthalocyanine/fullerene organic solar cells. *Appl. Phys. Lett.* **90**, 103515 (2007).
38. Wei, G. *et al.* Efficient, Ordered Bulk Heterojunction Nanocrystalline Solar Cells by Annealing of Ultrathin Squaraine Thin Films. *Nano Lett.* **10**, 3555–3559 (2010).
39. Long, Y. *et al.* Effect of Annealing on Exciton Diffusion in a High Performance Small Molecule Organic Photovoltaic Material. *ACS Appl. Mater. Interfaces* **9**, 14945–14952 (2017).
40. Zhang, Y. *et al.* Large Crystalline Domains and an Enhanced Exciton Diffusion Length Enable Efficient Organic Solar Cells. *Chem. Mater.* **31**, 6548–6557 (2019).
41. Mikhnenko, O. V., Blom, P. W. M. & Nguyen, T.-Q. Exciton diffusion in organic semiconductors. *Energy Environ. Sci.* **8**, 1867–1888 (2015).

Summary

The ever-increasing demand for cleaner sources of energy calls for inexpensive and highly efficient solar cells. Solution- and vacuum-processable organic solar cells have gained significant attention as an attractive source of energy owing to their continuously rising power conversion efficiency, low cost, thin device structure, and mechanical flexibility.

The absorption of light in organic solar cells generates a strongly bound electron-hole pair called an exciton. To efficiently dissociate the exciton into charges, a heterojunction composed of electron donating and accepting materials with suitable energy levels is typically used to provide the driving force needed to overcome the Coulomb attraction between the electron-hole pair. The photon-to-charge conversion in organic solar cells is a complex process that is subject to losses; hence, it is critical to carefully monitor every step from photon-to-charge conversion, such as exciton photogeneration, exciton diffusion towards the donor-acceptor interface, and exciton dissociation into charges. This thesis sheds light on the photon-to-charge conversion process in organic photovoltaics using a multi-disciplinary approach that combines results from steady-state and time-resolved spectroscopy, and Monte Carlo simulations.

The thesis starts with an introduction (Chapter 1) that provides an overview of the photophysical processes in organic semiconductors relevant for organic solar cells, formulates aims and objectives, describes methodologies and main findings, and finally, an overview of the thesis.

In Chapter 2, the photophysical properties of triphenylamine-based push-pull molecules both in solution and the solid state are investigated. Time-resolved photoluminescence measurements reveal that the excited state of these molecules in solution is short-lived when compared with the solid state. These results are shown

to be associated with non-radiative decay through an energetically accessible conical intersection between the excited and ground state potential surfaces. In this manner, these findings reveal that the conformational changes of the molecules in solution open non-radiative decay channels, whereas the confinement of the molecules in the solid state limits the non-radiative losses. Monte Carlo simulations, combined with time-resolved photoluminescence quenching experiments, retrieved an exciton diffusion length of ~ 16 nm in solution-processed films, which demonstrates that the short-excited state lifetime in solutions does not necessarily preclude solid state applications.

The bulk-heterojunction structure is a widely used configuration in the manufacture of organic solar cells as it ensures exciton dissociation over the whole solar cell, without compromising the device thickness needed for efficient photon absorption. Chapter 3 highlights the importance of a thorough morphological investigation prior to the manufacture of bulk-heterojunction device. The investigation of PCBM and five novel fullerene derivatives shows similar photophysical trends when the materials are investigated individually as neat films. However, the photophysical investigation of the fullerenes mixed with an exciton quencher in the form of a bulk-heterojunction film showed that excitons dissociate in sample containing some of the new fullerene derivatives as expected, but hardly dissociate in samples containing the other derivatives. By carrying out a thorough morphological investigation, these results are rationalized to be influenced by the crystallization dynamics of some of the fullerene derivatives that precludes fine-intermixing in the films. In this manner, photo-generated excitons do not reach the heterojunction interface where they would dissociate into charges. This peculiarity could have a significant effect on device performance, hence the need to meticulously account for the crystallization dynamics during the fabrication of bulk-heterojunction devices.

As previously stated, to dissociate the exciton into charges, a heterojunction composed of electron donating and accepting materials with suitable energy levels is typically used. However, it is also possible to dissociate the exciton using a single

material, thereby making single-material organic solar cells possible. There are several strategies used to provide the driving force needed to overcome the Coulomb attraction between the electron-hole pair in a single-component ('material') organic solar cell. Chapters 4 and 5, show that exciton dissociation in single-component devices is achievable by using star-shaped molecules whose structure involves a combination of intramolecular donor and acceptor units. Upon photoexcitation, this combination promotes charge transfer excitons, which are typically considered the precursors of charge carrier generation. Moreover, Chapters 4 and 5 demonstrate that both intermolecular interactions and the elongation of the π -bridge length in star-shaped molecules can control the extent of charge carrier generation. In Chapter 4, through the variation of intermolecular separation, it is shown that photo-generated excitons undergo the formation of intermolecular charge transfer excitons (as evidenced by the bi-exponential photoluminescence decay) which contribute for charge generation. These findings demonstrate that intermolecular interactions play a fundamental role for exciton dissociation in star-shaped molecules.

Chapter 5 extends the investigation of star-shaped molecules to explore the effect of varying the intramolecular donor-acceptor spacing on charge carrier generation and exciton diffusion. The excited state lifetimes and exciton diffusion lengths decrease with the elongation of oligothiophene π -bridge lengths. These results are attributed to an increasing number of photo-generated excitons undergoing charge carrier conversion within the first 100 ps. Thus, Chapter 5 demonstrate that charge carrier generation can be tuned by varying the intramolecular donor-acceptor spacing. These findings provide new perspectives for the future development of novel materials for single-component devices.

Overall, this thesis provides insights into exciton dynamics and charge carrier generation in organic photovoltaics. By addressing the relevant steps of photon-to-charge carrier conversion and identifying the possible loss mechanisms, the presented results further contribute to a better understanding of the photophysical processes that lead to photocurrent generation in organic solar cells.

Samenvatting

De steeds toenemende vraag naar schonere energiebronnen vraagt om goedkope en zeer efficiënte zonnecellen. Organische zonnecellen, die in oplossing en vacuüm verwerkt kunnen worden, hebben aandacht gekregen als een aantrekkelijke energiebron vanwege hun continu stijgende efficiëntie, lage kosten, dunne structuur en mechanische flexibiliteit.

De absorptie van licht in organische zonnecellen creëert een sterk gebonden elektron-gat paar dat exciton wordt genoemd. Om het exciton efficiënt in twee ladingen uiteen te laten vallen, wordt typisch een heterojunctie structuur gebruikt die bestaat uit elektron-donerende en electron-accepterende materialen met geschikte energieniveaus om de drijvende kracht te leveren die de Coulomb-aantrekking tussen de elektron-gat paren (exciton) overwint. De omzetting van een foton naar lading in organische zonnecellen is een zeer complex proces, wat gepaard gaat met verliezen; daarom is het van cruciaal belang om elke stap in de foton-naar-lading conversie zorgvuldig te bekijken, zoals de exciton-fotogeneratie, de diffusie van het exciton naar de donor-acceptor-interface en de exciton-dissociatie in ladingen. Dit proefschrift bestudeert het foton-naar-lading conversieproces in organische fofovoltaïsche materialen met behulp van een multidisciplinaire benadering, die de resultaten combineert van normale en tijdsopgeloste spectroscopie, en Monte Carlo-simulaties.

Het proefschrift begint met een inleiding (Hoofdstuk 1) met een overzicht van de fofofysische processen in organische halfgeleiders, die relevant zijn voor organische zonnecellen. Verder worden de doelen en doelstellingen van het proefschrift geformuleerd en worden de methodologieën en belangrijkste bevindingen geschetst. Tot slot wordt een overzicht van het gehele proefschrift gegeven.

In Hoofdstuk 2 worden de fotofysische eigenschappen van op trifenylamine gebaseerde push-pull moleculen in oplossing en vaste toestand onderzocht. Tijdsopgeloste fotoluminescentiemetingen laten zien dat de aangeslagen toestand van deze moleculen in oplossing korter leeft dan die in vaste toestand. Kan worden uitgerekend dat dit verschil in levensduur komt door stralingsloos verval. Dit stralingsloos verval vindt plaats via een energetisch toegankelijk, conisch snijpunt tussen de potentiaal oppervlakken van de aangeslagen toestand en die van de grondtoestand. De resultaten laten op deze manier zien, dat de conformationele veranderingen van de moleculen in oplossing stralingsloze vervalkanalen openen, terwijl de rigide omgeving van de moleculen in vaste toestand de stralingsloze verliezen beperken. Monte Carlo-simulaties, gecombineerd met tijdsopgeloste fotoluminescentie uitdovingsexperimenten, leverden een exciton-diffusielengte van ~ 16 nm op in films die in oplossing werden verwerkt, wat laat zien dat de korte levensduur van de aangeslagen toestand van de moleculen in oplossing, niet noodzakelijkerwijs toepassingen in vaste toestand uitsluit.

De bulk-heterojunctie structuur is een veelgebruikte structuur in organische zonnecellen, omdat het de exciton dissociatie in de gehele zonnecel garandeert, en er tegelijkertijd kan worden voldaan aan de vereiste dikte van de cel voor een efficiënte licht absorptie. Hoofdstuk 3 benadrukt het belang van een grondig morfologisch onderzoek, voorafgaand aan de fabricage van bulk heterojunctie 'devices'. PCBM en vijf nieuwe fullereen derivaten tonen vergelijkbare fotofysische eigenschappen, wanneer deze materialen afzonderlijk worden onderzocht in pure films. Echter, wanneer deze derivaten worden gemengd met een exciton-quencher in bulk-heterojunctie films, laat fotofysisch onderzoek zien dat de excitonen van sommige van deze derivaten inderdaad, zoals verwacht, dissociëren, maar dat ze dat in andere derivaten nauwelijks doen. Een grondig morfologisch onderzoek laat zien dat kristallisatie in sommige van deze fullereen-derivaten de fijne vermenging in de films belemmert. Dit verhindert dat de excitonen de heterojunctie-interface bereiken, waar ze normaliter in ladingen zouden worden gedissocieerd. Deze eigenschap kan een

groot effect hebben op de prestaties van een zonnecel, vandaar de noodzaak om nauwgezet rekening te houden met de kristallisatiedynamiek tijdens de fabricage van bulk heterojunctie zonnecellen..

Zoals eerder vermeld, wordt typisch een heterojuncte structuur gebruikt, die bestaat uit elektron-donerende en -accepterende materialen, met geschikte energieniveaus om het exciton in ladingen te splitsen. Het is echter ook mogelijk om het exciton te splitsen met één enkel materiaal, waardoor organische zonnecellen gemaakt kunnen worden, die slechts uit één materiaal bestaan. Voor deze zonnecellen kunnen verschillende strategieën worden gebruikt om de drijvende kracht te leveren, die nodig is om de Coulomb-aantrekking tussen het elektron-gat paar te overwinnen. Hoofdstukken 4 en 5 laten zien, dat splitsing van excitonen in ‘devices’ bestaande uit één component, kan worden bereikt met bepaalde stervormige moleculen, die een combinatie van een intramoleculaire donor en acceptor hebben. Door deze combinatie worden bij foton-excitatie ladingsoverdracht excitonen gemaakt, wat doorgaans wordt beschouwd als de voorloper van ladingsdrager generatie. Bovendien laten hoofdstukken 4 en 5 zien, dat bij deze stervormige moleculen zowel door intermoleculaire interacties als ook door de verlenging van de π -bruglengte, de mate van ladingsdrager generatie kan worden beïnvloed. In hoofdstuk 4 wordt door variatie van de intermoleculaire afstand aangetoond, dat door licht gegenereerde excitonen deels worden veranderd in intermoleculaire ladingsoverdracht excitonen (dit blijkt uit het bi-exponentiële photoluminescentieverval), die bijdragen aan het genereren van lading. Deze resultaten laten zien dat in stervormige moleculen intermoleculaire interacties een fundamentele rol spelen in de dissociatie van excitonen.

Hoofdstuk 5 breidt het onderzoek van stervormige moleculen uit, door de intramoleculaire donor-acceptor afstand te variëren en het effect hiervan te bekijken op het genereren van ladingsdragers en excitondiffusie. De levensduur van de aangeslagen toestand en de exciton-diffusielengtes nemen af met de verlenging van de oligothiofeen- π -bruglengten. Deze resultaten worden toegeschreven aan een

toenemende hoeveelheid excitonen die binnen de eerste 100 ps worden geconverteerd in ladingsdragers. Hoofdstuk 5 laat dus zien dat het genereren van ladingsdragers kan worden getuned door de intramoleculaire donor-acceptorafstand te variëren. Deze bevindingen bieden nieuwe perspectieven voor de toekomstige ontwikkeling van nieuwe materialen voor zonnecellen met één component.

Dit proefschrift verdiept het inzicht in de exciton-dynamica en het genereren van ladingsdragers in organische fotonvoltaïsche materialen. Door naar de relevante stappen van foton-naar-ladingsdrager conversie te kijken en de mogelijke verliesmechanismen te identificeren, dragen de resultaten gepresenteerd in dit proefschrift verder bij aan een beter begrip van de fotofysische processen die leiden tot het genereren van ladingen in organische zonnecellen.

Acknowledgements

As I have reached the end of my PhD journey, I would like to acknowledge several people whose contribution was essential, whether directly or indirectly, to my accomplishment in completing this thesis.

My first and foremost appreciation goes to my promoter, Maxim Pchenitchnikov, for giving me the opportunity to be part of his group. Maxim, under your guidance, I have learned a lot during my PhD, not only about science but also about life, which helped me grow as an individual. I am thankful for all your support, and your willingness to help in personal matters. For these and many other reasons, I am deeply grateful.

Secondly, I would like to thank all the SEPOMO project participants for the wonderful times we spent together during the networking events. In particular, I would like to thank Pablo Simón Marqués, José María Andrés Castán, Giacomo Londi, Ivan Ramirez, David Beljonne, Karsten Walzer, Clément Cabanetos, and Philippe Blanchard for our collaboration, which culminated in a publication.

I am thankful to my co-supervisors, L. Jan Anton Koster and Esther Barrena, for their support and helpful feedback during the preparation of this thesis. I also would like to thank the members of the assessment committee, Prof. Richard Hildner, Prof. Koen Vandewal, and Prof. Bruno Ehrler, for their remarks and suggestions.

My PhD journey would not have been quite so smooth without the immense support I received from you, Foppe de Haan. I am truly thankful for your excellent technical support, your outstanding data analysis softwares, and your Monte Carlo simulation code, which simplified my work substantially. Your support was beyond technical, especially during the Coronavirus pandemic lockdown; you always made sure to update us with the latest news, something I truly appreciated.

I also would like to acknowledge Henriet and Vanessa for their administrative support in RUG and SEPOMO.

A big thank you goes to all OCMP and OSFN group members, and Jannete for the friendship and our pleasant chats during the coffee breaks. Special thanks to my former colleague from the OCMP group, Björn Kriete, who contacted me towards the end of my PhD to discuss potential job opportunities. Indeed, as I write this acknowledgment we are once again colleagues. Thank you, Björn.

The results presented in this thesis also benefited from numerous collaborations outside the SEPOMO project. Among them, firstly I would like to thank Dr. Yuriy N. Luponosov, for proving most of the materials investigated in this thesis and performing a thorough revision of Chapter 2. I would also like to thank Assoc. Prof. Dr. Thomas L. C. Jansen for performing the included density functional theory calculations. And finally, I would like to thank Sylvia Rousseva for providing the materials and preparing the samples analyzed in Chapter 3, and also for preparing the samples analyzed in Chapter 5.

A special thanks to my paranympths Sundar and Jan. Jan, you receive my enormous thanks for accepting to be my paranympth and for our nice conversations, especially those about investing. And Sundar, the chill guy. Man, you have such an amazing personality! It was a wonderful experience being your colleague, and I wish that we will become colleagues again one day. Thanks once again for your friendship and for accepting to be my paranympth.

My buddy Nong. Well, actually, Dr. Nong. As you already mentioned in your thesis acknowledgements, we shared a lot in common during our PhD journey. The same funding from the SEPOMO project, the same supervisor. Accordingly, we also attended the same conferences. I must admit that having you as a colleague and a friend made my journey much smoother. I wish you all the best with your new endeavors in Vietnam.

Living in Groningen would not have been pleasant without the many amazing people I met along the way. Sampson, Mustapha, Lungani, Nutifafa and Linda, you all kept my African spirit going and I always looked to you as a source of motivation. Please continue doing wonders and thank you so very much for the nice chats and advice. Many thanks to my salsa dancing partner, Sarah. I hope you will forever continue dancing. Nan and Annerieke, I will forever remember our wonderful conversations. The owners of the dance school Salsa Juan Carlos, it is truly wonderful that you have created an environment where everyone feels welcome and at home. Without a doubt, I will miss a lot being part of such an amazing dancing school.

Finally, a few words in Portuguese for my family. Dedico este trabalho a minha família, em particular a minha mãe pela coragem e resiliência que teve esse todo tempo cuidando de três filhos. Te amo mãe. Ave, Ave, Ave Maria. Creio em salvação, creio em Fátima.

Benedito Amado Luís Raúl

Eindhoven, September 2022

Curriculum Vitae



PERSONAL DETAILS

Date of birth: 04 / 03 / 1992

Nationality: Mozambican

LANGUAGES

Portuguese

English

Turkish

INTERESTS

Salsa and bachata dancing

Travelling

Personal finance

BENEDITO AMADO LUÍS RAÚL

WORK EXPERIENCE

Research Scientist – University of Groningen, Netherlands
02 / 2018 – 02 / 2022

- Created and validated Monte-Carlo simulation Models for investigation of photophysical processes in organic semiconductors
- Performed the Design, maintenance and alignment of optical systems

Researchers Representative – Marie Curie ITN (SEPOMO), Netherlands

01 / 2019 – 01 / 2021

- Participated in supervisory board meetings
- Organized and led meetings with 15 researchers
- Organized network events

Intern – IMEC, Belgium

05 / 2017 – 01 / 2018

- Developed and characterized wide band gap perovskites

EDUCATION

PhD in Physics – University of Groningen, Netherlands
02 / 2018 – 02 / 2022

- Ultrafast spectroscopy of novel organic materials for photovoltaics applications

Master in Renewable Energy Science and Technology –
École Polytechnique, France

2016 – 2018

- Photovoltaics

Bachelor in Physics & Pre-Master in Electrical and Electronics Engineering – Fatih University & Bilkent University, Turkey

2011 – 2016

- Physics, and Electronics